Understanding Plasma-Driven Solution Electrolysis and Its Applications

by

Han-Ting Chen

A dissertation submitted in partial fulfillment
of the requirements for the degree of
Doctor of Philosophy
(Chemical Engineering)
in the University of Michigan
2025

Doctoral Committee:

Professor Suljo Linic, Chair
Associate Professor Bryan R. Goldsmith
Professor Mark J. Kushner
Associate Professor Nirala Singh

Han-Ting Chen

hantingc@umich.edu

ORCID iD: 0000-0002-6942-718X

© Han-Ting Chen 2025

Dedication

This dissertation is dedicated to my beloved partner and parents, whose love and resilience have sustained me.

Acknowledgements

The PhD journey has been a long and challenging marathon, especially as it began during COVID. I am grateful for the support and help I have received from the Linic lab, my friends, and my family, who have guided me through this process. I would like to first acknowledge my funding sources. These works were supported by the Army Research Office and accomplished under Grant No. W911NF-20-1-0105 and Grant No. W911NF-25-1-0207.

I am deeply thankful to my advisor, Prof. Suljo Linic, for his research guidance and mentoring over the past several years. When I broke the equipment, struggled to present my ideas clearly, and gave poor presentations, I always received support and constructive suggestions that led to significant improvement. I also thank my committee members, Prof. Nirala Singh, Prof. Bryan Goldsmith, and Prof. Mark Kushner, for their valuable advice. It is always reassuring to see them at conferences and symposia. Finally, I would also like to thank Prof. Mark Kushner for teaching EECS 517, where I learned about plasma science.

I would like to acknowledge the members of the plasma subgroup, Prof. Dongho Lee and Dr. Yi Zhang, for their support and collaboration. Dongho co-authored Chapters 3 and 4 in this dissertation, who guided me through my first and second year as a mentor and helped me adapt to the lab. Yi has been my teammate for nearly my entire PhD, with whom I shared many discussions about science and life. The PhD journey was not easy for either of us, and I am grateful that we supported each other through its ebbs and flows.

It has been a great honor to attend the monthly meetings and annual reviews with the MURI team, where I learned a lot from the other PIs and researchers. I would like to thank Prof. Peter Bruggeman, Prof. Mark Kushner, Prof. Renee Frontiera, Prof. Uwe Kortshagen, and Prof. George Schatz for their fruitful discussions and collaborations. I would also like to thank members of Bruggeman's group, Dr. Yuanfu Yu, Jae Hyun Nam, and Dr. Jingkai Jiang, for their technical support and insightful discussions.

I am extremely grateful to the Linic Lab members for the time we spent together and for all the help I received. Shiuan-Bai, my labmate and classmate since undergrad, and my roommate during my first year, thank you for your companionship over the past several years. It is reassuring to have someone with a similar cultural background in the lab and to go through the tough times together. I probably would not have made it this far without you in Ann Arbor. Shawn, who is an excellent chef, thank you for hosting lab gatherings and always looking after our well-being. Ahmet and Bill, the "teaching gang", according to Bill, thank you for your support and help as GSIs. Special thanks to the past and current lab members for the thoughtful feedback and advice during group meetings and practice talks. It has been an honor to work with you all.

The PhD journey is tough, and I am grateful to have been lifted by a support system. Fan-Wei, my roommate for the past four years, thank you for taking me in after I was "kicked out" by Shiuan-Bai, for doing the dishes, and for playing squash and pickleball with me. We share so many similarities and know each other almost too well. I am glad that you are still willing to taste the samples from my "baking experiments". Guān lí pêng-an. Yu-Jun (June), a friend since undergrad who came to Ann Arbor a year earlier, thank you for your emotional support and for our grocery runs and Starbucks and McDonald's trip. It was a great honor to join the "Michigan

Chemical Engineering: Escaping to Taiwan subgroup + COVID-Positive Guy", membership earned by serving a 14-day quarantine in Taiwan or by (regrettably) getting COVID while traveling back. Yu-Chen (Ellen), thank you for visiting us several times in Ann Arbor and traveling with June and me to Orlando, Las Vegas, and Denver. I am always amazed by your whimsical stories and enjoy travelling with you, especially our New Orleans trip. Wan-Ni (Wanny), thank you for hosting me in Boston and hanging out with me at AIChE. Hsin-Ting (Dennis), thank you for all the pickleball games and endless baseball discussions. I am amused and oddly honored to receive spam emails with your name, as the department listed my email under your name. Sarah, thank you for inviting me to your wedding. Yi-June, thank you for your guidance as a mentor when I was a naïve undergrad researcher and for driving all the way from Tennessee to visit us. Special thanks to Vivian, Abby, Szu-Hsien, Zi-Jie, members of AATPC, and Chia-Wen, who enriched my life in Ann Arbor.

Last, I would like to thank Yung-Ling (Christine) Kao and my parents, Jung-Yao Chen and Shu-Jing Hong. I am blessed that you supported me in pursuing my dreams while allowing me to only exist in your life for several hours per week on video calls. Life has been difficult, but it feels much better with you around. I look forward to the next chapter in my life, which I will be by your side once again.

Table of Contents

Dedication ii

Acknowledgements iii

List of Tables ix

List of Figures x

Abstract xvi

Chapter 1 Introduction 1

1.1 Summary 1

1.2 Non-Thermal Plasma 1

1.3 Reactions in the Plasma Phase 3

1.4 Reactions at the Electrode Surface 4

1.5 Paschen's Law 5

1.6 Plasma-Liquid Interactions 6

1.7 Faradaic and Non-Faradaic Processes 8

1.8 Plasma-Liquid Sheath 10

1.9 Plasma-Driven Solution Electrolysis 11

1.10 Conventional Electrochemistry 13

1.11 Charge Transfer and Equilibrium 14

1.12 Current versus Applied Potential 15

1.13 Dissertation Scope 16

1.14 References 18

Chapter 2 Experimental Methods 24

2.1 Summary 24
2.2 Plasma Reactors 25
2.3 Plasma Current Profiles and Circuits 32
2.4 Negative and Positive Polarities Power Supply 33
2.5 Pulser and Waveform Generator 34
2.6 Oscilloscope 37
2.7 Rogowski coil 38
2.8 Plasma Ignitions 39
2.9 Chemical Scavengers 40
2.10 Linear Sweep Voltammetry 43
2.11 Open Circuit Potential 45
2.12 Material Characterization Techniques 47
2.13 Gas Chromatography-Mass Spectrometry 48
2.14 References 50
Chapter 3 Bridging Plasma-Driven Solution and Conventional Electrochemistry via an Electrochemical Probe 54
3.1 Summary 54
3.2 Introduction 54
3.3 Experimental Section 55
3.4 Results and Discussions 60
3.5 Conclusions 76
3.6 References 76
Chapter 4 Formation of Mixed Bimetallic Nanoparticles of Immiscible Metals through Plasma-Induced Reduction of Precursors in Solutions: A Case Study of Ag−Pt Alloy Nanoparticles 82
4.1 Summary 82
4.2 Introduction 83

4.3 Experimental Section 84

4.4 Results and Discussions 87

4.5 Conclusions 111

4.6 References 111

Chapter 5 Plasma-Anode Reaction Mechanisms: Direct Cation Oxidation Versus Hydroxyl-Radical Mediation 118

5.1 Summary 118

5.2 Introduction 118

5.3 Experimental Section 122

5.4 Results and Discussions 126

5.5 Conclusions 138

5.6 References 138

Chapter 6 Conclusion and Future Directions 144

6.1 Overall Conclusions 144

6.2 Critiques 150

6.3 Future Directions 153

6.4 References 156

List of Tables

Table 1.1 A comparison of conventional electrochemistry with PDSE highlights the main differences between the two systems. Adapted from [32] 12

Table 2.1 Comparison between two pulsed DC plasma systems..... 26

Table 2.2 The common reactions and their rate constants in the liquid phase. Most of the rate constants are from radiolysis. 41

Table 3.1 The ferricyanide and ferrocyanide concentrations in Figure 3.1b. The total concentration is controlled to be 10 mM. 57

Table 3.2 Rate constants for the selected reactions 65

Table 5.1 Rate constants for the reactions 131

List of Figures

Figure 1.1 Overview of different atmospheric pressure gas discharges spanning a range of more than 10 orders of magnitude in electron density. TD stands for Townsend discharge, while DC stands for direct current. Adapted from [3]. 2

Figure 1.2 The cross-section of water molecules versus electron energy. Reactions are listed on the right-hand side of the figure with their threshold energy. The data were retrieved from the TRINITI database, www.lxcat.net, on November 21, 2023. 4

Figure 1.3 Breakdown voltage for plane-parallel electrodes at 20 ˚C for (a) noble gas and (b) common gas. Adapted from [8] and data from [9]. 6

Figure 1.4 Schematic of discharge types used in plasma-liquid interactions: (A) direct discharge in liquid; (B)-(D) gas-phase discharges; and (E) and (F) multiphase discharges. Details: (B) plasma jet without direct contact with the liquid; (C) gas-phase plasma with a liquid electrode; (D) surface discharge; (E) gas-phase plasma with a dispersed liquid phase (aerosols); (F) discharges in bubbles. Adapted from [10]. 7

Figure 1.5 Schematic diagram of some of the most important species and mechanisms for an Ar/humid air plasma in contact with water. Adapted from [10]. 8

Figure 1.6 Schematic representation of selected redox processes underpinning PDSE. Adapted from [32]. 13

Figure 1.7 Representation of a reduction reaction, which presents the energy level of electrons in an electrode and the molecular orbitals (MO) of an adsorbed species. Electrons move from the electrode to the LUMO of the species. Adapted from [34]. 14

Figure 2.1 Schematic of the plasma reactor setup (left) developed for hydrogen peroxide propylene epoxidation with high selectivity and photo of the plasma discharge in water (right). A glass frit is installed at the plasma-liquid interface. Adapted from [1]. 27

Figure 2.2 Schematic of a pulsed DC plasma-liquid reactor. In this graph, the working gas is He with an applied voltage of -3.5 kV. The plasma pulse width is 5 μs. Adapted from [2]. 27

Figure 2.3 Photo of the plasma jet box after the failure. Carbon residue can be seen next to the metal screws. 30

Figure 2.4 Schematic of the plasma jet configuration (left) including an image of the plasma jet in operation (in false colors; right). Adapted from [3]. 31

Figure 2.5 Connections of the power supply. The port in the far left is connected to the socket. The black line is connected to the interface 14, while the red line is connected to the interface 15. The high-voltage cable is connected to the pulser, and the building earth ground is connected to the grounding port (yellow/green line). A switch is also installed, connected to the red line, for an instant shutoff of the high-voltage supply. 34

Figure 2.6 The panel in the rear of a pulser. The VDCs stand for the input from a high-voltage power supply. The pulser is air-cooled with fans. In the right section, the top cable is the pulser output, connected to the plasma jet. The bottom cable is connected to the socket. The front panel provides the connection to the waveform generator, with a switch to enable the output. .. 35

Figure 2.7 The waveform generator setting panel for a 20 μs pulse with a negative polarity plasma. The pulse width input is 980 μs instead. The waveform is plotted in the figure. 36

Figure 2.8 The waveform generator setting panel for a 20 μs pulse with a positive polarity plasma. The pulse width input is 20 μs. The waveform is plotted in the figure. 37

Figure 2.9 An example of common LSV profiles. (a) Applied voltages versus time between 0.5 V to 0 V versus an Ag/AgCl reference electrode. (b) Corresponding current profiles versus voltage with the addition of 5 mM ferricyanide and 5 mM ferrocyanide. The working electrode was a Pt disk with a rotating speed of 1000 rpm. 44

Figure 2.10 The measured OCP shifts against the measured current values on a Pt electrode. We used a potentiostat to measure the current values on a Pt electrode, denoted as working 1, with 5 mM of ferricyanide and 5 mM of ferrocyanide. 100 mM of potassium sulfate was added as the supporting electrolyte. The OCP shifts between two reference electrodes at different positions were measured with another potentiostat. The reference electrode placed 10 mm away from the Pt electrode is denoted as working 2, while another reference electrode is placed far away from the Pt electrode. 46

Figure 2.11 Bright-field STEM intensity line profiles of (a) Pt-$NP_{(EG)}$ (111) facet, (b) Pt-$NP_{(EG)}$ (220) facet, (c) $Ag_{0.2}Pt_{0.8}$-$NP_{(EG)}$ (111) facet, and (d) $Ag_{0.2}Pt_{0.8}$-$NP_{(EG)}$ (220) facet. These line profiles were smoothed using the Savitzky–Golay algorithm[23] with a polynomial degree of 2. . 48

Figure 3.1 (a) Schematic of the pulsed DC plasma setup and the electrochemical probe with a three-electrode setup. (b) The measured solution potentials versus the ferricyanide-to-ferrocyanide concentration ratios. 56

Figure 3.2 Solution potentials measured with an electrochemical probe before and after PDSE for (a) negative polarity plasma and (b) positive polarity plasma. Corresponding solution potential shifts derived from (a) and (b) under (c) negative polarity plasma and (d) positive polarity plasmas. The close-up views clearly illustrate the shifts for low initial ferricyanide-to-ferrocyanide ratios in (a) and high ferricyanide-to-ferrocyanide ratios in (b). 61

Figure 3.3 The measured current profiles for the negative polarity plasma with the current values (a) 1 mA, (b) 1.5 mA, and (c) 2 mA. The measured current profiles for the positive polarity plasma with the current values (d) 1 mA, (e) 1.5 mA, and (f) 2 mA. For a given current value, the total charge transfer per pulse is calculated and controlled by applying different

voltages. During the pulse with a specified current value and a pulse width, a constant voltage is applied to the high-voltage electrode. The current values are defined to be positive when the current is from the liquid phase to the plasma phase. 63

Figure 3.4 Plasma-generated electrochemical potentials for (a) negative polarity plasma and (b) positive polarity plasma. High-energy species ratios for (c) negative polarity plasma and (d) positive polarity plasma. 68

Figure 3.5 The electron and •OH fluxes to the liquid surface as a function of time for a voltage pulse width of 9 μs. The electron flux was estimated from the interfacial surface area and the current. The •OH flux was estimated by the number density gradient times the diffusion coefficient of •OH near the liquid interface. Adapted from [11]. 71

Figure 3.6 Plasma-generated electrochemical potentials for (a) negative polarity plasma with 100 mM KNO_3 and (b) positive polarity plasma with 100 mM KCl. High-energy species ratios for (c) negative polarity plasma with 100 mM KNO_3 and (d) positive polarity plasma with 100 mM KCl. 73

Figure 3.7 (a) Schematic of the Pt electrode setup and the electrochemical probe with a three-electrode setup. (b) The measured solution potential shifts versus the initial solution potentials after applying 310 mV and 190 mV to the Pt electrode at 500 rpm. The electrode potentials were applied against an Ag/AgCl reference electrode. 74

Figure 3.8 Solution potential shifts versus initial solution potentials for (a) an applied electrode potential of 190 mV with and without 100 mM KNO_3, and (b) an applied electrode potential of 310 mV with and without 100 mM KCl. The data indicate that these scavengers do not affect reduction or oxidation in the conventional electrochemical system. 75

Figure 4.1 (a) Schematic of the pulsed DC plasma setup with applied voltage *Vs* and ballast resistance R_B. The M^{+n} metal ions are reduced to M^0 zerovalent atoms by the solvated electrons in the liquid. The current versus time for a single plasma pulse with a 20 μs pulse width while interacting with (b) aqueous and (c) EG solution, respectively. The fixed voltage is -2 kV, and the frequency is 1 kHz. Both solutions contain 0.1 mM $AgNO_3$ and 10 mM $Pt(NH_3)_4(NO_3)_2$.... 88

Figure 4.2 Infrared-measured temperature distribution of the EG solution containing 0.1 mM $AgNO_3$ and 10 mM $Pt(NH_3)_4(NO_3)_2$ is shown in (a) before plasma-liquid interactions and (b) after ten minutes of plasma-liquid interaction when the temperature reached equilibrium. 89

Figure 4.3 Ultraviolet-visible extinction spectra of the precursor solution (0.1 mM $AgNO_3$ and 10 mM $Pt(NH_3)_4(NO_3)_2$ in EG solution) at room temperature and after heating the precursor solution to 25°C and 48°C for 10 minutes. The negligible changes in the UV-vis extinction spectra indicate that no spontaneous reduction reaction occurs at 25°C and 48°C. 90

Figure 4.4 (a) The dark-field STEM image, (b) overlapping Ag and Pt EDS mapping data with the STEM image, and (c) EDS line scan of the Ag and Pt net signals of $Ag_{0.2}Pt_{0.8}$-$NP_{(EG)}$ synthesized in EG. (d) The dark-field STEM image, (e) overlapping Ag and Pt EDS mapping data with the STEM image, and (f) EDS line scan of the Ag and Pt net signals of a nanoparticle

synthesized in aqueous solution. The dark-field STEM images were acquired by the high-angle annular dark-field detector (HAADF). 92

Figure 4.5 (a) UV-vis extinction spectrum of $Ag_{0.2}Pt_{0.8}$-$NP_{(EG)}$ in EG solution. (b) Size distribution of $Ag_{0.2}Pt_{0.8}$-$NP_{(EG)}$. The average nanoparticle size is 10.5 ± 2.0 nm..... 93

Figure 4.6 EDS line scan of Pt-$NP_{(EG)}$ exhibits Ag and Pt signals. Ag signals are negligible, confirming it as a Pt monometallic nanoparticle. 93

Figure 4.7 (a) The Pt 4f XPS core scan comparison between $Ag_{0.2}Pt_{0.8}$-$NP_{(EG)}$ and Pt-$NP_{(EG)}$, a shift is clearly shown. (b) The XRD pattern comparison between $Ag_{0.2}Pt_{0.8}$-$NP_{(EG)}$ and Pt-$NP_{(EG)}$. The peak position of the $Ag_{0.2}Pt_{0.8}$-$NP_{(EG)}$ (111) facet shifts to the one of the Ag (111) facet. (c) The bright-field STEM image of Pt-$NP_{(EG)}$ along with its lattice structure of a cubic structure. (d) The bright-field STEM image of $Ag_{0.2}Pt_{0.8}$-$NP_{(EG)}$ along with its lattice structure of a cubic structure. The reported lattice constants were measured with a pixel size of 0.718 pm. 95

Figure 4.8 Current versus potential profiles from linear sweep voltammetry are shown for (a) silver precursor in aqueous solution, (b) platinum precursor in aqueous solution, (c) silver precursor in ethylene glycol solution, and (d) platinum precursor in ethylene glycol solution.... 98

Figure 4.9 Logarithm of current versus potential profiles from linear sweep voltammetry are shown for (a) silver precursor in aqueous solution, (b) platinum precursor in aqueous solution, (c) silver precursor in ethylene glycol solution, and (d) platinum precursor in ethylene glycol solution. Each condition contains six different concentrations. 99

Figure 4.10 The onset reduction potential versus the log of the concentration of Ag (Ag^+) and Pt ($Pt(NH_3)_4^{2+}$) precursor in (a) aqueous solution and (b) EG solution. A 340 mV onset reduction potential gap is observed between two metal salt precursors in aqueous solution (0.1 mM Ag^+: 520 mV; 10 mM $Pt(NH_3)_4^{2+}$: 180 mV), while a negligible difference is found in EG solution (0.1 mM Ag^+: 322 mV; 10 mM $Pt(NH_3)_4^{2+}$: 326 mV)..... 100

Figure 4.11 (a) The current profile of the three concentration conditions with matched reduction potentials. The current profiles show negligible differences. (b) The dark-field STEM image and (c) overlapping Ag and Pt EDS mapping data with the STEM image of nanoparticles synthesized in ethylene glycol solution containing 0.36 mM $AgNO_3$ and 100 mM $Pt(NH_3)_4(NO_3)_2$. (d) The corresponding EDS line scan of the nanoparticle in the middle with only Ag signals. (e) The corresponding EDS line scan of the nanoparticles in the bottom-right with both Pt and Ag signals. (f) The dark-field STEM image and (g) overlapping Ag and Pt EDS mapping data with the STEM image of a nanoparticle synthesized in ethylene glycol solution containing 0.078 mM $AgNO_3$ and 3 mM $Pt(NH_3)_4(NO_3)_2$. (h) The corresponding EDS line scan of the nanoparticle with both Ag and Pt signals. 103

Figure 4.12 (a) Dark-field STEM image and (b) overlapping Ag and Pt EDS mapping data with the STEM image of a nanoparticle synthesized in ethylene glycol solution containing 0.36 mM $AgNO_3$ and 100 mM $Pt(NH_3)_4(NO_3)_2$. (c) EDS line scan of the net Ag, net Pt, and high-angle

annular dark-field detector (HAADF) signals. The line scan focused on a pore and indicated a decrease in Ag signals. 105

Figure 4.13 (a) Low-magnification dark-field STEM image, (b) EDS Pt mapping data, (c) EDS Ag mapping data, and (d) overlapping Ag and Pt EDS mapping data with the STEM image of the nanoparticles synthesized in ethylene glycol solution containing 0.078 mM $AgNO_3$ and 3 mM $Pt(NH_3)_4(NO_3)_2$. 106

Figure 4.14 (a) Current profiles of plasma discharge with 20 μs and 40 μs pulse width in the ethylene glycol solution containing 0.1 mM $AgNO_3$ and 10 mM $Pt(NH_3)_4(NO_3)_2$. (b) Dark-field STEM image and (c) overlapping Ag and Pt EDS mapping data with the STEM image of the samples synthesized with a 40 μs pulse width. (d) EDS line scan of the nanoparticle marked with a yellow rectangle on the bottom left of (b) with mainly Ag signals. (e) EDS line scan of the nanoparticle marked with a red square of (b) with both Ag and Pt signals. The Pt-to-Ag atomic ratio is about 80 to 20%. 108

Figure 4.15 (a) Low-magnification dark-field STEM image, (b) EDS Pt mapping data, (c) EDS Ag mapping data, and (d) overlapping Ag and Pt EDS mapping data with the STEM image of the nanoparticles synthesized from thermal reduction. From another spot in the same sample, we conducted measurements again with the line scans as shown in the following figures. (e) Dark-field STEM image and (f) overlapping Ag and Pt EDS mapping data with STEM image of the nanoparticles synthesized from thermal reduction. (g) Corresponding EDS line scan of the nanoparticles at the top with only Ag signals. (h) Corresponding EDS line scan of the nanoparticle in the bottom with only Pt signals. 110

Figure 5.1 Breakdown voltage as a function of pd (pressure times distance). Fitting results suggest that the secondary-electron emission coefficient is at most 10^{-5}. Adapted from [21]. 120

Figure 5.2 Diagram of possible processes driven by plasma ions injected into water for an argon anode glow discharge electrolysis. Adapted from [26]. 121

Figure 5.3 The measured intensity from a GC-MS versus the known concentration of (a) IPA and (b) acetone in the liquid phase. Both curves show linear behaviors and can be used as calibration lines. 124

Figure 5.4 Known ferricyanide concentrations versus the extinction values from UV-vis spectra, which illustrates a linear behavior. 125

Figure 5.5 (a) Plasma reactor with an H-cell configuration. Both chambers were stirred to mitigate the mass-transfer limitations. (b) GC-MS spectra with three current values. The peaks are assigned to acetone and IPA, respectively. (c) The IPA concentration versus reaction time for a plasma-anode configuration (pulse width 10 μs, current 2.5 mA) and for 20 ˚C IPA evaporation. (d) Natural-log scale concentrations normalized by the initial concentration versus reaction time, converted from (c). 127

Figure 5.6 The measured current profiles for the plasma anode with the current values 2.5, 3, and 3.5 mA for pulse widths (a) 10 μs, (b) 5 μs, and (c) 3 μs. For a given current value, the total charge transfer per pulse is calculated and controlled by applying different voltages.

During the pulse with a specified current value and a pulse width, a constant voltage is applied to the high-voltage electrode. 129

Figure 5.7 Measured acetone concentration versus plasma-liquid interaction time. Acetone concentrations plateaued and decreased due to its high volatility. 130

Figure 5.8 (a) $\ln(C/C_0)$ versus time for solutions containing different concentrations of ferricyanide/ferrocyanide redox couple. (b) $\ln(C/C_0)$ versus time with 0, 400, and 800 mM Cl^-. The two •OH scavengers both showed no measurable effect on the reaction. With a supporting electrolyte present in all cases, the addition of these salts did not alter the current or voltage profiles, which have been previously reported.[34] 132

Figure 5.9 The measured current profiles for the plasma cathode with the current values 2.5, 3, and 3.5 mA for pulse widths (a) 10 μs, (b) 5 μs, and (c) 3 μs. For a given current value, the total charge transfer per pulse is calculated and controlled by applying different voltages. During the pulse with a specified current value and a pulse width, a constant voltage is applied to the high-voltage electrode. 134

Figure 5.10 (a) Measured IPA consumption rate constant for both plasma-anode and plasma-cathode configurations. (b) Rate constants after eliminating the contribution from the non-Faradaic processes. These rate constants are attributed to cation-induced IPA reactions. 135

Figure 5.11 The applied voltages versus the applied current with 3, 5, and 10 μs pulse width. The voltages increased while the current increased and while the pulse width decreased. 136

Figure 5.12 (a) Oxidation of ferrocyanide to ferricyanide driven by plasma-liquid interaction in a plasma-anode configuration. (b) Oxidation of IPA to acetone under the same conditions. The molar changes are normalized to the charge input. 137

Figure 6.1 Graphical abstract of Chapter 3. We illustrated the electrochemical measurements and the characterization of the high-energy species in PDSE. 146

Figure 6.2 Graphical abstract of Chapter 4. We illustrated the three requirements to exclusively form immiscible bimetallic alloy nanoparticles. 148

Figure 6.3 Graphical abstract of Chapter 5. We illustrated the two possible reaction pathways and demonstrated that Route 2 is more likely to be the case for the IPA-to-acetone oxidation reaction. 150

Figure 6.4 LIF intensity, water vapor, and •OH density for He and argon (Ar) DC discharges for varying discharge currents. Voltages were adjusted to achieve the specified currents. Adapted from [1] 155

Abstract

Non-thermal plasma generates high-energy species under ambient conditions by utilizing electrons to drive chemical reactions in the plasma phase. When coupled to a liquid phase, these electrons, along with other reactive species, such as radicals, ions, and photons, can transfer into the liquid phase and drive reactions that are otherwise challenging to achieve. In this dissertation, we focus on plasma-driven solution electrolysis (PDSE). In PDSE, the charge transfer process is emphasized, as it resembles conventional electrochemical systems by replacing one or both electrodes with plasma. PDSE has been explored for nanomaterials synthesis, material processing, chemical conversion, and polymerization reactions. Still, despite its wide range of applications, the characterization and utilization of these high-energy species, along with their reaction mechanisms, remain insufficiently understood.

In this dissertation, we first establish a framework to compare PDSE with conventional electrochemical systems. Similar to a conventional electrochemical system, we show that the plasma-liquid interface can drive oxidation and reduction reactions using both positive (plasma anode) and negative (plasma cathode) polarity plasma. Moreover, we find that PDSE can reach net-zero conversion of the redox couple, which is analogous to the condition in which the electrode potential equals the solution potential in a conventional system. Because the interfacial reactions are driven by high-energy species, this potential at which no-net conversion occurs under PDSE can also be interpreted in terms of the effective concentrations of those species, which is supported by the scavenging of high-energy species.

Building on the relative reducing and oxidizing capabilities revealed by polarity switching, we then utilized the plasma-cathode configuration to drive reduction reactions. We focus on the synthesis of bimetallic immiscible alloy nanoparticles. We developed three design requirements: (1) the reduction rates of the metal precursors must be high to kinetically trap the immiscible metal atoms in a single structure; (2) the reduction rates of the two precursors must be matched, as assessed by their onset reduction potentials, so that both metals are present simultaneously and can be kinetically trapped; and (3) the nucleation process must be controlled to avoid the nucleation threshold at which burst nucleation occurs and to yield exclusively alloy nanoparticles. These requirements are fulfilled by PDSE through its high metal precursor reduction rates and the control of reaction time on the μs scale.

Last, we revisited the positive polarity (plasma-anode) configuration that mainly drives oxidation reactions. We challenged the common view that hydroxyl radical formation is essential in this system. We used a probe molecule with a lower O-H bond dissociation enthalpy change than that of water to test the following two reaction mechanisms at a plasma-anode/water-cathode interface: (1) a cascading pathway in which cation-water reactions generate •OH that oxidizes solutes, and (2) a direct cation-solute pathway without intermediate involvement. We discovered that the conversion of the probe molecule was not suppressed by hydroxyl radical-scavenging experiments, which suggests a direct cation-substrate reaction. Moreover, we demonstrated that the Faradaic efficiency trends on plasma parameters differed between the above-mentioned two mechanisms. These results identify a direct cation-substrate oxidation reaction pathway and highlight the need for reaction pathway understanding for process optimization.

Chapter 1 Introduction

1.1 Summary

This chapter provides the background for the dissertation, which focuses on the characterization, reaction mechanisms, and applications of plasma-driven solution electrolysis (PDSE). To frame PDSE, we address three themes: (1) plasma properties, including definitions and key physical and chemical characteristics; (2) plasma-liquid interactions, emphasizing charge transfer, the transport of reactive species, and the role of the plasma sheath; and (3) conventional electrochemical systems, motivated by the analogy that PDSE replaces an electrode with a plasma to drive electrochemical reactions. Collectively, these sections establish the fundamental basis for understanding PDSE.

1.2 Non-Thermal Plasma

Plasma, a fully or partially ionized gas, is commonly classified as thermal or non-thermal according to the relative temperatures of its constituent species. In thermal plasmas, electrons, ions, and neutral molecules are close to thermal equilibrium and share similarly high temperatures. Typical examples include lightning, stellar atmospheres, and astrophysical nebulae.[1-2] In non-thermal plasmas (NTP), by contrast, the electron temperature (T_e) greatly exceeds the ion (T_i) and neutral gas temperatures (T_g), which often remain near ambient. This non-equilibrium arises from the low mass and high mobility of electrons, since collisional energy transfer to heavier species is insufficient to equilibrate the system under typical conditions.

Common NTP configurations include dielectric barrier discharges, corona discharges, radio frequency plasmas, and microwave plasmas. Among these, atmospheric-pressure NTPs have received particular attention due to their ability to treat liquids and heat-sensitive materials, such as biological targets, that cannot tolerate low-pressure or vacuum environments.[3] The properties of atmospheric-pressure plasmas span several orders of magnitude in reactor size, applied frequency, reactive species number density, and electron number density. For example, Figure 1.1 compares electron number densities across representative atmospheric-pressure NTP sources. To maintain the background gas near ambient temperature and minimize gas heating, common strategies include noble gas admixtures (which offer higher thermal conductivity and lower breakdown voltages than most molecular gases), high gas flow rates, reduced reactor size, and transient, pulsed operation.[3]

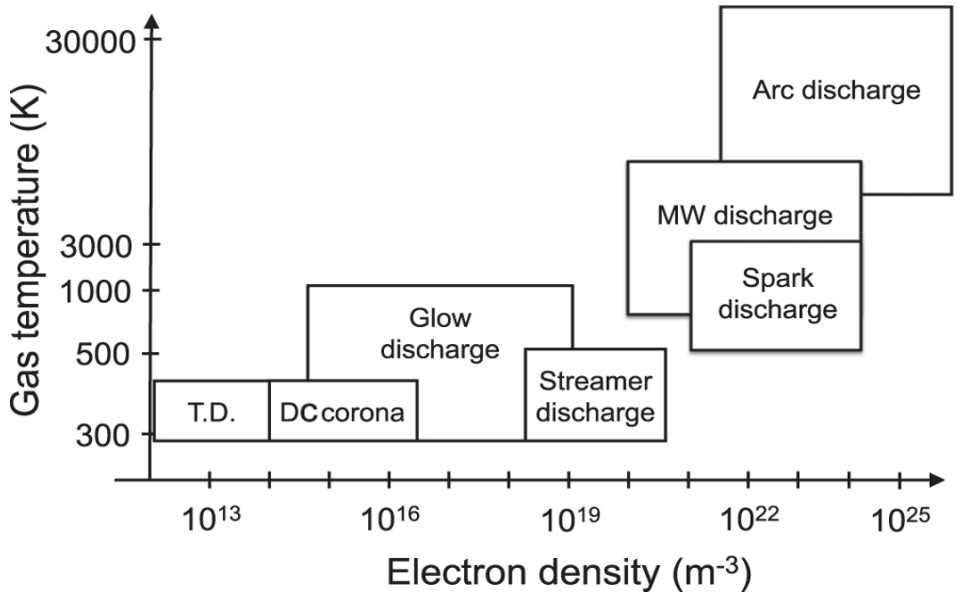


Figure 1.1 Overview of different atmospheric pressure gas discharges spanning a range of more than 10 orders of magnitude in electron density. TD stands for Townsend discharge, while DC stands for direct current. Adapted from [3].

1.3 Reactions in the Plasma Phase

Electrons accelerated by the electric field initiate electron-molecule interactions, including elastic collision, attachment, rotational-vibrational excitation, electronic excitation, and ionization. The rates of these processes are governed primarily by two quantities: the threshold energy (the minimum electron energy required for a given reaction) and the collision cross-section (the effective target area that determines the probability of reaction as a function of electron energy). Together with the electron and neutral number densities and the electron energy distribution function (EEDF), these parameters determine process rates in the plasma phase. These data are available in the LXCat online database.[4-6] For example, the cross-sections of electron-induced reactions with water molecules are plotted in Figure 1.2.

Among these interactions, elastic scattering has no threshold and transfers little energy to neutral molecules due to the large mass disparity. Rotational-vibrational excitation deposits energy into molecular internal modes, whereas electronic excitation promotes electrons in the target species to higher electronic states. Ionization ejects an electron from a neutral molecule, producing a positive ion and a free electron. The ejected electron can be accelerated by the electric field and induce additional impact ionizations, leading to an electron avalanche. Beyond these excitation and ionization pathways, loss processes also occur. Excited species relax via radiative emission or collisional quenching (including vibrational-translational energy transfer), and free electrons are removed through electron-ion recombination. Electron attachment to molecules also provides an additional loss pathway for free electrons.

Beyond electron-induced reactions, other processes are noteworthy. Penning ionization involves a reaction between two excited species whose total energy exceeds the ionization threshold of one particle. It often occurs in discharges with gaseous mixtures as excited noble gas

species (He* and Ar*) ionize other gases (N_2, H_2O, and O_2). Ultraviolet (UV) emitted by the discharge also drives chemistry in the plasma phase, including photoionization, photodissociation, photodetachment, and photoexcitation. Photoionization often dominates in corona discharges.

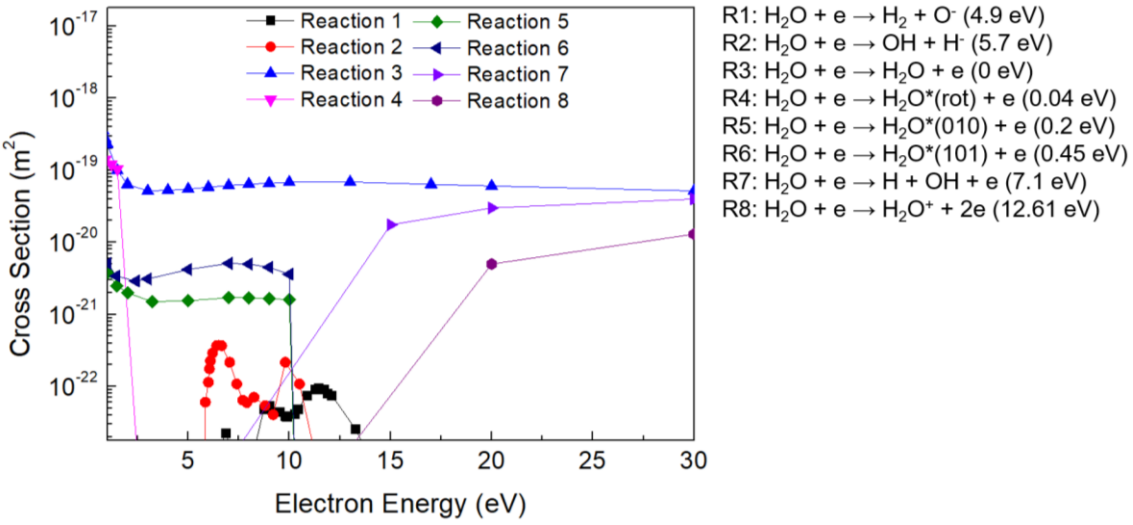


Figure 1.2 The cross-section of water molecules versus electron energy. Reactions are listed on the right-hand side of the figure with their threshold energy. The data were retrieved from the TRINITI database, www.lxcat.net, on November 21, 2023.

1.4 Reactions at the Electrode Surface

Secondary-electron emission from the cathode, which is triggered by ions, metastable particles, or UV photons, provides the seed electron flux that enables ignition and sustains a plasma discharge. The minimum energy required for electron emission is determined by the work function of the electrode material, while the yield depends on the electrode material and the discharge gas. The secondary-electron emission coefficient, γ, is the ratio of the number of secondary electrons emitted from a surface to the number of ions incident on that surface. This coefficient is generally on the order of 10^{-1}, namely, approximately 10% of incident ions

generate secondary emission.[7] The electrons emitted from this process are accelerated across the sheath, initiating avalanches and driving plasma-phase reactions.

1.5 Paschen's Law

Plasma ignition requires applying a sufficiently high voltage between electrodes in a gas-filled gap. For a direct current (DC) glow discharge, the minimum voltage to initiate a discharge is the breakdown voltage (V_B), which is normally measured empirically and can also be estimated by Paschen's law,[8] where A (unit: $Torr^{-1}$ cm^{-1}) and B (unit: V $Torr^{-1}$ cm^{-1}) interpolate the gas Townsend coefficients from experiments, γ is the secondary emission coefficient, p is the pressure in Torr, and d is the gap distance in cm. In Figure 1.3, the breakdown-voltage curves as a function of pd are shown for some common gases.

$$V_B = \frac{Bpd}{\ln(Apd) - \ln[\ln(1+\frac{1}{\gamma})]} \quad \text{(Equation 1.1)}$$

For given gas types and electrode materials, the breakdown voltages can be expressed as a function of only the pressure (p) and the distance (d). It should be noted that this applies to parallel plates and only to glow discharge. For a point to plane electrode configuration, large gaps, and electronegative admixture gas, deviations from Paschen's law may occur.

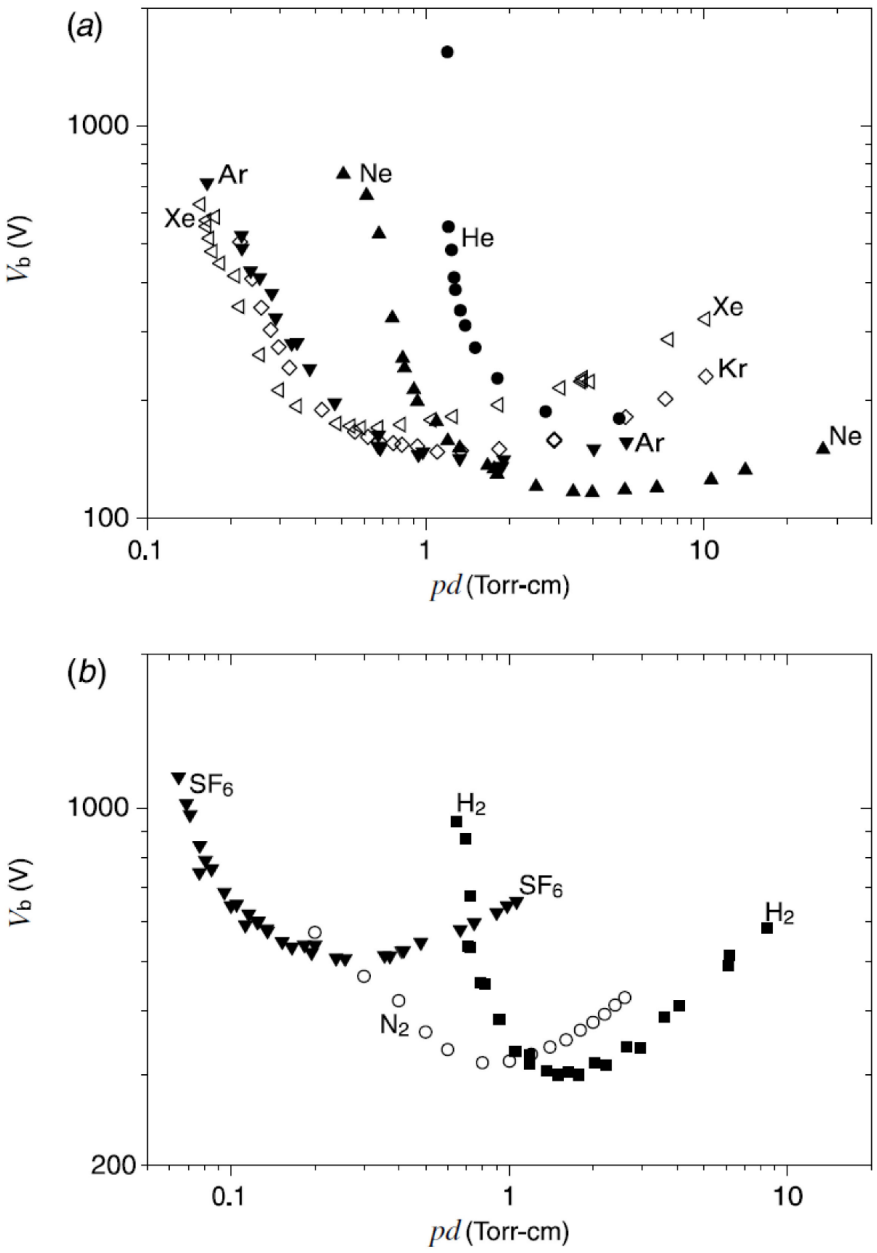


Figure 1.3 Breakdown voltage for plane-parallel electrodes at 20 ˚C for (a) noble gas and (b) common gas. Adapted from [8] and data from [9].

1.6 Plasma-Liquid Interactions

Plasma-liquid systems, like gas-phase plasmas, can be categorized by power source and reactor configuration. Common configurations include: (1) discharges formed within the bulk

liquid; (2) discharges in which the liquid serves as an electrode (grounded or biased), with either galvanic or capacitive coupling; (3) surface discharges initiated at the gas-liquid interface; and (4) dispersed-phase systems involving gas bubbles in liquid or liquid droplets/bubbles in a gas stream. Examples are shown in Figure 1.4.[10] Its applications include nanomaterials synthesis,[11-12] analytical chemistry,[13-14] material processing,[15-16] the decomposition of harmful compounds in water including per- and polyfluoroalkyl substances (PFAS) removal,[17] medical and agricultural applications,[18] as well as enabling polymerization reactions.[19-20]

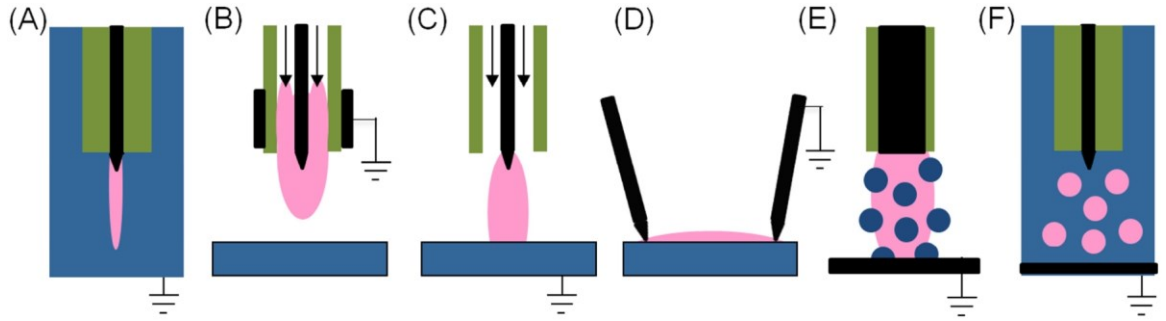


Figure 1.4 Schematic of discharge types used in plasma-liquid interactions: (A) direct discharge in liquid; (B)-(D) gas-phase discharges; and (E) and (F) multiphase discharges. Details: (B) plasma jet without direct contact with the liquid; (C) gas-phase plasma with a liquid electrode; (D) surface discharge; (E) gas-phase plasma with a dispersed liquid phase (aerosols); (F) discharges in bubbles. Adapted from [10].

In this dissertation, we focused on configuration (c) in Figure 1.4, in which the liquid phase is connected to a grounding electrode and is electrically coupled to the discharge. In this configuration, charge transfer occurs at the plasma-liquid interface. The resulting physicochemical complexity is summarized in Figure 1.5, which depicts the primary reactions and transport processes expected for an argon (Ar)/H_2O system. As we outlined the plasma-phase kinetics above, the discussion here emphasizes interfacial phenomena and the resulting aqueous-phase chemistry.

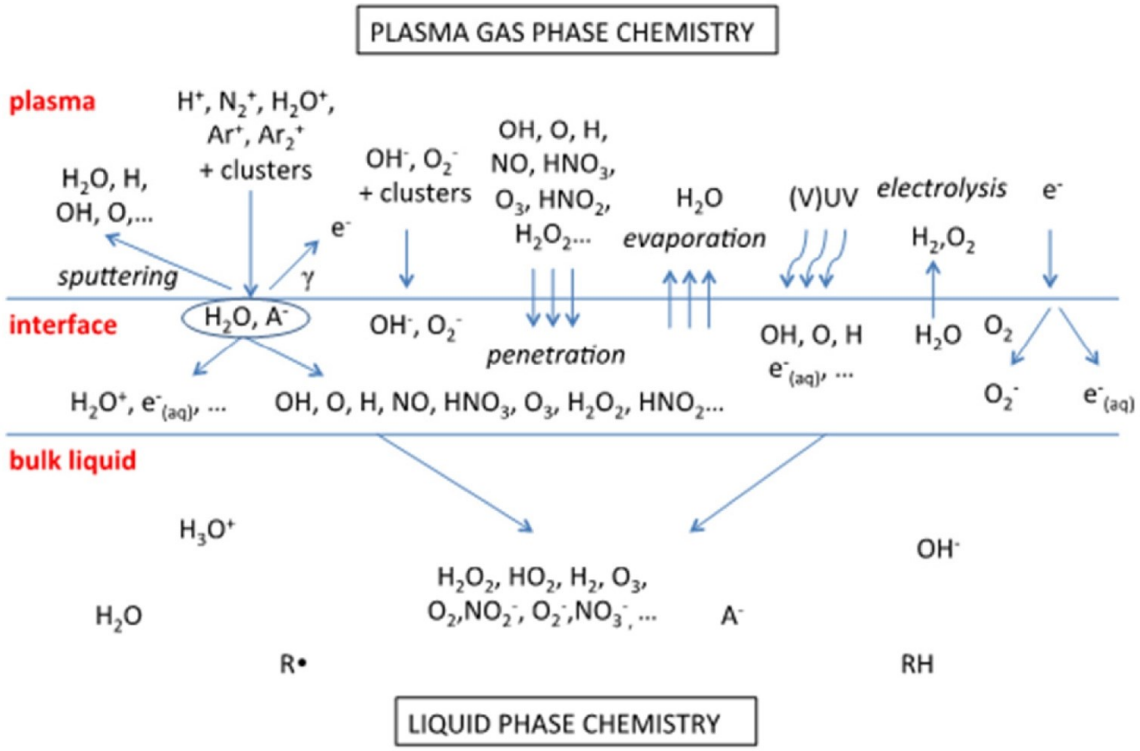


Figure 1.5 Schematic diagram of some of the most important species and mechanisms for an Ar/humid air plasma in contact with water. Adapted from [10].

1.7 Faradaic and Non-Faradaic Processes

At the plasma-liquid interface, interfacial interactions can be grouped into Faradaic (charge-transfer) and non-Faradaic (non-charge-transfer) processes. Because the liquid is incorporated into the external circuit, interfacial charge transfer is expected. In the Faradaic pathway, electrons (and, in some cases, ions) transfer cross the interface, which rapidly solvate to form solvated electrons (e_{sol}^-). They then react with dissolved solutes or with the solvent itself to initiate subsequent liquid phase chemistry. In this dissertation, the terms hydrated electrons (e_{aq}^-) and e_{sol}^- are both used; the former refers specifically to solvated electrons in aqueous solution. In chapters involving non-aqueous solvents, the term "solvated electron" is used.

At the plasma-liquid interface, ionic bombardment depends on interfacial polarity. In a liquid-anode configuration, the anode sheath accelerates electrons toward the liquid; negative ions are generally not the dominant charge carriers at the interface. In contrast, in a liquid-cathode configuration, the cathode sheath accelerates cations toward the liquid surface, which can induce secondary-electron emission and additional interfacial reactions. These ions may also become solvated and enter the liquid phase as ionic species. In both configurations, because electrons have much higher mobility than ions, they are typically considered the primary charge carriers. Although ionic fluxes contribute less to charge transport, they are important for sputtering, producing reactive intermediates, and facilitating mass transfer across the plasma-liquid interface. The liquid-cathode configuration will be further discussed due to its complexity and intriguing reaction mechanisms.

The non-Faradaic processes generally involve the mass transfer of neutral species and photolysis, which are not charge-transfer driven. Transfer of neutral species can happen in both directions. This is often described through the concentration or activity differences between the two phases. From the plasma phase to the liquid phase, high-energy species, such as oxygen atom (•O), hydroxyl radicals (•OH), and nitrogen monoxide (NO), may be generated in the plasma phase, which depends on the gas and liquid compositions. These species then transfer into the liquid phase due to concentration gradients. This phenomenon is commonly described using Henry's law.[21] Although it is commonly used, its applicability has been questioned by several works.[22-23] First, Henry's law assumes equilibrium at the interface, which might not always be the case in transient timescale. Also, additional mass transfer processes other than free diffusion (e.g., convection) can occur.[24] Still, it provides a useful estimate of the boundary condition at the plasma-liquid interface. On top of that, liquid phase species, especially volatile

solvents, can evaporate and participate in plasma phase reactions. Mass transfer between the two phases is generally enhanced through bobbling that purges gas through a glass frit or small orifices at the interface. This increases the interfacial surface area and creates microbubbles/droplets in both phases with unique chemistry.[25-26]

Photolysis at the plasma-liquid interface results from the ultraviolet (UV) emission in the plasma phase, generated by the recombination of electrons and ions, along with the relaxation of excited molecules. These photons drive reactions, including the generation of e_{sol}^- and water ions, along with the dissociation of water molecules into hydrogen radical (•H) and •OH.[27] UV photons might also drive reaction pathways distinct from those initiated by electrons at the plasma-liquid interface, which provides special design principles to the interface.[28]

1.8 Plasma-Liquid Sheath

The plasma-liquid sheath is the thin, partially charged layer that forms at the interface between a plasma and a liquid surface, where the quasi-neutrality of free electrons and ions is disrupted. This layer is distinct from sheaths at plasma-solid interfaces because of two-phase interactions, including evaporation, surface deformation, droplet ejection, and electric double layer.[29] These influence the interfacial charge distribution and the composition of both phases. The sheath structure and properties vary with the liquid and the applied bias, producing either a positively charged ion sheath (at a cathode) or a more complex electron sheath (at an anode).

The sheath sets the local electric field and thus the kinetic energy distributions of charged species (ions and electrons) bombarding the liquid surface. Energy transfer from these fast incident particles can induce secondary-electron emission from the liquid phase and trigger cascading reactions. In a typical ion sheath at a negatively biased surface (cathode), the field accelerates positive ions toward the liquid; conversely, an anode sheath accelerates electrons

toward the liquid. This acceleration shifts the charged particle energy distributions to higher values, which is critical for determining the nature and extent of subsequent chemical and physical interactions. This electrical coupling is covered in a review paper.[30]

1.9 Plasma-Driven Solution Electrolysis

Plasma-Driven Solution Electrolysis (PDSE) is a method that induces liquid-phase chemical transformations by exploiting interactions between gas-phase plasmas and liquids. This approach can be viewed as replacing a conventional metal electrode in an electrolytic cell with a gas-phase plasma, yielding a form of "electrodeless" electrochemistry. The analogy is motivated by the occurrence of charge transfer and coupling within the same electrical circuit. Still, some researchers argue that plasma electrochemistry shares more fundamental similarities with radiation chemistry than with conventional electrochemistry. While conventional electrochemistry relies primarily on interfacial charge transfer, both plasma electrochemistry and radiation chemistry involve high-energy processes that generate reactive radicals, initiating cascading reactions.[31] A typical scheme is presented in Figure 1.6, and a comparison with conventional electrochemistry is listed in Table 1.1.

PDSE is driven by the transfer of energetic species produced by the plasma, including electrons, ions, radicals, and photons, which generate a highly reactive interfacial liquid layer. PDSE holds significant promise for selective, efficient, and green chemical transformations, such as nanoparticle and polymer synthesis, and for leveraging renewable electricity to enable more sustainable chemical conversion. However, many PDSE-driven processes are notably challenged by transport limitations arising from the short lifetimes and limited penetration depths of these highly reactive species. Our group and collaborators have published review papers on this topic.[32-33]

Table 1.1 A comparison of conventional electrochemistry with PDSE highlights the main differences between the two systems. Adapted from [32]

	Conventional electrochemistry	**PDSE**
Charge transfer driven by	The difference in Fermi level between the electrode and the solution	Plasma-generated high-energy species (electrons, ions, photons, radicals, etc.)
Penetration depth and lifetime	Generally, not considered due to charge transfer only occurring at the electrode solution interface	Determined by the liquid environment, the nature and energy of the energetic species, the transport and lifetime of the species
Reaction rate for a given redox couple	Determined by the electrode potential, the electrode material, diffusion, and the nature of the redox couple in the solution	Determined by the flux of high-energy species, transport, and rate constants of the redox reaction

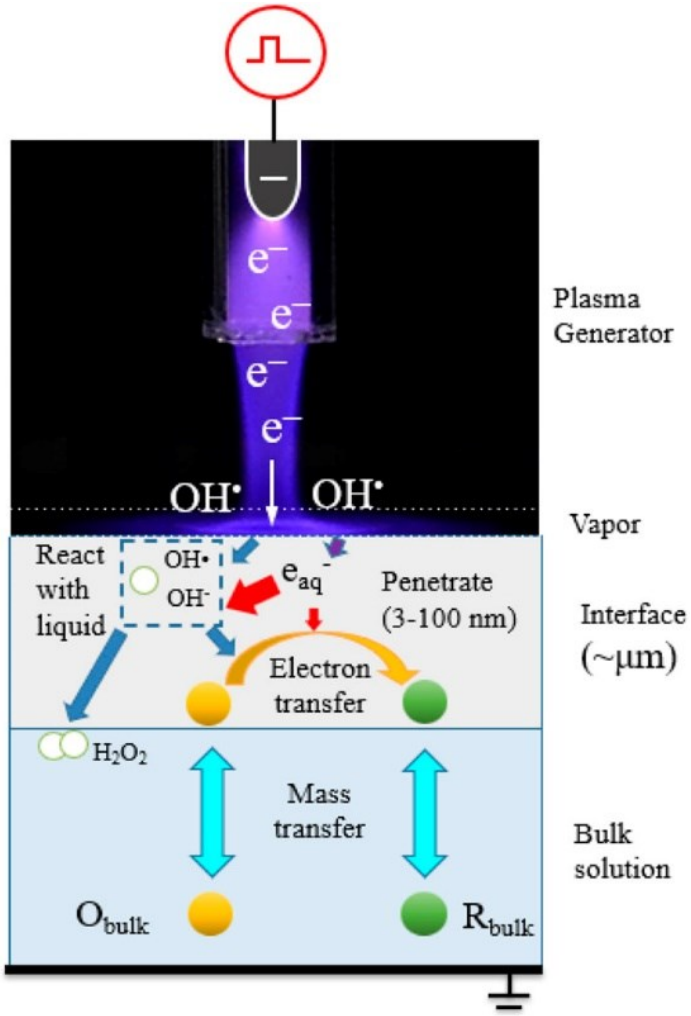


Figure 1.6 Schematic representation of selected redox processes underpinning PDSE. Adapted from [32].

1.10 Conventional Electrochemistry

As PDSE is often compared with a conventional electrochemical system, and as several electrochemical measurements were performed in this dissertation, conventional electrochemistry will be discussed. Electrochemistry is the branch of chemistry focused on the interrelation between electrical and chemical effects. This involves the study of chemical reactions caused by the charge transfer of electric current and the production of electrical energy by chemical reactions. The discipline integrates fundamental components such as

thermodynamics (chemical potential), electron-transfer kinetics on an electrode surface, and mass transfer at the electrode surface and within the electrolyte.[34] Here, we discuss the charge transfer mechanism at the electrode-electrolyte interface.

1.11 Charge Transfer and Equilibrium

At the electrode-electrolyte interface, charge transfer proceeds via Faradaic processes, which entail the electron transfer across the interface (oxidation or reduction). Faradaic transfer is driven by the applied electric potential, which controls the energy level (Fermi level) of electrons in the electrode. By manipulating this potential, the charge transfer direction can be controlled, either from the electrode to the LUMO (lowest unoccupied molecular orbital) or from the HOMO (highest occupied molecular orbital) of the redox couple to the electrode. In Figure 1.7, the energy level of electrons in an electrode and the HOMO and LUMO of a redox couple are illustrated.

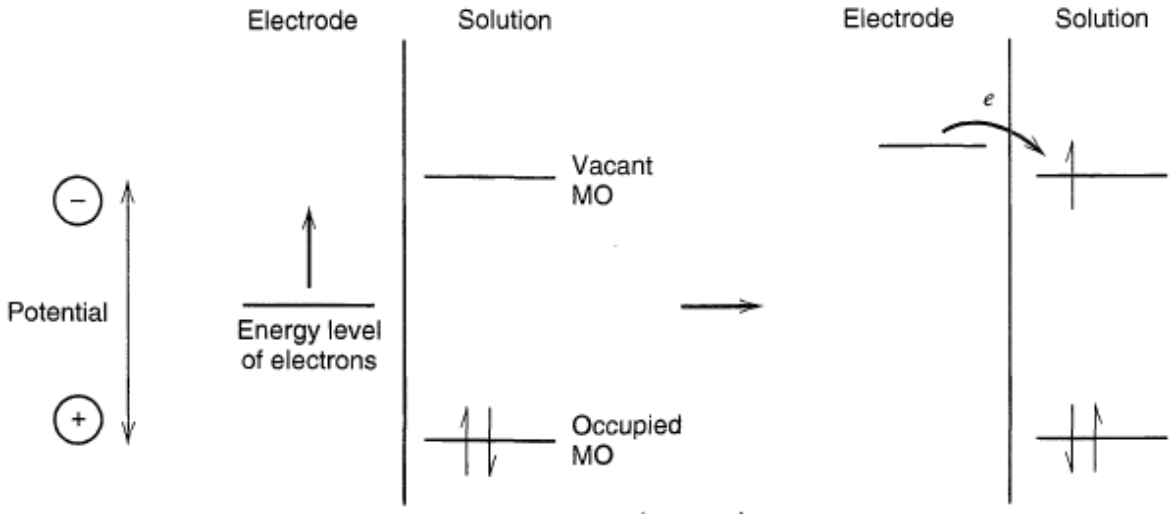


Figure 1.7 Representation of a reduction reaction, which presents the energy level of electrons in an electrode and the molecular orbitals (MO) of an adsorbed species. Electrons move from the electrode to the LUMO of the species. Adapted from [34].

Given this scheme, equilibrium at the electrode surface represents a state of thermodynamic balance. This balance is a dynamic process where the rates of the forward (reduction) and backward (oxidation) reactions are equal and opposite, resulting in zero net current. This state occurs at the equilibrium potential and is characterized for reversible systems by the Nernst equation (Equation 1.2), which links the electrode potential to the surface activities (or concentrations) of the oxidized (O) and reduced (R) species. In Equation 1.2, E stands for the reduction potential, E^0 stands for the formal potential, F stands for the Faraday constant, R stands for the ideal gas constant, n stands for the number of electrons transferred, T stands for the temperature, and C_R and C_O stand for the concentrations of the reduced and oxidized forms, respectively.

$$\mathrm{E} = E^0 - \frac{RT}{nF} \ln\left(\frac{C_R}{C_O}\right) \text{ (Equation 1.2)}$$

The reduced and oxidized forms of a species are collectively called a redox couple. For a well-defined redox couple, E, the reduction potential, is governed by the ratio of the reduced to the oxidized forms, which also corresponds to the relative occupancies of the HOMO and LUMO. Therefore, when an electrode reaches an equilibrium with a redox couple with a net current of zero, the potential is defined as the open-circuit potential (OCP). At that potential, the electrode Fermi level equals the average electron energy level of the redox couple; that is, the OCP equals the reduction potential E.[35]

1.12 Current versus Applied Potential

When the applied electrode potential deviates from the defined E, a net current, and thus a net direction of reduction or oxidation of the redox couple, may occur at the electrode surface. The relationship between the current and the applied potential is described by the Butler-Volmer Equation, which quantitatively relates the net Faradaic current (I) to the overpotential (η). η is

the difference between the applied potential at the electrode and the reduction potential of the redox couple. In its common form, it describes the rate of a simple, one-step electron transfer process under conditions where mass-transfer effects are negligible. The full Butler-Volmer expression gives the net current as the difference between the cathodic (reduction) and anodic (oxidation) components, whose rate constants (k) depend exponentially on η. This equation is widely used in electrochemistry to treat heterogeneous kinetics, since it simplifies into the Tafel equation at large overpotentials and to a linear relationship at small overpotentials.

In Equation 1.3, I stands for the current, n stands for the number of electron transferred, A stands for the electrode area, k^0 stands for standard rate constant, $C_O(0,t)$ and $C_R(0,t)$ stand for the concentrations of the oxidized and reduced forms at time t at x = 0 (electrode surface), α stands for the charge transfer coefficient, and η stands for the overpotential. It should also be noted that the reduction potentials are based on thermodynamic considerations. Slow kinetics might prevent a reaction from occurring at a significant rate within a given potential region. The potential region is called a potential window, and the potential at which a reaction first becomes measurable is called an onset reduction potential, which will be further discussed.

$$\mathrm{I} = \mathrm{n}FAk^0\left(C_O(0,t)e^{\frac{-\alpha nF\eta}{RT}} - C_R(0,t)e^{\frac{(1-\alpha)nF\eta}{RT}}\right) \text{ (Equation 1.3)}$$

1.13 Dissertation Scope

In this chapter, we covered the topics and the background of this dissertation. To understand PDSE, all three aspects are essential for interpreting multiphase interactions and decoupling the phenomena. Electrochemical tools and the analogy to the electrochemistry of PDSE contribute to this dissertation, likely more than plasma-phase phenomena.

In Chapter 2, we introduce the methods and experimental setups in this dissertation. This involves the setup of the electrochemical tools, the setup and the operational procedures for

pulsed DC plasma configurations with negative and positive plasma polarities, the setup of gas chromatography-mass spectrometry, and the characterization tools of the nanoparticles. Technical details and relevant background are discussed in this chapter.

In Chapter 3, we use an electrochemical tool to study PDSE. Even though the plasma-liquid interface is often compared to an "electrodeless" interface, the two fields use terminology in different ways or drift from their original meanings. Here, we employ a redox couple with a well-defined electrochemical potential to compare PDSE with conventional electrochemical systems. We show that, under certain conditions, PDSE yields net-zero conversion of a redox couple at the interface due to the simultaneous presence of reducing and oxidizing agents. Although this net-zero conversion resembles the equilibrium between an electrode and a redox couple in conventional electrochemistry, in PDSE it is driven by high-energy species. Thus, PDSE deviates from a conventional electrochemical system. Building on this insight, we propose an electrochemical approach that utilizes the PDSE net-zero condition to quantify the relative effective concentration ratios of these high-energy species.

In Chapter 4, as we establish that high-energy species exist at the plasma-liquid interface, we utilize PDSE to synthesize bimetallic alloy nanoparticles. These nanoparticles are challenging to synthesize through coreduction in one pot due to the intrinsic immiscibility of the two metals. From this chapter, we develop three requirements to form these nanoparticles: fast reduction rates of metal precursors, comparable reduction rates for both precursors, and the nucleation control to exclusively form alloy nanoparticles. PDSE meets these requirements by offering high reduction rates and precise control of reaction time to short pulses, which are difficult to achieve with conventional thermal systems.

In Chapter 5, we revisit the charge transfer reaction mechanism in the plasma-anode (positive polarity) configuration. It is commonly believed that observed oxidation reaction under this configuration results from cascading reactions with the formation of •OH as an intermediate. •OH forms via cation-induced ionization and water dissociation, driven by charge transfer to water. Here, we add isopropyl alcohol (IPA), which exhibits a lower O-H bond dissociation enthalpy change than that of water, to test the hypothesis. We find that scavenging •OH does not affect the IPA consumption rate, contradicting the view that •OH is responsible for all oxidation reactions.

In Chapter 6, we summarize the findings, provide some critique in hindsight and in reflection, and outline possible future directions for the field.

1.14 References

1. da Silva, C. L.; Sonnenfeld, R. G.; Edens, H. E.; Krehbiel, P. R.; Quick, M. G.; Koshak, W. J., The Plasma Nature of Lightning Channels and the Resulting Nonlinear Resistance. *Journal of Geophysical Research: Atmospheres* **2019,** *124* (16), 9442-9463.

2. Girard, P.; Köppen, J.; Acker, A., Chemical Compositions and Plasma Parameters of Planetary Nebulae with Wolf-Rayet and Wels Type Central Stars. *Astronomy & Astrophysics* **2007,** *463* (1), 265-274.

3. Bruggeman, P. J.; Iza, F.; Brandenburg, R., Foundations of Atmospheric Pressure Non-Equilibrium Plasmas. *Plasma Sources Science and Technology* **2017,** *26* (12), 123002.

4. Pitchford, L. C.; Alves, L. L.; Bartschat, K.; Biagi, S. F.; Bordage, M.-C.; Bray, I.; Brion, C. E.; Brunger, M. J.; Campbell, L.; Chachereau, A.; Chaudhury, B.; Christophorou, L. G.; Carbone, E.; Dyatko, N. A.; Franck, C. M.; Fursa, D. V.; Gangwar, R. K.; Guerra, V.; Haefliger, P.; Hagelaar, G. J. M.; Hoesl, A.; Itikawa, Y.; Kochetov, I. V.; McEachran, R. P.; Morgan, W.

L.; Napartovich, A. P.; Puech, V.; Rabie, M.; Sharma, L.; Srivastava, R.; Stauffer, A. D.; Tennyson, J.; de Urquijo, J.; van Dijk, J.; Viehland, L. A.; Zammit, M. C.; Zatsarinny, O.; Pancheshnyi, S., LXCat: An Open-Access, Web-Based Platform for Data Needed for Modeling Low Temperature Plasmas. *Plasma Processes and Polymers* **2017,** *14* (1-2), 1600098.

5. Pancheshnyi, S.; Biagi, S.; Bordage, M. C.; Hagelaar, G. J. M.; Morgan, W. L.; Phelps, A. V.; Pitchford, L. C., The LXCat Project: Electron Scattering Cross Sections and Swarm Parameters for Low Temperature Plasma Modeling. *Chemical Physics* **2012,** *398*, 148-153.

6. Carbone, E.; Graef, W.; Hagelaar, G.; Boer, D.; Hopkins, M. M.; Stephens, J. C.; Yee, B. T.; Pancheshnyi, S.; van Dijk, J.; Pitchford, L., Data Needs for Modeling Low-Temperature Non-Equilibrium Plasmas: The LXCat Project, History, Perspectives and a Tutorial. *Atoms* **2021,** *9* (1), 16.

7. Go, D. B., Ionization and Ion Transport. In *A primer for the study of non-equilibrium, low-temperature gas discharges and plasmas* [Online] Morgan & Claypool Publishers: 2018. https://doi.org/10.1088/978-1-6817-4601-2.

8. Michael A. Lieberman, A. J. L., Direct Current (DC) Discharges. In *Principles of Plasma Discharges and Materials Processing*, John Wiley & Sons, Inc.: 2005; pp 535-569.

9. Mariotti, D.; McLaughlin, J. A.; Maguire, P., Experimental Study of Breakdown Voltage and Effective Secondary Electron Emission Coefficient for a Micro-Plasma Device. *Plasma Sources Science and Technology* **2004,** *13* (2), 207.

10. Bruggeman, P. J.; Kushner, M. J.; Locke, B. R.; Gardeniers, J. G. E.; Graham, W. G.; Graves, D. B.; Hofman-Caris, R. C. H. M.; Maric, D.; Reid, J. P.; Ceriani, E.; Fernandez Rivas, D.; Foster, J. E.; Garrick, S. C.; Gorbanev, Y.; Hamaguchi, S.; Iza, F.; Jablonowski, H.; Klimova, E.; Kolb, J.; Krcma, F.; Lukes, P.; Machala, Z.; Marinov, I.; Mariotti, D.; Mededovic

Thagard, S.; Minakata, D.; Neyts, E. C.; Pawlat, J.; Petrovic, Z. L.; Pflieger, R.; Reuter, S.; Schram, D. C.; Schröter, S.; Shiraiwa, M.; Tarabová, B.; Tsai, P. A.; Verlet, J. R. R.; von Woedtke, T.; Wilson, K. R.; Yasui, K.; Zvereva, G., Plasma–Liquid Interactions: A Review and Roadmap. *Plasma Sources Science and Technology* **2016,** *25* (5), 053002.

11. Chen, Q.; Li, J.; Li, Y., A Review of Plasma–Liquid Interactions for Nanomaterial Synthesis. *Journal of Physics D: Applied Physics* **2015,** *48* (42), 424005.

12. Maguire, P.; Rutherford, D.; Macias-Montero, M.; Mahony, C.; Kelsey, C.; Tweedie, M.; Pérez-Martin, F.; McQuaid, H.; Diver, D.; Mariotti, D., Continuous in-Flight Synthesis for on-Demand Delivery of Ligand-Free Colloidal Gold Nanoparticles. *Nano Letters* **2017,** *17* (3), 1336-1343.

13. Rosen, A. L.; Hieftje, G. M., Inductively Coupled Plasma Mass Spectrometry and Electrospray Mass Spectrometry for Speciation Analysis: Applications and Instrumentation. *Spectrochimica Acta Part B: Atomic Spectroscopy* **2004,** *59* (2), 135-146.

14. Smoluch, M.; Mielczarek, P.; Silberring, J., Plasma-Based Ambient Ionization Mass Spectrometry in Bioanalytical Sciences. *Mass Spectrometry Reviews* **2016,** *35* (1), 22-34.

15. Ishijima, T.; Nosaka, K.; Tanaka, Y.; Uesugi, Y.; Goto, Y.; Horibe, H., A High-Speed Photoresist Removal Process Using Multibubble Microwave Plasma under a Mixture of Multiphase Plasma Environment. *Applied Physics Letters* **2013,** *103* (14),

16. Friedrich, J. F.; Mix, R.; Schulze, R.-D.; Meyer-Plath, A.; Joshi, R.; Wettmarshausen, S., New Plasma Techniques for Polymer Surface Modification with Monotype Functional Groups. *Plasma Processes and Polymers* **2008,** *5* (5), 407-423.

17. Singh, R. K.; Fernando, S.; Baygi, S. F.; Multari, N.; Thagard, S. M.; Holsen, T. M., Breakdown Products from Perfluorinated Alkyl Substances (PFAS) Degradation in a Plasma-Based Water Treatment Process. *Environmental Science & Technology* **2019,** *53* (5), 2731-2738.

18. Domonkos, M.; Tichá, P.; Trejbal, J.; Demo, P., Applications of Cold Atmospheric Pressure Plasma Technology in Medicine, Agriculture and Food Industry. *Applied Sciences* **2021,** *11* (11), 4809.

19. Sengupta, S. K.; Sandhir, U.; Misra, N., A Study on Acrylamide Polymerization by Anodic Contact Glow-Discharge Electrolysis: A Novel Tool. *Journal of Polymer Science Part A: Polymer Chemistry* **2001,** *39* (10), 1584-1588.

20. Tan, P. E. C.; Mahinay, C. L. S.; Culaba, I. B.; Streeter, O. K. M.; Hilario, M. R. A., Plasma Polymerization of Styrene Using an Argon-Fed Atmospheric Pressure Plasma Jet. *Journal of Vacuum Science & Technology B* **2018,** *36* (4),

21. Zheng, Y.; Wang, L.; Bruggeman, P., Modeling of an Atmospheric Pressure Plasma-Liquid Anodic Interface: Solvated Electrons and Silver Reduction. *Journal of Vacuum Science & Technology A* **2020,** *38* (6), 063005.

22. Heirman, P.; Bogaerts, A., Critical Comparison of Interfacial Boundary Conditions in Modelling Plasma–Liquid Interaction. *Journal of Physics D: Applied Physics* **2025,** *58* (8), 085206.

23. Dickenson, A.; Walsh, J. L.; Hasan, M. I., Electromechanical Coupling Mechanisms at a Plasma–Liquid Interface. *Journal of Applied Physics* **2021,** *129* (21),

24. Stapelmann, K.; Gershman, S.; Miller, V., Plasma–Liquid Interactions in the Presence of Organic Matter—a Perspective. *Journal of Applied Physics* **2024,** *135* (16),

25. Lee, D.; Chen, H.-T.; Linic, S., Plasma-Induced Selective Propylene Epoxidation Using Water as the Oxygen Source. *JACS Au* **2023,** *3* (4), 997-1003.

26. Ho, J.; Hershey, M.; Swearer, D. F., Accelerated Carbon Dioxide Mineralization and Polymorphic Control Facilitated by Nonthermal Plasma Bubbles. *Physical Chemistry Chemical Physics* **2025,** *27* (31), 16435-16446.

27. Heit, G.; Neuner, A.; Saugy, P.-Y.; Braun, A. M., Vacuum-UV (172 nm) Actinometry. The Quantum Yield of the Photolysis of Water. *The Journal of Physical Chemistry A* **1998,** *102* (28), 5551-5561.

28. Xu, C.; Andaraarachchi, H. P.; Kortshagen, U. R., Synthesis of Composition-Tunable Ag-Cu Bimetallic Nanoparticles through Plasma-Driven Solution Electrolysis. *Nanomaterials* **2024,** *14* (21), 1758.

29. Vanraes, P.; Bogaerts, A., The Essential Role of the Plasma Sheath in Plasma–Liquid Interaction and Its Applications—a Perspective. *Journal of Applied Physics* **2021,** *129* (22),

30. Vanraes, P.; Bogaerts, A., Plasma Physics of Liquids—a Focused Review. *Applied Physics Reviews* **2018,** *5* (3),

31. Bloomquist, C. K.; Naumov, D.; Yang, A.; Mathison, R.; Herzog, B. D.; Tenn, W. J., III; Modestino, M. A.; Aydil, E. S., Exploring the Balance between Faradaic and Non-Faradaic Processes in Organic Chemical Reactions at Plasma-Liquid Interfaces. *Journal of the American Chemical Society* **2025,** *147* (16), 13937-13947.

32. Bruggeman, P. J.; Frontiera, R. R.; Kortshagen, U.; Kushner, M. J.; Linic, S.; Schatz, G. C.; Andaraarachchi, H.; Chaudhuri, S.; Chen, H.-T.; Clay, C. D.; Dias, T. C.; Doyle, S.; Jones, L. O.; Meyer, M.; Mueller, C. M.; Nam, J. H.; Raisanen, A.; Rich, C. C.; Srivastava, T.; Xu, C.; Xu,

D.; Zhang, Y., Advances in Plasma-Driven Solution Electrochemistry. *The Journal of Chemical Physics* **2025,** *162* (7),

33. Bruggeman, P. J.; Frontiera, R. R.; Kortshagen, U. R.; Kushner, M. J.; Linic, S.; Schatz, G. C.; Andaraarachchi, H.; Exarhos, S.; Jones, L. O.; Mueller, C. M.; Rich, C. C.; Xu, C.; Yue, Y.; Zhang, Y., Plasma-Driven Solution Electrolysis. *Journal of Applied Physics* **2021,** *129* (20), 200902.

34. Bard, A. J.; Faulkner, L. R., *Electrochemical Methods: Fundamentals and Applications*. Sec. ed.; John Wiley & Sons: New York, 2001.

35. Boettcher, S. W.; Oener, S. Z.; Lonergan, M. C.; Surendranath, Y.; Ardo, S.; Brozek, C.; Kempler, P. A., Potentially Confusing: Potentials in Electrochemistry. *ACS Energy Letters* **2021,** *6* (1), 261-266.

Chapter 2 Experimental Methods

2.1 Summary

In this chapter, we provide a detailed description of the plasma system, present rate constants for common liquid-phase reactions, explain the electrochemical tools, briefly outline material characterization tools, and describe a method for detecting gas-phase concentrations. The plasma system is used across the following three chapters. We include descriptions of the following equipment: plasma jet, plasma reactors, high-voltage pulser, high-voltage power supply (negative and positive polarities), waveform generator, current detector (Rogowski wire), and signal recorder (oscilloscope).

The reaction constants and scavengers for aqueous solutions are further discussed in Chapters 3 and 5. Comparing rate constants rationalizes the choice of scavengers and suggests possible pathways for high-energy species in the liquid phase. The electrochemical tools are utilized in Chapters 3 and 4. In Chapter 3, they are utilized to understand redox couple behaviors, while in Chapter 4, they are used to determine the onset reduction potentials of the precursors. The materials characterization tools are used in Chapter 4. The gas-phase concentration detection is used in Chapter 5, where we measure the gas-phase concentrations of two molecules and correlate them to their liquid-phase concentrations. Additional details for specific projects are further described in their own chapters.

2.2 Plasma Reactors

In this dissertation, we mainly focus on a pulsed direct current (DC) plasma with helium (He) gas. He flow is essential for lowering the breakdown voltage compared to the atmosphere and decreasing the vapor content. When the flow rate decreases or the water content increases, the breakdown voltage increases significantly. In our lab, we developed two types of plasma-liquid reactors, compared in the table below (Table 2.1). The primary difference between the two systems is the charge transfer. In the reactor with a glass frit, the grounding electrode is installed around the glass frit, which introduces bubbles and separates the plasma and liquid phases. As a result, current is more likely to flow directly to the grounding electrode rather than into the liquid phase. The high electrical resistance of the deionized water might also play a role. Therefore, in the system with a glass frit, we usually do not consider the effect of charge transfer from the plasma phase to the liquid phase. It is also noted that the plasma system with a glass frit can utilize the tungsten needle as a cathode or as an anode, respectively, by switching the polarity. For the plasma-anode setup, the breakdown voltages were usually higher for the same frequency, current, and pulse width than those of the plasma-cathode setup. The hydrogen peroxide (H_2O_2) production was achievable with both polarities.

The glass frit has three types, depending on the size of the pores of the glass frit, including coarse, medium, and fine. The coarse one has the largest average pore size, which also results in the lowest pressure drop while purging He across the glass frit. The fine one has the smallest average pore size and the highest pressure drop while purging He. The choice of these three types of glass frit affects the liquid phase moisture and also the pressure buildup in the plasma phase for a He and water plasma system. Due to the size of the bubbles, the gas-to-liquid interfacial surface area should also vary. Overall, a glass frit alters the plasma parameters, the

breakdown voltages, and the gas-to-liquid phase mass transfer. It is also noted that the glass frit surface might quench reactive species and contribute to the prevention of deep oxidation reactions.

Table 2.1 Comparison between two pulsed DC plasma systems.

Reactor Type	Phases	Charge Transfer	Plasma Type
Plasma-liquid system with a glass frit	Gas and liquid	Not applicable	Pulsed DC plasma
Pulsed DC plasma-liquid reactor	Gas and liquid	Plasma-liquid interface	Pulsed DC plasma

In Figure 2.1, the scheme depicts a plasma-liquid system with a glass frit. In the setup, reactant molecules are converted into highly energetic reactive species (ions, radicals, and excited molecules) in the plasma phase. Subsequently, these reactive species are then transferred into the liquid phase, where they dissolve or react with liquid-phase species. At the plasma-liquid interface, a glass frit, a high-surface-area porous silica structure, is installed to limit mass transfer from the liquid phase to the plasma phase (it is often undesirable to expose liquid-phase species to the high-energy plasma) while simultaneously increasing the plasma-liquid interfacial area. It should also be noted that long-lived species, such as H_2O_2, are more likely to be transferred through a glass frit. We also observed that when the liquid phase temperature increased, the breakdown voltage also increased, likely due to the water content increase in the plasma phase. Therefore, the liquid phase still affects the gas phase reactions even with the installation of a glass frit. The selectivity improvement might result from the pressure drop across the porous structure and the quenching effect of the glass frit surface to the short-lived species.

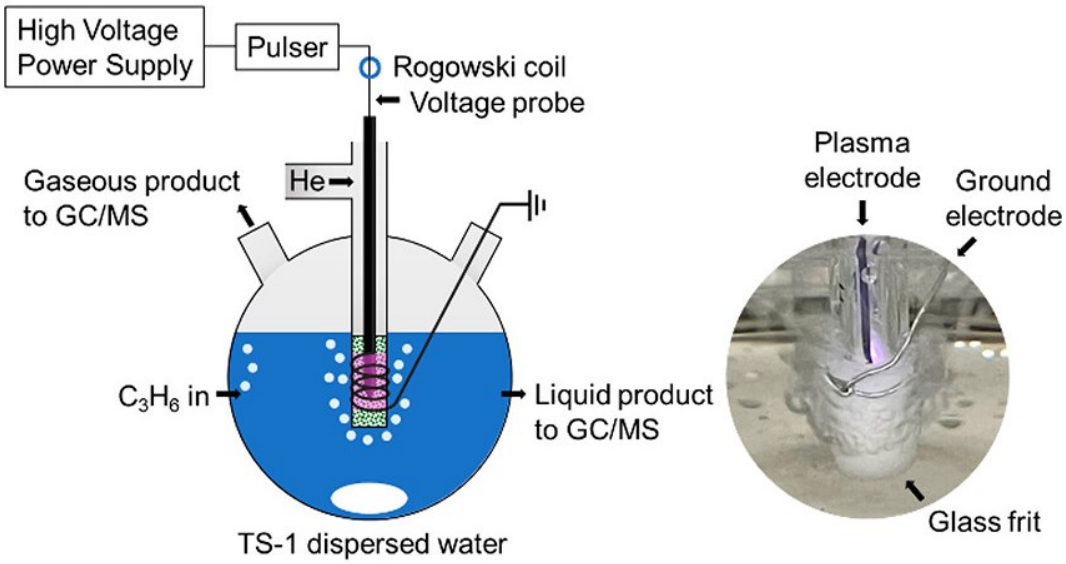


Figure 2.1 Schematic of the plasma reactor setup (left) developed for hydrogen peroxide propylene epoxidation with high selectivity and photo of the plasma discharge in water (right). A glass frit is installed at the plasma-liquid interface. Adapted from [1].

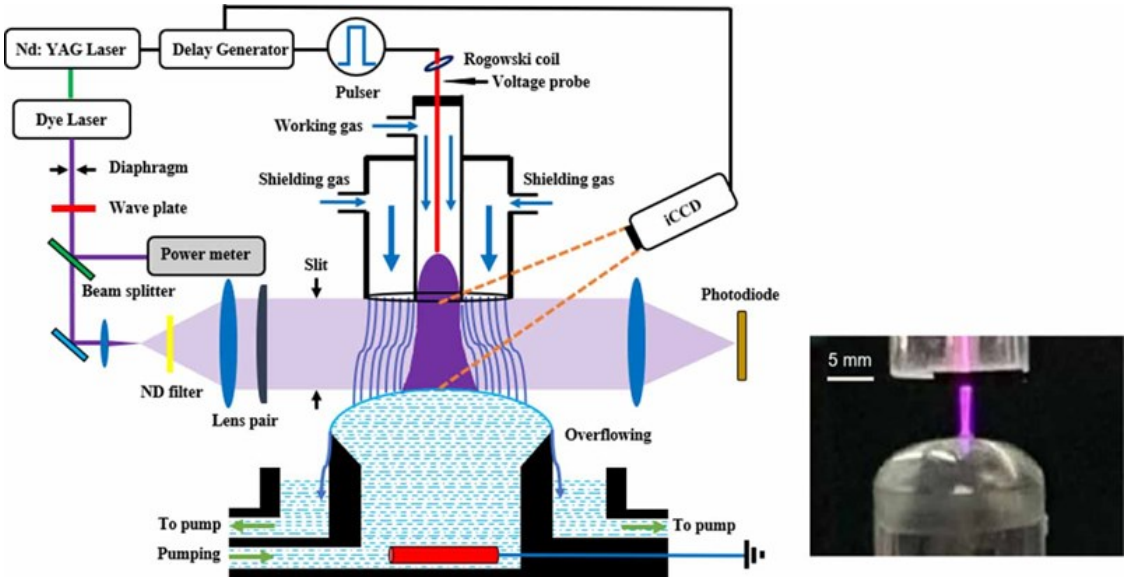


Figure 2.2 Schematic of a pulsed DC plasma-liquid reactor. In this graph, the working gas is He with an applied voltage of -3.5 kV. The plasma pulse width is 5 μs. Adapted from [2].

The other reactor setup explicitly involves charge transfer. In this case, the plasma serves as either a cathode or an anode, depending on the circuit. The closet system we used was

reported previously, plotted in Figure 2.2.[2] An inert electrode is often used as a grounding electrode, which is placed far away from the plasma-liquid interface. Common electrode choice includes platinum (Pt) wires, graphite rods, or gold wires. Under this configuration, ion currents in the electrolyte maintain charge neutrality in the liquid phase, making the system closer to a conventional electrochemical cell. In addition to charge-transfer-induced reactions, other high-energy species also transfer into the liquid phase and drive reactions. For example, in a plasma-cathode configuration, solvated electrons (e_{sol}^-) and hydroxyl radicals (•OH) are transferred into the liquid phase with a pulsed DC plasma. During the pulse on-time, e_{sol}^- dominate and drive reduction reactions. While the pulse off-time, •OH has a longer lifetime both in the liquid phase and in the plasma phase, becoming the dominant reactant that drives oxidation reactions. This alternation rapidly switches the interface from reductive to oxidative, creating a unique interface and expanding reaction possibilities. We also established that charge-transfer induced reactions, such as the plasma-anode induced H_2O_2 production, are not compatible with a glass frit. It might result from the quenching of •OH radicals at the glass frit surface or the recombination of •OH and hydrogen radical (•H) to water, although the actual mechanism remains unclear.

We also use two types of gas flow configurations. In Chapters 3 and 4, we use a quartz capillary tube with a 2 mm inner diameter (first setup). In this case, we usually use a high flow rate of He, which is also connected to the plasma jet box. The tube is inserted in to a connected tunnel and installed with O-rings. It is often used with a shielding gas to avoid the effect of the atmosphere that forms reactive nitrogen and oxygen species. This high-flow rate also induces convection on the liquid surface and forms a dimple at the plasma-liquid interface. A tungsten needle is inserted into the tube. The distance between the needle tip to the end of the tube is usually 10 mm, which may vary based on the need. It should be noted that loud noises occur with

this configuration, probably due to the boundary instabilities between the He flow and the atmosphere.

In Chapter 5, we used the gas flow tube illustrated in Figure 2.1 without the installation of a glass frit (second setup). The T-shaped tube is connected to the gas flow in one direction, while the tungsten needle is inserted perpendicularly. Usually, a modest He flow rate will be used in this case as the gas flow is connected to another equipment. This setup is also used to drive chemical synthesis and is designed to be airtight to prevent leakage. For the second setup, as the needle is inserted into a cushion, the gas flow is not connected to the plasma jet box. We previously purged He with propylene gas into the reactor using the first setup. The leaking of propylene gas probably led to a failure in the plasma jet box and formed carbon residue, illustrated in Figure 2.3. Although the actual causes of this failure are still not well-understood, the first setup is only recommended with pure inert gas flow or probably inert gas with vapor flow. For other gases or systems with volatile molecules, using the second setup should avoid the gas leakage to the plasma jet box and prevent possible failure.



Figure 2.3 Photo of the plasma jet box after the failure. Carbon residue can be seen next to the metal screws.

In Figure 2.4, the plasma jet circuit from the literature is plotted, which is similar to the one we use.[3] The photo of the one we use is demonstrated in Figure 2.3. A Rogowski coil and a high voltage probe (D-dot) are connected to an oscilloscope to measure the current and voltage profiles. In the plasma electronic circuit, a 500 Ω resistor is connected in series to the tungsten needle. The outside box of the plasma jet is made out of aluminum and connected to the grounding for safety concerns. It should be noted that the screws inside the plasma jet should be made from plastic instead of metal. As mentioned previously, a short-circuit occurred between the metal screws in the plasma jet, likely when propylene gas leaked into the jet box. The low breakdown voltage of the leaked gas likely contributed to a short circuit between the metal screws and the grounded jet box, causing the failure. The tungsten needles are from Miller, 2% lanthanated tungsten. The needle tips are sharpened to a 40-degree angle. The total length of the

needle depends on the application and the length of the tubes, which the gas is purged. It should also be noted that the leaking of flammable gases to the jet is dangerous and should be avoided.

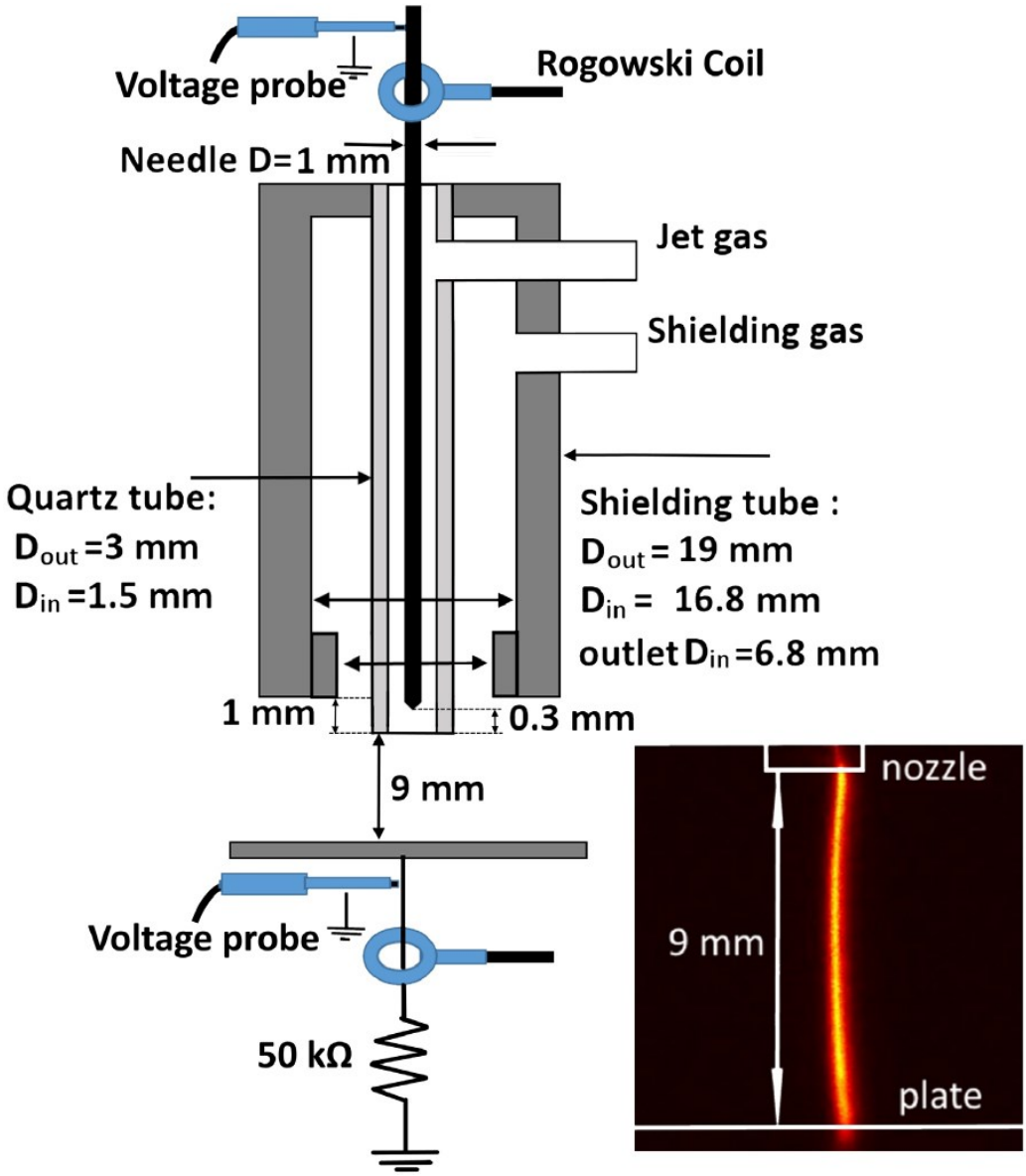


Figure 2.4 Schematic of the plasma jet configuration (left) including an image of the plasma jet in operation (in false colors; right). Adapted from [3].

2.3 Plasma Current Profiles and Circuits

In this dissertation, we utilize a pulsed DC plasma with a fixed anode or cathode configuration. The power supply is connected to a pulser and a function generator. The frequency is often 1 kHz with pulse widths on the order of μs; namely, the plasma is on for several μs in a pulse, repeating 1000 times per second. During each pulse, we typically hold the applied voltage constant and measure the resulting current profiles. The shape of the current profiles strongly depends on the conductivity of the solution, which has also been reported in the literature.[4]

In Chapters 3 and 5, high concentrations of supporting electrolyte are added to reduce Joule heating and the voltage drop across the electrolyte, whereas in Chapter 4 the supporting electrolyte is not added due to possible coalescence. From the current profiles, for a similar total current input and pulse width, the current distribution differs: in high conductivity solutions, the peak current appears after a long delay, while in low conductivity solutions, no clear delay is observed. This likely reflects the limits of the current values we can apply. For a high conductivity solution, the current rises rapidly after a certain time due to the decrease of the gas-phase resistivity; for a low conductivity solution, even if the gas-phase resistivity decreases, the remaining high resistivity of the electrolyte limits the current increase. Therefore, for a high conductivity solution with a fixed total charge input, the required applied voltage is much lower, and the current concentrates near the end of the pulse. We further assume that if the applied voltages are the same for both cases, the delay may not appear for the high conductivity solution; however, the resulting power output might exceed the capability of our equipment.

Another factor that may influence the current profile shape is the measurement method. In our setup, current profiles are recorded with a Rogowski coil and an oscilloscope. The

detection of low currents might be limited by instrumental sensitivity and the signal-to-noise ratio, particularly when the system is attenuated for high currents. Under such conditions, low-current regions may fall below the effective detection threshold, which can distort the apparent profiles and contribute to the differences observed across pulse widths. The Rogowski coil and the oscilloscope are further discussed in this chapter.

2.4 Negative and Positive Polarities Power Supply

In this dissertation, the plasma jet is connected to a negative polarity power supply and a positive polarity power supply, respectively. The two high-voltage power supplies are both one-quadrant amplifiers. A high-voltage DC amplifier boosts low-voltage DC signals to high-voltage outputs, using negative feedback around a high-voltage operational amplifier. The key factors of an amplifier include its gain accuracy, bandwidth and slew rate (how quickly the output can change), noise and offset, stability, and protections. The bandwidth and slew rate matter more for the pulsed DC setting in our experiments, which contribute to the accuracy of the pulse width and prevent a possible overshoot. The maximum output power is 10 W for our equipment. The power supply is then connected to a pulser, which outputs the high-voltage pulses to the plasma jet. In Figure 2.5, the setting of the high-voltage supply is illustrated. The positive power supply is on top, and the negative power supply is on the bottom. By switching between the two power supplies and coupling them to a pulser, we can then switch the polarities of the plasma. It should also be noted that a safety switch is installed to shut off the power supply instantly in an emergency, which is also illustrated in the photo.

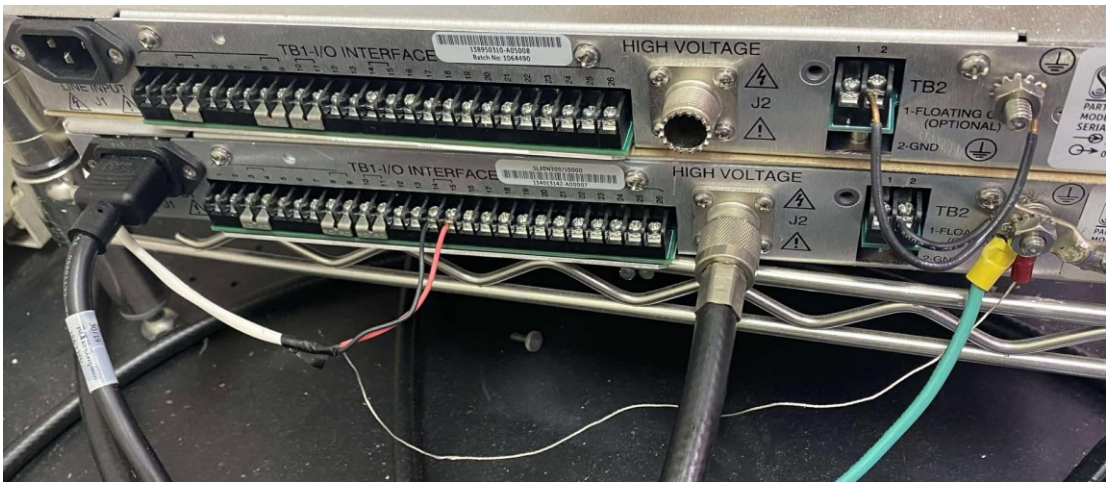


Figure 2.5 Connections of the power supply. The port in the far left is connected to the socket. The black line is connected to the interface 14, while the red line is connected to the interface 15. The high-voltage cable is connected to the pulser, and the building earth ground is connected to the grounding port (yellow/green line). A switch is also installed, connected to the red line, for an instant shutoff of the high-voltage supply.

2.5 Pulser and Waveform Generator

In the experimental setup, a waveform generator and a power supply are connected to a pulser. In Figure 2.6, the setup of this pulser is illustrated. When a negative polarity plasma (plasma-cathode) is used, the negative polarity power supply is connected to the -VDC in the setup. The +VDC is connected to a shortcut. When a positive polarity plasma (plasma-anode) is used, the positive polarity power supply is then connected to the +VDC in the setup. The -VDC is then connected to a shortcut instead. The high-voltage output is connected to the plasma jet, which ignites plasma with a tungsten needle. The pulser is air-cooled with rapid pulse rise and fall times. It should also be noted that the maximum pulse output voltage is usually limited to a certain number. For example, our pulser is limited to a 10 kV differential between the highest and lowest voltages in a pulse.



Figure 2.6 The panel in the rear of a pulser. The VDCs stand for the input from a high-voltage power supply. The pulser is air-cooled with fans. In the right section, the top cable is the pulser output, connected to the plasma jet. The bottom cable is connected to the socket. The front panel provides the connection to the waveform generator, with a switch to enable the output.

The pulser is also connected to a waveform generator, which provides the gate signal for the high-voltage output pulses. For a pulsed-DC setup, the frequency and the pulse width are selected and entered into the waveform generator. The maximum pulse width is the reciprocal of the frequency (e.g., at 1 kHz, the maximum pulse width is 1000 μs). When negative polarity plasma is used, the input pulse width value is the maximum pulse width minus the desired pulse width (e.g., at 1 kHz, enter 980 μs for a desired 20 μs pulse width). During the initial trial-and-error period, the He plasma with a pulse width of 980 μs was accidentally ignited with an ethylene glycol solution. The plasma filament was not stable, and the current was extremely high, which should be avoided. When positive polarity plasma is used, the input pulse width value is directly the desired pulse width (e.g., at 1 kHz, enter 20 μs for a desired 20 μs pulse width). It should be noted that there is also a minimum pulse width, which differs among waveform generators. The common settings of a 20 μs pulse with 1 kHz are illustrated in Figure

2.7 for a negative polarity plasma and Figure 2.8 for a positive polarity plasma. A pulsed mode is used with a delay of 0 ns, high 2.5 V, low -2.5 V, leading 18 ns, and trailing 18 ns. These settings apply to both polarities. The save and recall functions are often used to retrieve and keep the pulse settings.

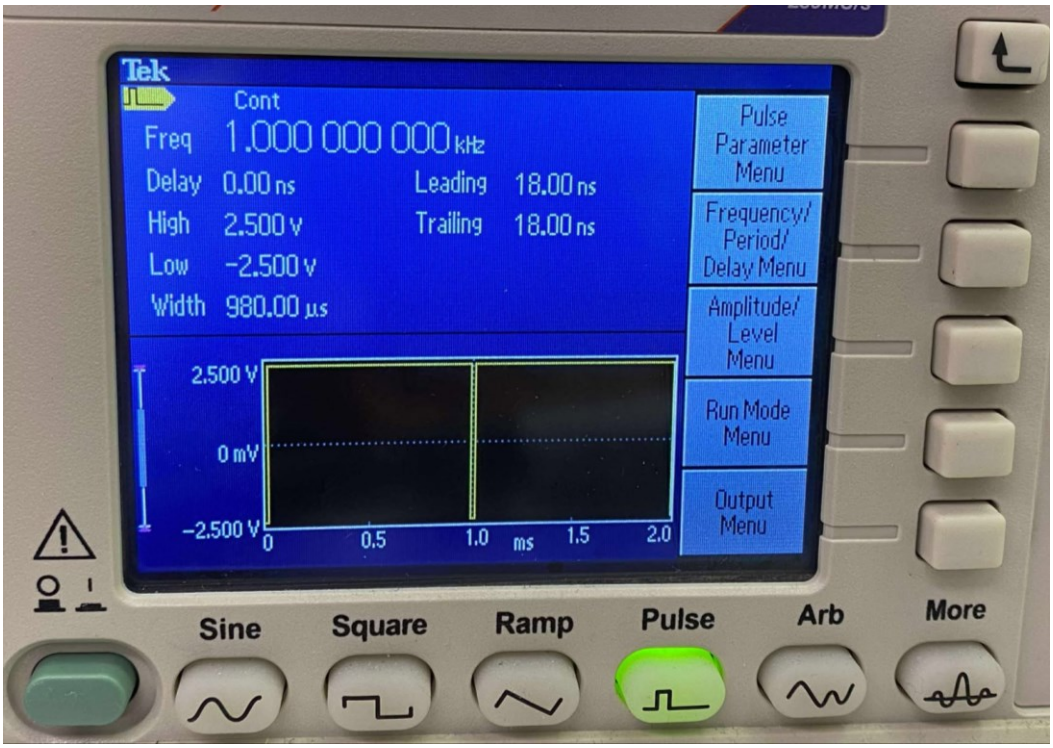


Figure 2.7 The waveform generator setting panel for a 20 µs pulse with a negative polarity plasma. The pulse width input is 980 µs instead. The waveform is plotted in the figure.

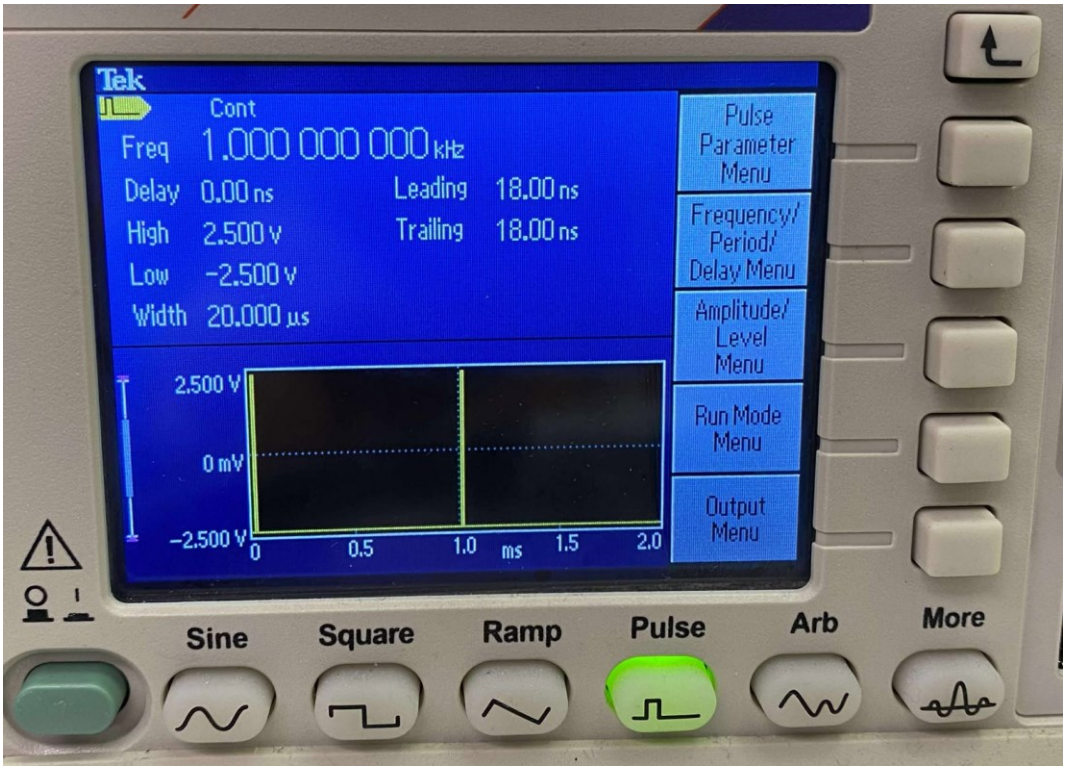


Figure 2.8 The waveform generator setting panel for a 20 µs pulse with a positive polarity plasma. The pulse width input is 20 µs. The waveform is plotted in the figure.

2.6 Oscilloscope

An oscilloscope displays and records signals, such as voltage, as a waveform. For the detection of the voltage input, the magnitude of the pulse is displayed on the vertical axis and time on the horizontal axis, using a high-voltage probe. We also use it to record the induced current profiles measured with a Rogowski coil. In our measurements, the displayed magnitude depends on the attenuation setting. With high attenuation, low-amplitude signals become insensitive. Conversely, with low attenuation, high-amplitude signals may exceed the upper limit and appear saturated. Horizontal magnification is also used to locate the pulse and must be set appropriately to display the pulse. The measured signals must be calibrated to reflect their actual

values. For example, in our setup, the measured voltages from the D-dot detector are calibrated against the readings of the high-voltage supply, and the two show a linear relationship.

Standard pulse measurements include rise time and pulse width. Rise time is the time interval required to ramp up the signal, usually voltage, from low to high. It is usually measured between 10% and 90% of the full amplitude of a pulse. Pulse width is defined to be the duration time that it remains in its high state. It can be defined at the 50% amplitude level by convention. In our case, the voltage profile from an oscilloscope is measured sometimes with an IR drop due to the sudden current increase, especially for long pulses and high conductivity solutions. The induced current profiles are recorded with a reduced form, which keeps the shape and the magnitude of the current profile in a pulse. The recorded current pulses are integrated versus time to calculate the total charge input in a pulse and therefore the current.

2.7 Rogowski coil

A Rogowski coil is an electrical device for measuring alternating current (AC) or short current pulses. It is often looped around a conductor to measure current as a non-intrusive, toroidal current sensor. When the current of the conductor changes, the resulting time-varying magnetic field induces a voltage in the coil winding that is proportional to the current-to-time derivative. This signal is then passed through an integrator to recover a waveform proportional to the instantaneous current. Because of its low inductance, a Rogowski coil can capture rapid current changes with response times down to several nanoseconds.[5] Compared with conventional current transformers, Rogowski coils exhibit excellent linearity (no saturating core), pose no risk of opening of the second winding, and are relatively cheap to construct. However, they cannot measure steady DC because they respond only to changes in current. Here, we use a Rogowski

coil to measure μs-scale current profiles of high-voltage DC pulses that ignite plasma between the liquid surface and the tip of a tungsten needle.

2.8 Plasma Ignitions

During the ignition of plasma, we first set up the pulser and the waveform generators. The setups are mentioned previously. Later, we turn on the safety switch connected to the power supply. Then, the power supply is enabled and turned on. We then choose to use current or voltage as the limiting parameter. The parameter not chosen as the limiting factor is set to a high but reasonable value. Here, the voltage and current outputs are both limited by the current setting, which is still zero. We then gradually increase the limiting factor to reach the desired output. For example, if we intend to control the current at 2 mA, we first increase the voltage knob to 4 kV, which complies with the maximum power output of the power supply. As we gradually increase the current knob, a sign of current pops up at the power supply panel, indicating that the current is the limiting factor. During the current increase, the output voltage also rises to achieve the desired current until it reaches the preset limit. If the voltage reaches 4 kV before the current reaches the intended 2 mA, the operation becomes voltage-limited. In that case, increasing the current knob no longer increases the output, because the voltage is capped at 4 kV. To further increase the current and the power output, the voltage knob also has to be increased. This setting protects the power supply from reaching its maximum power output.

In our experiments, we typically set the voltage knob to about 5 kV and use the current knob as the limiting parameter. As we focus mainly on charge transfer reactions in this dissertation, the applied current is more straightforward to compare and control. For the non-Faradaic processes discussed in Section 2.1, based on previous experience, current is also an input parameter more related to the production rate of H_2O_2 than voltage. It should be noted that

the choice of limiting factor here does not affect the pulse settings and the output waveform. Both modes produce high voltage pulses. When the current is the limiting factor, the output voltage rises only as high as needed to sustain the set current. When voltage is the limiting factor, the output voltage is fixed at the desired value and the resulting current is determined by the ignition conditions and other reactor settings. A voltage decrease is sometimes observed when the plasma is ignited while utilizing current as the limiting factor.

2.9 Chemical Scavengers

Chemical scavengers are commonly used in plasma-driven solution electrolysis (PDSE) and radiolysis as substances that preferentially react with a target species and remove it from the system. Most chemical scavengers were initially developed for radiolysis, which also involves short-lived high-energy species. The addition of a chemical scavenger sheds light on the reaction mechanism, characterizes the flux or generation of species, simplifies rate expressions, and removes undesired reactants. Common scavengers are listed in the NIST Solution Kinetics Database and in the literature.[6-7] Still, scavenging might sometimes result in different consequences and complicate the system. In PDSE, due to the complexity and the existence of several phases, the interpretation and the use of scavengers should be cross-examined and verified. For example, alcohols are often used as •OH scavengers that suppress H_2O_2 formation. Still, in one of our case study with a plasma-anode configuration, the addition of methanol actually increased the production of H_2O_2, likely due to methanol evaporation. As methanol transferred into and reacted within the plasma phase, it may have been a more effective source of •OH production, increasing overall H_2O_2 production. In this dissertation, we mainly used salts to quench high-energy species. In Table 2.2, we listed the common reactions in the liquid phase discussed in the literature. The table provides a comparison of rate constants between common

reactions and scavenging reactions. Specifically, reactions 2.45 and 2.46 are used in Chapter 3 as scavengers, and reactions 2.43 and 2.46 are used in Chapter 5. We also highlight reactions 2.1 and 2.22 as common pathways for the high-energy species. Here, the reactions 2.47 and 2.48 are photolysis reactions as Φ stands for the reaction quantum yield. The rate constant of reaction 2.9 explicitly includes the water concentration; therefore, its units are M^{-1} s^{-1}.

Table 2.2 The common reactions and their rate constants in the liquid phase. Most of the rate constants are from radiolysis.

Index	Reaction	Rate constant	Reference
2.1	$2e_{aq}^- + 2H_2O \rightarrow H_2 + 2\ OH^-$	$1 \times 10^8\ M^{-3}\ s^{-1}$	7-8
2.2	$e_{aq}^- + H_2O \rightarrow \bullet H + OH^-$	$1.9 \times 10^1\ M^{-1}\ s^{-1}$	7
2.3	$e_{aq}^- + H_2O^+ \rightarrow \bullet H + \bullet OH$	$6 \times 10^{11}\ M^{-1}\ s^{-1}$	7
2.4	$e_{aq}^- + \bullet H + H_2O \rightarrow H_2 + OH^-$	$2.5 \times 10^{10}\ M^{-2}\ s^{-1}$	7
2.5	$e_{aq}^- + \bullet OH \rightarrow OH^-$	$3 \times 10^{10}\ M^{-1}\ s^{-1}$	7
2.6	$e_{aq}^- + O^- + H_2O \rightarrow 2OH^-$	$2.2 \times 10^{10}\ M^{-2}\ s^{-1}$	7
2.7	$e_{aq}^- + H_3O^+ \rightarrow \bullet H + H_2O$	$2.3 \times 10^{10}\ M^{-1}\ s^{-1}$	7
2.8	$e_{aq}^- + H_2O_2 \rightarrow \bullet OH + OH^-$	$1 \times 10^8\ M^{-1}\ s^{-1}$	7
2.9	$e_{aq}^- + HO_2^- + H_2O \rightarrow \bullet OH + 2OH^-$	$1.9 \times 10^1\ M^{-1}\ s^{-1}$	7
2.10	$e_{aq}^- + O_2 \rightarrow O_2^-$	$6 \times 10^{11}\ M^{-1}\ s^{-1}$	7
2.11	$e_{aq}^- + \bullet O \rightarrow O^-$	$2.5 \times 10^{10}\ M^{-1}\ s^{-1}$	7-8
2.12	$\bullet H + H_2O \rightarrow H_2 + \bullet OH$	$1 \times 10^1\ M^{-1}\ s^{-1}$	7
2.13	$\bullet H + \bullet H \rightarrow H_2$	$7.5 \times 10^9\ M^{-1}\ s^{-1}$	7
2.14	$\bullet H + \bullet OH \rightarrow H_2O$	$7 \times 10^9\ M^{-1}\ s^{-1}$	7
2.15	$\bullet H + OH^- \rightarrow H_2O + e_{aq}^-$	$2.2 \times 10^7\ M^{-1}\ s^{-1}$	7
2.16	$\bullet H + H_2O_2 \rightarrow H_2O + \bullet OH$	$9 \times 10^7\ M^{-1}\ s^{-1}$	7
2.17	$H_2 + H_2O_2 \rightarrow H_2O + \bullet OH + \bullet H$	$6 \times 10^6\ M^{-1}\ s^{-1}$	7-8
2.18	$\bullet H + O_2 \rightarrow HO_2$	$2.1 \times 10^{10}\ M^{-1}\ s^{-1}$	7
2.19	$\bullet H + HO_2 \rightarrow H_2O_2$	$1 \times 10^{10}\ M^{-1}\ s^{-1}$	7
2.20	$\bullet O + H_2O \rightarrow \bullet OH + \bullet OH$	$1.3 \times 10^4\ M^{-1}\ s^{-1}$	7-8

2.21	$\bullet O + O_2 \rightarrow O_3$	3×10^9 M^{-1} s^{-1}	7-8
2.22	$\bullet OH + \bullet OH \rightarrow H_2O_2$	5.5×10^9 M^{-1} s^{-1}	7
2.23	$\bullet OH + O^- \rightarrow HO_2^-$	2×10^{11} M^{-1} s^{-1}	7
2.24	$\bullet OH + H_2 \rightarrow \bullet H + H_2O$	4.2×10^7 M^{-1} s^{-1}	7
2.25	$\bullet OH + OH^- \rightarrow O^- + H_2O$	1.3×10^{10} M^{-1} s^{-1}	7
2.26	$\bullet OH + HO_2 \rightarrow O_2 + H_2O$	6×10^9 M^{-1} s^{-1}	7
2.27	$\bullet OH + O_2^- \rightarrow O_2 + OH^-$	8×10^9 M^{-1} s^{-1}	7
2.28	$O^- + H_2O \rightarrow OH^- + \bullet OH$	1.8×10^6 M^{-1} s^{-1}	7
2.29	$O^- + H_2 \rightarrow OH^- + \bullet H$	8×10^7 M^{-1} s^{-1}	7
2.30	$O^- + H_2O_2 \rightarrow O_2^- + H_2O$	5×10^9 M^{-1} s^{-1}	7
2.31	$O^- + HO_2^- \rightarrow O_2^- + OH^-$	4×10^8 M^{-1} s^{-1}	7
2.32	$O^- + O_2 \rightarrow O_3^-$	3.6×10^9 M^{-1} s^{-1}	7
2.33	$\bullet OH + H_2O_2 \rightarrow H_2O + HO_2$	2.7×10^7 M^{-1} s^{-1}	7
2.34	$\bullet OH + HO_2^- \rightarrow OH^- + HO_2$	7.5×10^9 M^{-1} s^{-1}	7
2.35	$H_2O^+ + H_2O \rightarrow H_3O^+ + \bullet OH$	6×10^3 M^{-1} s^{-1}	7
2.36	$H_3O^+ + OH^- \rightarrow H_2O + \bullet H + \bullet OH$	6×10^{10} M^{-1} s^{-1}	8
2.37	$HO_2 + H_2O \rightarrow H_3O^+ + O_2^-$	2×10^3 M^{-1} s^{-1}	8
2.38	$H_3O^+ + O_2^- \rightarrow H_2O + HO_2$	6×10^1 M^{-1} s^{-1}	9
2.39	$H_2O \rightleftharpoons H^+ + OH^-$	$k_f = 1.4 \times 10^{-2}$ M^{-1} s^{-1} $k_b = 1.4 \times 10^{11}$ M^{-1} s^{-1}	10
2.40	$H_2O_2 + OH^- \rightleftharpoons HO_2^- + H_2O$	$k_f = 1.0 \times 10^{10}$ M^{-1} s^{-1} $k_b = 1.0 \times 10^6$ M^{-1} s^{-1}	6, 11
2.41	$[Fe(CN)_6]^{3-} + e_{aq}^- \rightarrow [Fe(CN)_6]^{4-}$	1.2×10^{10} M^{-1} s^{-1}	6
2.42	$[Fe(CN)_6]^{3-} + \bullet H \rightarrow [Fe(CN)_6]^{4-} + H^+$	6.3×10^9 M^{-1} s^{-1}	6
2.43	$[Fe(CN)_6]^{4-} + \bullet OH \rightarrow [Fe(CN)_6]^{3-} + OH^-$	1.1×10^{10} M^{-1} s^{-1}	6
2.44	$[Fe(CN)_6]^{4-} + H_2O_2 \rightarrow [Fe(CN)_6]^{3-}$	Relatively slow	12
2.45	$NO_3^- + e_{aq}^- \rightarrow NO_3^{2-}$	9.7×10^9 M^{-1} s^{-1}	13
2.46	$Cl^- + \bullet OH \rightarrow ClOH^-$	4.3×10^9 M^{-1} s^{-1}	14
2.47	$H_2O + h\nu \rightarrow \bullet OH + \bullet H$	$\Phi = 0.37$	11, 15
2.48	$H_2O + h\nu \rightarrow \bullet OH + H^+ + e_{aq}^-$	$\Phi = 0.05$	11

2.10 Linear Sweep Voltammetry

Linear Sweep Voltammetry (LSV) is an electrochemical method in which the applied potential varies linearly with time (a voltage ramp) while the current is recorded as a function of potential or time. This technique is used in Chapters 3 and 4 to measure ferricyanide/ferrocyanide concentrations and onset reduction potentials. In Chapter 3, we employ it to determine the mass-transfer-limiting current of the redox couple at high overpotentials and quantify the concentrations of the reduced and oxidized forms. With the probe positioned near the plasma-liquid interface with a 3 standard liter per minute (SLPM) He flow, convection is sufficient to establish a mass-transfer-limited regime in which further increases in overpotentials do not increase the measured current. In this regime, the mass-transfer-limited current is approximately linearly correlated to the species concentration in the electrolyte, providing concentration information beyond the open-circuit potential (OCP), which reports only the concentration ratio of the redox couple. This approach also enables more reliable *in situ* electrochemical measurements of PDSE, as the current values are not affected significantly by the induced IR drop. In Figure 2.9, an example of common LSV profiles is provided. In Figure 2.9a, the applied voltage versus time is plotted, which clearly shows a linear behavior between the upper and lower limits. In Figure 2.9b, the applied voltage versus the induced current profile is plotted. The two regions with high overpotentials show mass-transfer limitations.

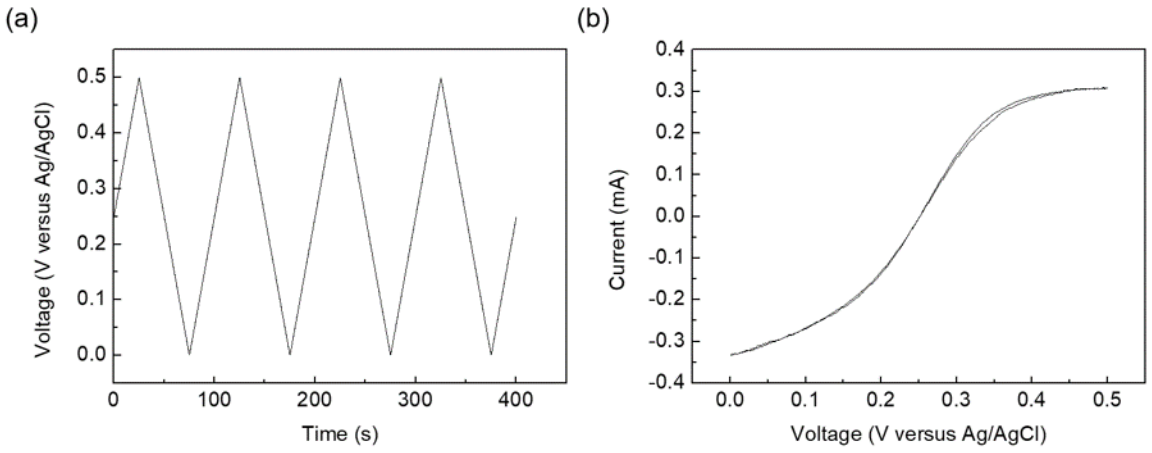


Figure 2.9 An example of common LSV profiles. (a) Applied voltages versus time between 0.5 V to 0 V versus an Ag/AgCl reference electrode. (b) Corresponding current profiles versus voltage with the addition of 5 mM ferricyanide and 5 mM ferrocyanide. The working electrode was a Pt disk with a rotating speed of 1000 rpm.

In Chapter 4, we used LSV to detect the onset reduction potentials of metal precursors. This reaction involves the reduction of metal ions on the electrode surface. When a potential higher than the onset reduction potential is applied to a metal electrode, the metal ions adsorb to the electrode surface and get reduced to metal atoms. Here, we assume that the measured onset reduction potential is related to the reduction potential of a metal precursor in the solvent. A similar method was used previously to detect the onset reduction potentials of metal precursors.[16-17] Since the reduction potentials are only related to thermodynamics, the surface kinetics and elementary steps on the electrode surface might require extra overpotentials to drive the reaction.[18] We also used a rotating disk electrode setup to mitigate mass-transfer limitations. The onset potentials are defined to be the starting potential of the exponential growth of current values. Based on Equation 1.3, the current increases exponentially versus the overpotential. The current versus applied potential is governed by electrode kinetics (Equation 1.3), mass-transfer limitations, and a decrease of electrode surface area as the reduced metal atoms covering the electrode surface. The existence of the reduced metal atoms on the electrode as the reduced form

of the metal ion/atom redox couple should also be noted, which probably makes the measured onset reduction potential values closer to its actual reduction potentials. This method can be more vigorously used to decide the reduction potentials in non-aqueous solutions.

2.11 Open Circuit Potential

The OCP is the potential difference measured between a working electrode and a reference electrode when the working electrode measures zero net current. For a fast redox couple on a well-defined electrode, the OCP is equivalent to the reduction potential of a redox couple and can be calculated from the Nernst equation.[18] From Equation 1.3, when the net current is zero, the Nernst equation can also be derived, corresponding to the concentration ratio of the redox couple. It should be noted that a net-zero current can be interpreted as no net conversion of the redox couple. That is, the electron energy level of the redox couple is in equilibrium with the electron energy level of the electrode in conventional electrochemistry. In Chapter 3, OCP is used as a technique to measure the redox couple concentration ratios, which shift after plasma-liquid interactions. We use a gold wire covered with hot-melt adhesive with only 1 mm exposure to the solution. The gold wire is adjusted to a L-shape to better fit the reactor design and to decrease the possible exposure directly to the plasma. If the gold wire directly interacts with plasma, there might be a current flow from or to the gold wire, which damages the connected potentiostat. Due to the liquid dimple from the strong He flow, the electrochemical probe should not be too close to the interface, as the dimple size may slightly vary across the plasma-liquid interaction time.

We observed that OCP measurements were influenced by plasma ignition even without a redox couple ratio change, likely due to ionic currents (IR drop) across the electrolyte. When we used a reference electrode as the working electrode and measured the OCP, the OCP shifted

during the plasma ignition. This phenomenon is better understood with a conventional electrochemical system. We measured the OCP shifts between two reference electrodes while applying an LSV with a Pt electrode in the electrolyte. As one reference electrode was set close to the Pt electrode and the other one far away, an OCP shift can be observed, even though the reference electrodes should be relatively inert to the local chemical change. The data in Figure 2.10 demonstrate the relationship between the measured current on the Pt electrode (x-axis, working 1) and the OCP shifts between two reference electrodes (y-axis, working 2).

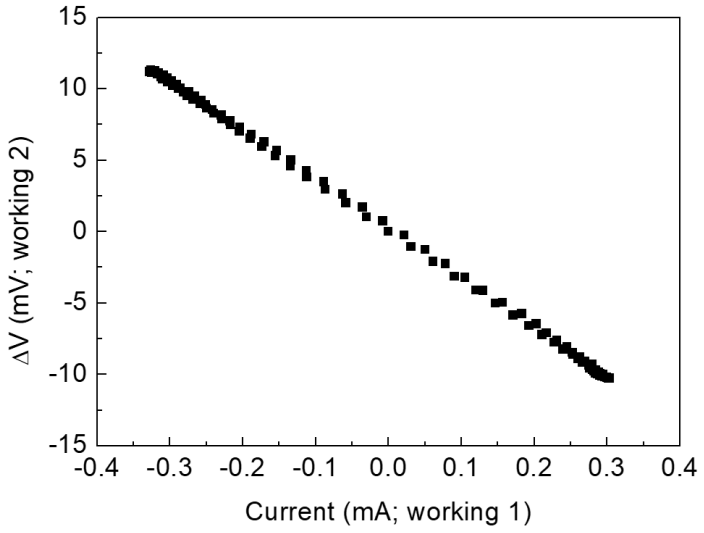


Figure 2.10 The measured OCP shifts against the measured current values on a Pt electrode. We used a potentiostat to measure the current values on a Pt electrode, denoted as working 1, with 5 mM of ferricyanide and 5 mM of ferrocyanide. 100 mM of potassium sulfate was added as the supporting electrolyte. The OCP shifts between two reference electrodes at different positions were measured with another potentiostat. The reference electrode placed 10 mm away from the Pt electrode is denoted as working 2, while another reference electrode is placed far away from the Pt electrode.

From Figure 2.10, it is demonstrated that the OCP shifts from two reference electrodes at different positions are a function of the measured current from the Pt electrode. The linear relationship implies that the measured OCP shifts might result from the IR drop in the

electrolyte, which should also affect the OCP measurements when we use a gold wire as the working electrode in Chapter 3 if the measurements are done *in situ*. This also confirms that an OCP shift does not necessarily suggest a redox couple ratio change if the OCPs are measured in the presence of an external current. Thus, *in situ* OCP measurements in PDSE require careful calibration of plasma-induced electric potential shifts, as not all changes in OCP reflect changes in the redox couple ratio due to the contribution of IR drop (electric potential). Accordingly, in Chapter 3, we performed OCP measurements before and after plasma-liquid interactions to avoid undesired contributions from other factors. It should also be noted that OCP reflects the local concentration ratio at the probe. Therefore, there might be a spatial distribution of OCP across the reactor in Chapter 3. This spatial distribution resolution might be limited by the size of the probe.

2.12 Material Characterization Techniques

In Chapter 4, we use X-ray photoelectron spectroscopy (XPS), scanning transmission electron microscopy (STEM), X-ray diffraction (XRD), energy dispersive X-ray spectroscopy (EDS), and Ultraviolet-visible (UV-vis) spectrum to characterize the alloy nanoparticles. XPS is a surface analysis technique for elemental and chemical composition. The penetration depth depends on the sample and the source.[19] STEM is used to decide the morphology, size distribution, and d-spacing of nanoparticles. We also use the signal intensities to decide the d-spacing differences between monometallic Pt nanoparticles and Pt-silver (Ag) alloy nanoparticles (Pt 80% and Ag 20%), illustrated in Figure 2.11.[20] EDS is often measured with STEM to quantify the elements in a sample. With a line scan, it can also reveal the distribution of elements in a single structure. For example, it distinguishes core-shell structures from alloy structures as the latter has uniform elemental distribution over a nanoparticle. XRD is used to

determine the crystalline structure of a sample. In Chapter 4, when Pt is mixed with Ag, the size of the d-spacing changes, and therefore the measured diffraction peak shifts. UV-vis spectrum is used due to the plasmonic nature of Ag nanoparticles.[21-22]

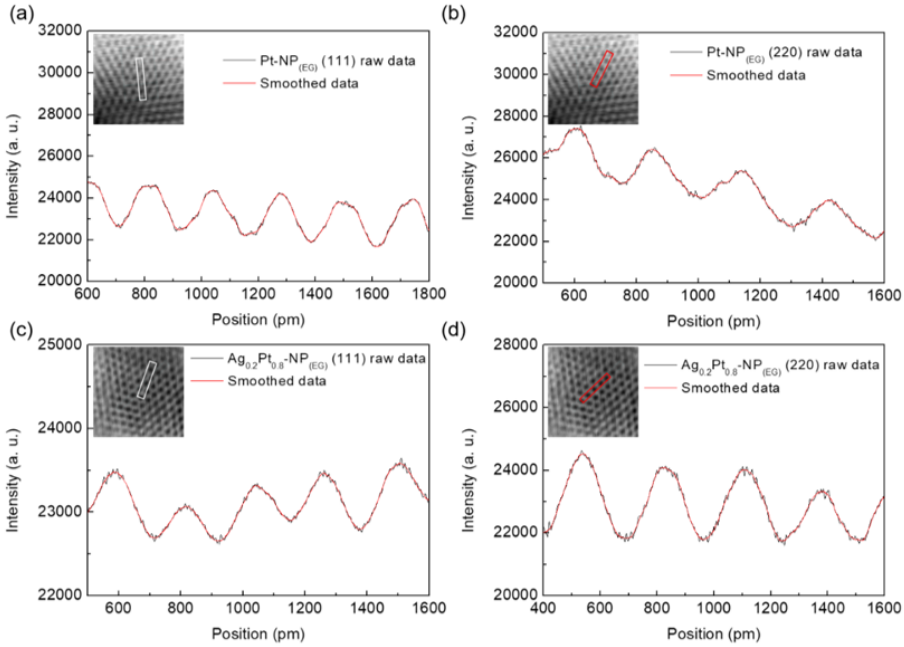


Figure 2.11 Bright-field STEM intensity line profiles of (a) Pt-NP$_{(EG)}$ (111) facet, (b) Pt-NP$_{(EG)}$ (220) facet, (c) $Ag_{0.2}Pt_{0.8}$-NP$_{(EG)}$ (111) facet, and (d) $Ag_{0.2}Pt_{0.8}$-NP$_{(EG)}$ (220) facet. These line profiles were smoothed using the Savitzky–Golay algorithm[23] with a polynomial degree of 2.

2.13 Gas Chromatography-Mass Spectrometry

Gas chromatography-mass spectrometry (GC-MS) is an analytical technique for identifying and quantifying compounds in liquid and gaseous samples that can be volatilized. In a gas chromatograph (GC), the sample is vaporized in the inlet and its components are separated either on a capillary column coated with a stationary phase or on a packed column with solid support materials. An inert carrier gas (typically He) is also injected to dilute the analytes and to propel them through the column. Each species exhibits a characteristic retention time, which is

governed by the column, the boiling point and polarity of the compound, and the oven temperature program of the GC. For example, in Chapter 5, we separated isopropyl alcohol and acetone in the feeding gas and assigned them to two characteristic peaks. The integrated peak area is usually linearly related to the concentration of that compound. A calibration line from standards with known concentrations is typically established and utilized.

GC columns play a crucial role in the separation and analysis of species. The column should be selected to fit the injected species, with appropriate selectivity and resolution toward the products. Some key parameters include the column length, internal diameter, and film thickness of the stationary phase. Some columns are suitable for and resistant to solvent injections (such as water), while most are not. Meanwhile, the choice between polar and non-polar stationary phases and the oven temperature settings also contribute to the separation process, affecting the retention time and the resolution of their characteristic peaks. The temperature ramps help elute broad mixtures by their boiling point differences. The cleaning process is also essential to clean the columns and prevent interference from the previous run. Standard chemicals are used to establish the retention time based on a specific oven setting and a column.

When the GC is coupled to a mass spectrometry (MS), the eluted compounds are then transferred to the MS, where they are ionized and fragmented, then sorted by a mass analyzer. By the fragment intensity ratios and the mass-to-charge (m/z) ratios, GC peaks can be matched against spectral libraries for confident identification and assigned a relative possibility. This enables simultaneous identification and quantification of unknown compounds. In an MS, the m/z ratios are measured with a quadrupole with four parallel rods. Ions with a specific m/z ratio

have a stable path through the oscillating electric field and reach the detector. By the setting, a range of m/z values can be scanned through to produce the spectrum.

In Chapter 5, GC-MS is used to determine the concentrations of acetone and isopropyl alcohol. The inlet of the GC-MS was held at 150 °C. The oven was held at 35 °C for 2 minutes and then heated to 180 °C with a temperature ramp of 15 °C min^{-1}. A solvent delay for 4 minutes was used to avoid damage to the filament. The MS source was held at 230 °C, and the MS quadrupole was held at 150 °C. A high-temperature post-run was used afterward to clean the remaining compounds.

2.14 References

1. Lee, D.; Chen, H.-T.; Linic, S., Plasma-Induced Selective Propylene Epoxidation Using Water as the Oxygen Source. *JACS Au* **2023,** *3* (4), 997-1003.

2. Yue, Y.; Exarhos, S.; Nam, J.; Lee, D.; Linic, S.; Bruggeman, P. J., Quantification of Plasma Produced OH and Electron Fluxes at the Liquid Anode and Their Role in Plasma Driven Solution Electrochemistry. *Plasma Sources Science and Technology* **2022,** *31* (12), 125008.

3. Yatom, S.; Luo, Y.; Xiong, Q.; Bruggeman, P. J., Nanosecond Pulsed Humid Ar Plasma Jet in Air: Shielding, Discharge Characteristics and Atomic Hydrogen Production. *Journal of Physics D: Applied Physics* **2017,** *50* (41), 415204.

4. Rumbach, P.; Clarke, J. P.; Go, D. B., Electrostatic Debye Layer Formed at a Plasma-Liquid Interface. *Physical Review E* **2017,** *95* (5), 053203.

5. Tumanski, S., *Handbook of Magnetic Measurements*. 1 ed.; CRC Press: 2011.

6. Buxton, G. V.; Greenstock, C. L.; Helman, W. P.; Ross, A. B., Critical Review of Rate Constants for Reactions of Hydrated Electrons, Hydrogen Atoms and Hydroxyl Radicals

(·OH/·O⁻ in Aqueous Solution. *Journal of Physical and Chemical Reference Data* **1988,** *17* (2), 513-886.

7. Madden, K. P.; Mezyk, S. P., Critical Review of Aqueous Solution Reaction Rate Constants for Hydrogen Atoms. *Journal of Physical and Chemical Reference Data* **2011,** *40* (2), 023103.

8. Tian, W.; Kushner, M. J., Atmospheric Pressure Dielectric Barrier Discharges Interacting with Liquid Covered Tissue. *Journal of Physics D: Applied Physics* **2014,** *47* (16), 165201.

9. Pandis, S. N.; Seinfeld, J. H., Sensitivity Analysis of a Chemical Mechanism for Aqueous-Phase Atmospheric Chemistry. *Journal of Geophysical Research: Atmospheres* **1989,** *94* (D1), 1105-1126.

10. Gopalakrishnan, R.; Kawamura, E.; Lichtenberg, A. J.; Lieberman, M. A.; Graves, D. B., Solvated Electrons at the Atmospheric Pressure Plasma–Water Anodic Interface. *Journal of Physics D: Applied Physics* **2016,** *49* (29), 295205.

11. Zvereva, G. N., Investigation of Water Decomposition by Vacuum Ultraviolet Radiation. *Optics and Spectroscopy* **2010,** *108* (6), 915-922.

12. Rabani, J.; Stein, G., The Reactivity of OH Radicals with Ferro-Ferricyanide, Formate, Ethanol and Amino Acids in Irradiated Solutions. *Transactions of the Faraday Society* **1962,** *58* (0), 2150-2159.

13. Elliot, A. J.; McCracken, D. R.; Buxton, G. V.; Wood, N. D., Estimation of Rate Constants for near-Diffusion-Controlled Reactions in Water at High Temperatures. *Journal of the Chemical Society, Faraday Transactions* **1990,** *86* (9), 1539-1547.

14. Jayson, G. G.; Parsons, B. J.; Swallow, A. J., Some Simple, Highly Reactive, Inorganic Chlorine Derivatives in Aqueous Solution. Their Formation Using Pulses of Radiation and Their

Role in the Mechanism of the Fricke Dosimeter. *Journal of the Chemical Society, Faraday Transactions 1: Physical Chemistry in Condensed Phases* **1973,** *69* (0), 1597-1607.

15. Heit, G.; Neuner, A.; Saugy, P.-Y.; Braun, A. M., Vacuum-UV (172 nm) Actinometry. The Quantum Yield of the Photolysis of Water. *The Journal of Physical Chemistry A* **1998,** *102* (28), 5551-5561.

16. Bonet, F.; Guéry, C.; Guyomard, D.; Herrera Urbina, R.; Tekaia-Elhsissen, K.; Tarascon, J. M., Electrochemical Reduction of Noble Metal Compounds in Ethylene Glycol. *International Journal of Inorganic Materials* **1999,** *1* (1), 47-51.

17. Bonet, F.; Guéry, C.; Guyomard, D.; Herrera Urbina, R.; Tekaia-Elhsissen, K.; Tarascon, J. M., Electrochemical Reduction of Noble Metal Species in Ethylene Glycol at Platinum and Glassy Carbon Rotating Disk Electrodes. *Solid State Ionics* **1999,** *126* (3), 337-348.

18. Bard, A. J.; Faulkner, L. R., *Electrochemical Methods: Fundamentals and Applications*. Sec. ed.; John Wiley & Sons: New York, 2001.

19. Stevie, F. A.; Donley, C. L., Introduction to X-Ray Photoelectron Spectroscopy. *Journal of Vacuum Science & Technology A* **2020,** *38* (6), 063204.

20. Chen, H.-T.; Lee, D.; Linic, S., Formation of Mixed Bimetallic Nanoparticles of Immiscible Metals through Plasma-Induced Reduction of Precursors in Solutions: A Case Study of Ag–Pt Alloy Nanoparticles. *Chemistry of Materials* **2023,** *35* (16), 6557-6565.

21. Aslam, U.; Linic, S., Kinetic Trapping of Immiscible Metal Atoms into Bimetallic Nanoparticles through Plasmonic Visible Light-Mediated Reduction of a Bimetallic Oxide Precursor: Case Study of Ag–Pt Nanoparticle Synthesis. *Chemistry of Materials* **2016,** *28* (22), 8289-8295.

22. Linic, S.; Christopher, P.; Ingram, D. B., Plasmonic-Metal Nanostructures for Efficient Conversion of Solar to Chemical Energy. *Nature Materials* **2011,** *10* (12), 911-921.

23. Savitzky, A.; Golay, M. J. E., Smoothing and Differentiation of Data by Simplified Least Squares Procedures. *Analytical Chemistry* **1964,** *36* (8), 1627-1639.

Chapter 3 Bridging Plasma-Driven Solution and Conventional Electrochemistry via an Electrochemical Probe

3.1 Summary

In this work, we attempt to characterize PDSE using electrochemical methods. We developed an electrochemical probe method to characterize plasma-liquid interactions by directly linking plasma-driven solution electrolysis (PDSE) with conventional electrochemical concepts. Using a gold wire probe, we measured the open-circuit potential (OCP) at the plasma-solution interface in a ferricyanide/ferrocyanide redox system. These measurements revealed how plasma application modulates interfacial electrochemical potentials and enabled quantification of reactive species, including hydrated electrons (e_{aq}^-) and hydroxyl radicals (•OH). By correlating probe-derived potentials with local species concentrations, we identified the relative abundances of these short-lived intermediates under different plasma polarities and operating conditions. This approach provides a quantitative framework for probing plasma-liquid chemistry with electrochemical resolution.

The electrochemical probe setup was initiated by Dr. Dongho Lee to measure the ionic current in the liquid phase with a μs timescale. The current experiments and data analyses were done by Han-Ting Chen.

3.2 Introduction

Plasma-driven solution electrolysis (PDSE) has emerged as an area of increasing interest at the intersection of electrochemistry and plasma science.[1-3] In PDSE systems, low-temperature

plasma interacts with a liquid phase, which generates a highly reactive interface with plasma-induced species such as electrons,[4-5] ions,[6-8] photons,[9-10] and neutral radicals.[11-13] These high-energy species drive complex physical and chemical processes that are challenging to achieve through other conventional electrolysis or thermal-driven processes.[14-16] While PDSE is promising for expanding the capabilities of both electrochemical systems and plasma-assisted applications, its high reactivity and inherent complexity present challenges for the characterization and control, especially in the liquid phase.[17-19]

From an electrochemical perspective, the characterization of PDSE remains relatively limited and not fully understood. In conventional electrochemistry, charge transfer across the electrode-electrolyte interface is driven by the difference between the electrode potential and the solution potential at the interface.[20] The electrode potential reflects the Fermi level of electrons in the electrode, while the solution potential corresponds to the electrochemical potential of the electrons in the solution and is governed by the reduction potential of the target redox couple.[21] Oldham *et al.* previously referenced the term "overpotential" involving radio-frequency (RF) plasmas with the scanning reference electrode technique.[22] However, its analogy to conventional electrochemical systems remains unclear due to the alternating current nature of RF plasma. The scanning reference electrode technique is more suited to measuring the direction of current and the IR drop across the electrolyte.[23] Therefore, the inclusion of charge-transfer processes and a clear alignment of terminology with that used in conventional electrochemistry are still lacking, limiting direct comparisons between PDSE and conventional electrochemical systems.

3.3 Experimental Section

The sketch in Figure 3.1a shows the plasma and electrochemical setup used in our study. A pulsed direct-current (DC) plasma discharge was generated to interact with the solution, which

contains ferricyanide/ferrocyanide redox couple, with varying concentration ratios. For the electrochemical measurements, the gold wire, positioned at the plasma-liquid interface, served as an electrochemical probe that measured the solution potential through OCP measurements. The solution potential is governed by the redox couple ratio, illustrated in Figure 3.1b. A plasma that has reducing (or oxidizing) power will change this ratio by reducing (or oxidizing) the redox couple, and this will affect the solution potential measured by the gold wire. We note that the measured solution potentials correlate with the concentration of the oxidized and reduced forms of the redox couple following the Nernst equation.[20] The total concentration of ferricyanide and ferrocyanide is controlled to be 10 mM, listed in Table 3.1. The total concentration is chosen to mitigate the mass-transfer limitations, yet to make the solution potential shifts more measurable. The scale of several mM fitted better for the total current input we used. If the concentration is too high, the solution potential shifts become less significant, while the redox species might be easily exhausted if the concentration is too low.

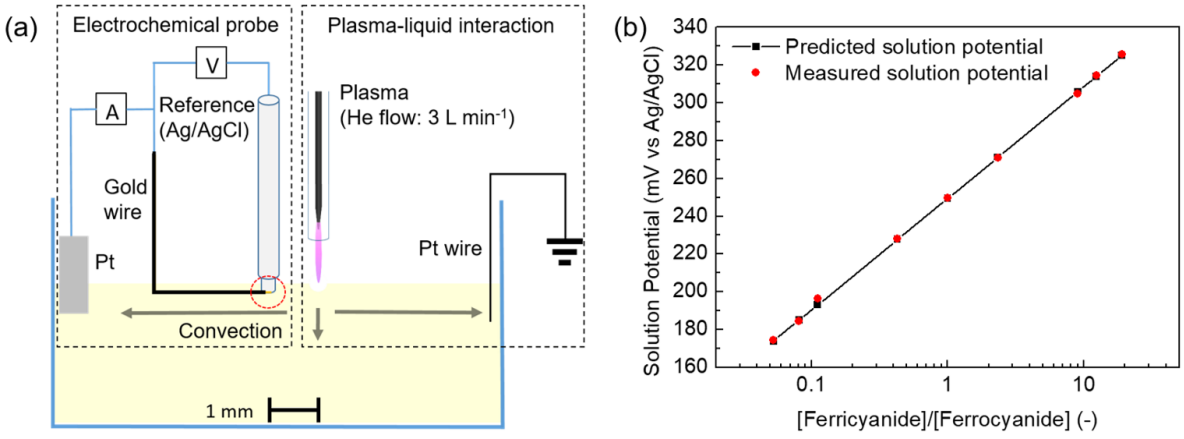


Figure 3.1 (a) Schematic of the pulsed DC plasma setup and the electrochemical probe with a three-electrode setup. (b) The measured solution potentials versus the ferricyanide-to-ferrocyanide concentration ratios.

Table 3.1 The ferricyanide and ferrocyanide concentrations in Figure 3.1b. The total concentration is controlled to be 10 mM.

Solution #	Ferricyanide concentration (mM)	Ferrocyanide concentration (mM)	Ferricyanide-to-Ferrocyanide concentration ratios (-)
1	0.5	9.5	0.053
2	0.75	9.25	0.081
3	1	9	0.11
4	3	7	0.43
5	5	5	1.0
6	7	3	2.3
7	9	1	9.0
8	9.25	0.75	12
9	9.5	0.5	19

Ferricyanide ($K_3[Fe(CN)_6]$) and ferrocyanide ($K_4[Fe(CN)_6]\bullet 3H_2O$) were dissolved in 50 ml of deionized water (18.2 MΩ·cm at 25 °C). The redox couple is specifically chosen due to its pH-independent and fast kinetics on a metal electrode.[24] The concentrations of the redox species were specified for each experimental condition. 100 mM of potassium sulfate (K_2SO_4) was also in the solution as the supporting electrolyte. Potassium nitrate (KNO_3) and potassium chloride (KCl) were added as scavengers for e_{aq}^- and •OH radicals, respectively. Solution potential measurements were conducted using a three-electrode setup comprising a gold wire working electrode (0.5 mm diameter, 99.95%), a platinum (Pt)-coated fluorine-doped tin oxide (FTO) counter electrode, and a silver-silver chloride electrode (Ag/AgCl (3M KCl), $E_{Ag/AgCl}$ = 208 mV vs NHE) reference electrode. A 1 mm segment of the gold wire was exposed to the electrolyte. Both the working and reference electrodes were positioned 1 mm away from the plasma-liquid interface (between the edge of the dimple and the tip end of the probe), oriented in the direction opposite to the grounding electrode. The reference electrode was placed next to the working electrode. The plasma-liquid interface was put in the middle of a Petri dish, with the grounding electrode on the right. It should be noted that the plasma-liquid interface formed a dimple due to the strong He flow. The depth of the gold probe had to be modified to align with the bottom of

the dimple. The counter electrode, although not required for the OCP measurement, was placed toward the solution on the left. At the working electrode, OCP was measured with a potentiostat (Gamry Reference 620) and averaged for 100 s at a sampling interval of 0.1 s before and after 30 minutes of plasma-liquid interactions. Reported values are the mean of three individual experiments.

We also used linear-sweep voltammetry, introduced in Chapter 2, to measure the absolute concentrations of the reduced and the oxidized forms. With high overpotentials and the convection by the He flow, the measured currents were mass-transfer limited and did not increase significantly with the increase in the overpotentials. Therefore, the currents in those regions were proportional to the absolute concentrations of the redox couple. This was also used to compare with the measurements from the OCP. Still, the LSV measurements likely changed the local redox couple concentrations and therefore affected the OCP measurements. As the LSV measurements involved currents, charge transfer of the redox couple occurred at the electrode surface and changed its local ratios. That is, after the LSV measurements, the OCP values might be altered and have to be measured again. The scan rate of the LSV measurements was 25 mV sec^{-1}, and the overpotentials were 300 mV from the measured OCPs.

During PDSE, the potentiostat should be switched off, or the probe should be moved away from the plasma-liquid interface. If the probe is too close to the interface with PDSE, PDSE affects the signals of the electrochemical cell due to the IR drop or due to the direct interactions between the probe and the plasma. When the *in situ* measurement is performed, which is discussed as a possible method in Chapter 2, both the IR drops and the solution potential shifts have to be taken into account for the OCP shifts. For example, we used to measure the OCP shifts in the scale of μs during PDSE. As the timescale was not sufficient for

the redox couple concentration changes to be measured at the position of the probe, the signals were believed to result only from the IR drop of a single pulse. The IR drop was not mass-transfer limited and therefore can be measured with a probe in such a short time.

We also discovered that by adjusting the relative position of the working and reference electrodes, the IR drops can be mitigated. It was used as a method to calibrate the relative position of the two electrodes and to eliminate the contributions from other factors while measuring the solution potential shifts during PDSE interactions. Still, as the redox couple ratio changes were mass-transfer limited on the μs timescale, the merits of *in situ* measurement were outweighed by the instability of the *in situ* measurements and the risk of damaging the potentiostat. As a result, all of the solution potential measurements were done before and after PDSE.

To reduce system complexity, we deliberately used the pulsed DC helium (He) plasma as a case study. Both plasma-cathode (negative polarity) and plasma-anode (positive polarity) configurations were investigated to represent the cathodic and anodic conditions, respectively, of conventional electrochemical systems. For plasma generation, high-voltage power supplies (negative polarity: Spellman SL10N300; positive polarity: Spellman SL10PN300) were integrated with a function generator (Tektronix AFG2021) and a pulse generator (DEI PVX-4110), which was connected to a plasma jet. The plasma jet used in this study is similar to the one reported in the previous literature.[11] Within the plasma jet, a ballast resistance (500 Ω) was connected in series with a tungsten needle. The tungsten needle was inserted inside a quartz capillary tube (inner diameter: 2 mm; outer diameter: 3 mm), through which He was supplied as the working gas at a flow rate of 3 standard liters per minute (SLPM). We note that the 3 SLPM He flow caused convection in the solution, which mitigated mass-transfer limitations between

the probe tip and the plasma-liquid interface. Plasma was ignited between the needle tip and the liquid surface with a fixed tip-to-liquid gap of 5 mm. The pulsed discharge was operated at a repetition frequency of 1 kHz; namely, one single period was 1000 μs. The plasma on-time, defined by the pulse width, was varied between 5 and 50 μs depending on the experimental condition. A clean Pt wire was employed as the grounding electrode. The plasma-liquid interaction was maintained for 30 minutes in each experiment. Discharge current profiles were measured using a Rogowski coil (Pearson 2877) and recorded with an oscilloscope (Tektronix DPO 2022B).

We also utilized a three-electrode rotating disk electrode (RDE) setup with Pt (8 mm in diameter) as the working electrode material and a clean Pt wire as the counter electrode to study the electrochemical system. We applied two fixed electrode potentials to the Pt disk electrode at three initial solution potentials. The two fixed electrode potentials represented the reduction and oxidation environments, respectively. Solution potential shifts were measured using the same setup described above for PDSE. All electrodes and solution potentials reported here were referenced to the same Ag/AgCl (3 M KCl) reference electrode. The RDE rotation rate was 500 rpm.

3.4 Results and Discussions

The data in Figure 3.1b show the relationship between the ferricyanide-to-ferrocyanide concentration ratios and the measured solution potential without applying plasma. The data show a complete agreement between the solution potential measured by the gold wire and the one predicted by the Nernst equation. The data in Figures 3.2a and 3.2b show the solution potentials, measured by the gold wire, before and after plasma interaction with the solution. We note that the change in the solution potential is a consequence of the plasma-induced change in the

concentration of oxidized and reduced forms of the redox couple. We used a 30-minute plasma-liquid interaction time with a plasma current of 2 mA and 50 µs pulse width. The current profiles are plotted in Figure 3.3. These current profiles are consistent across all redox couple concentrations due to their high conductivities.

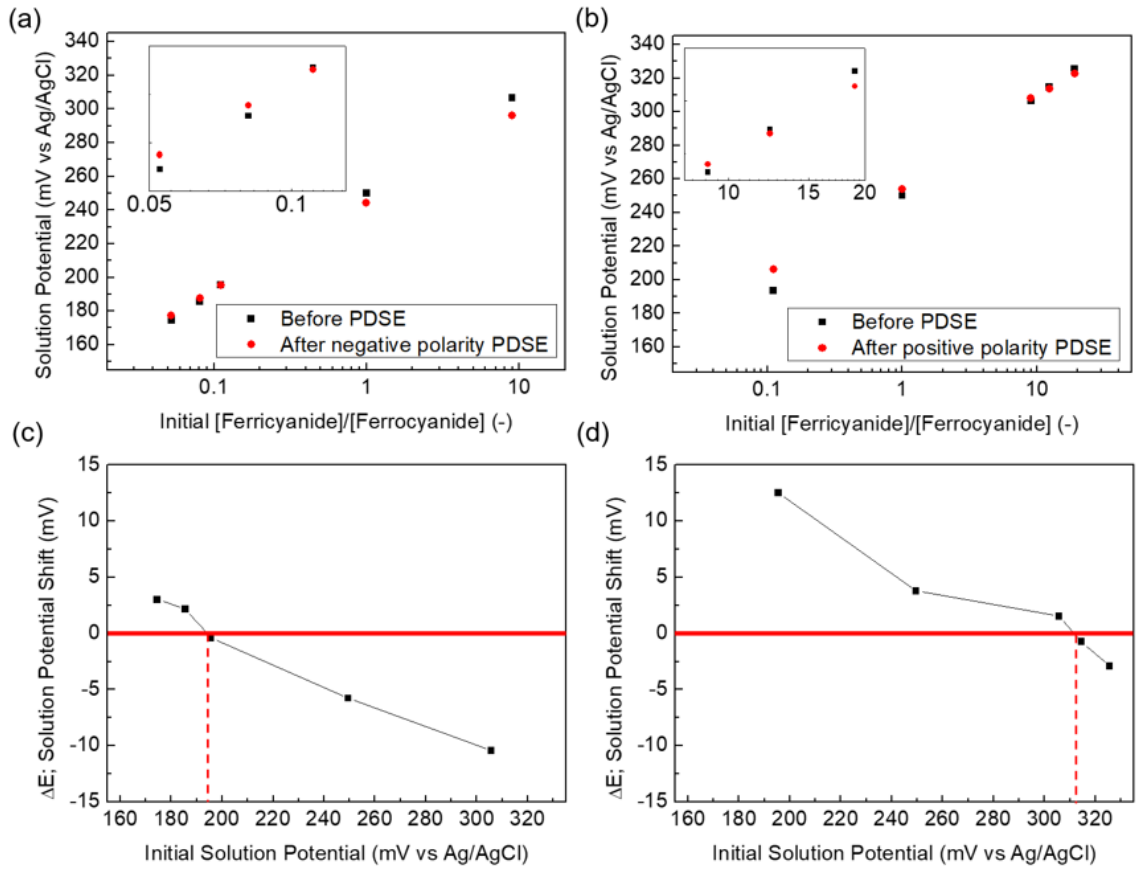


Figure 3.2 Solution potentials measured with an electrochemical probe before and after PDSE for (a) negative polarity plasma and (b) positive polarity plasma. Corresponding solution potential shifts derived from (a) and (b) under (c) negative polarity plasma and (d) positive polarity plasmas. The close-up views clearly illustrate the shifts for low initial ferricyanide-to-ferrocyanide ratios in (a) and high ferricyanide-to-ferrocyanide ratios in (b).

The data in Figure 3.2a were obtained with a negative polarity plasma. It is shown that for the high initial ferricyanide-to-ferrocyanide ratios (ferricyanide: oxidized form; ferrocyanide:

reduced form), upon application of the negative polarity plasma, negative solution potential shifts were observed, suggesting net reduction reactions. In contrast, other ratios showed positive solution potential shifts (see the close-up view), indicating net oxidation reactions. The data in Figure 3.2b show the results measured for the solutions interacting with a positive polarity plasma. It is shown that in this case, for the low initial ferricyanide-to-ferrocyanide ratios, positive solution potential shifts were observed, suggesting net oxidation reactions. Higher initial ferricyanide-to-ferrocyanide ratios showed slight negative solution potential shifts, suggesting net reduction reactions.

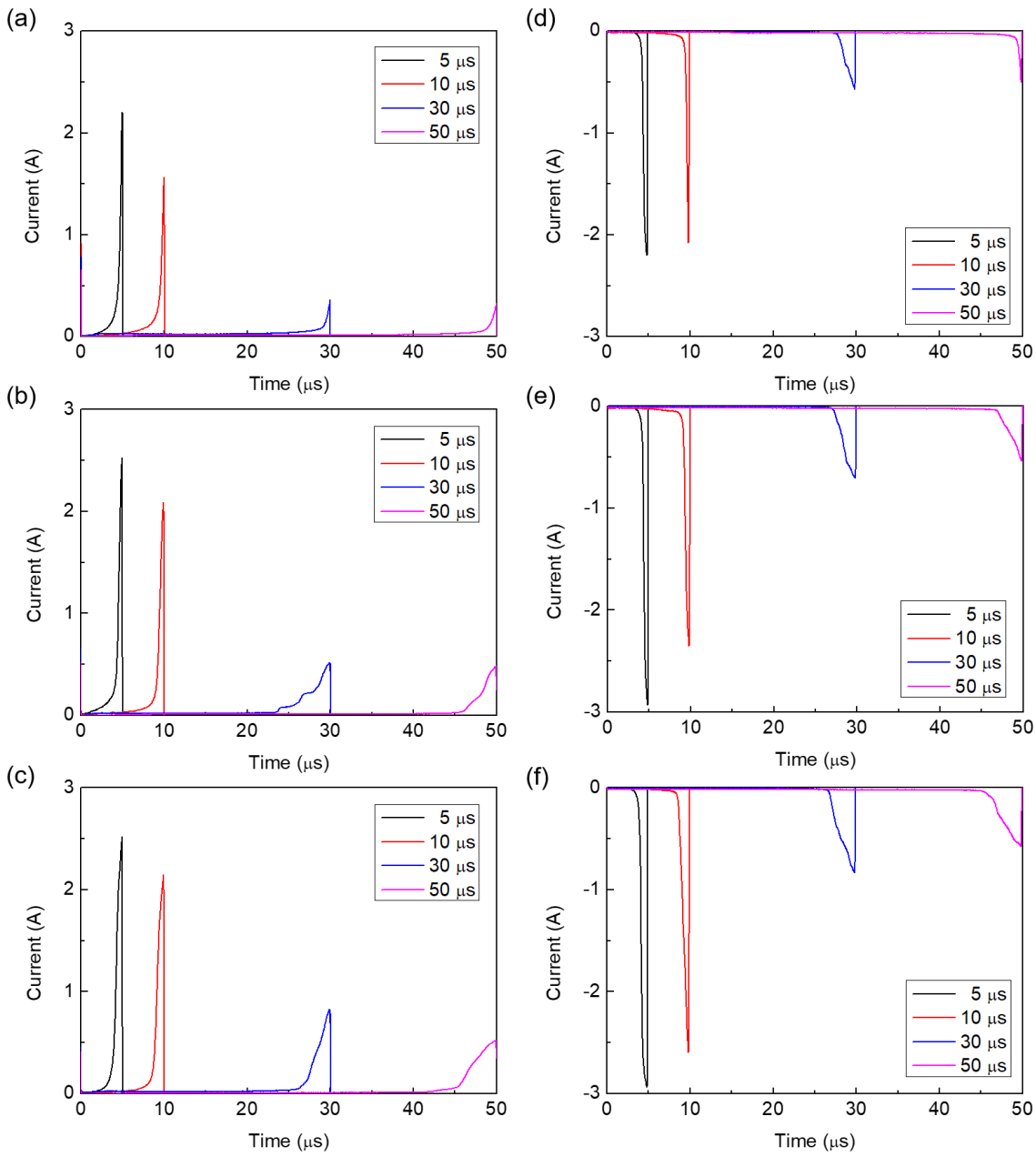


Figure 3.3 The measured current profiles for the negative polarity plasma with the current values (a) 1 mA, (b) 1.5 mA, and (c) 2 mA. The measured current profiles for the positive polarity plasma with the current values (d) 1 mA, (e) 1.5 mA, and (f) 2 mA. For a given current value, the total charge transfer per pulse is calculated and controlled by applying different voltages. During the pulse with a specified current value and a pulse width, a constant voltage is applied to the high-voltage electrode. The current values are defined to be positive when the current is from the liquid phase to the plasma phase.

Data in Figures 3.2c and 3.2d show the plasma-induced solution potential shifts (ΔE), calculated by subtracting the initial solution potentials (i.e., before the plasma treatment) from

the final solution potentials (i.e., after the plasma application), plotted against the initial solution potential. Using an analogy to conventional electrochemistry, under the condition of zero current (i.e., when there is no net conversion of the redox couple), the solution and electrode potentials are equal to each other. Based on this analogy, we can suggest that the "electrochemical" potential generated by plasma is the solution potential at which ΔE in Figures 3.2c and 3.2d is equal to zero. The data show that the plasma-generated "electrochemical' potential under the plasma conditions probed in the experiments in Figure 3.2 was 194 mV (Figure 3.2c) and 312 mV (Figure 3.2d) for the negative and positive polarity plasma, respectively.

We also note that the solution potential shifts were dependent on the probe position. In general, if the probe was moved away from the plasma-liquid interface, the solution potential shift decreased significantly. This might result from the mass-transfer limitations, as the concentration changes at the interface require time to be measured at the probe. Another factor might be that the input current values were not sufficient to induce a significant solution potential shift of the whole solution. Therefore, the plasma-generated electrochemical potentials have to be determined by an interpolation of the two closest points to a zero-solution potential shift. This makes sure that the no-net conversion phenomena were not due to mass-transfer limitations, but rather from PDSE-induced ratio changes at the interface.

ΔE, which corresponds to the changes in ferricyanide/ferrocyanide redox couple ratios, can also be correlated with the interfacial reactions driven by high-energy species. Previous studies have established that several high-energy species generated under PDSE react with ferricyanide/ferrocyanide. Among these species, e_{aq}^- and •OH radicals have been reported for both positive and negative polarity plasmas, exhibiting high reaction rate constants.[11, 25-26] We hypothesize that these two species are the dominant reactive species under PDSE and primarily

contribute to the observed changes in the redox couple ratio. The reaction with e_{aq}^- is $Fe(CN)_6^{3-}$ + $e_{aq}^- \rightarrow Fe(CN)_6^{4-}$, and the reaction with •OH is $Fe(CN)_6^{4-}$ + •OH → $Fe(CN)_6^{3-}$ + OH^-.[27]

Therefore, the change in ferricyanide concentration can be described using Equation 3.1.

$$\frac{d[Fe(CN)_6^{3-}]}{dt} = -k_{eaq}[e_{aq}^-][Fe(CN)_6^{3-}] + k_{OH}[\bullet OH][Fe(CN)_6^{4-}] \quad \text{(Equation 3.1)}$$

Table 3.2 Rate constants for the selected reactions

#	Reaction	Rate constant	Reference
3.1	$Fe(CN)_6^{3-} + e_{aq}^- \rightarrow Fe(CN)_6^{4-}$	$k_{eaq} = 1.2 \times 10^{10}\ M^{-1}\ s^{-1}$	[27]
3.2	$Fe(CN)_6^{4-} + \bullet OH \rightarrow Fe(CN)_6^{3-} + OH^-$	$k_{OH} = 1.1 \times 10^{10}\ M^{-1}\ s^{-1}$	[27]
3.3	$2\ e_{aq}^- + 2\ H_2O \rightarrow H_2 + 2\ OH^-$	$k_{H2O} = 1 \times 10^{8}\ M^{-3}\ s^{-1}$	[28-29]
3.4	$2 \bullet OH \rightarrow H_2O_2$	$k_{H2O2} = 5.5 \times 10^{9}\ M^{-1}\ s^{-1}$	[27]
3.5	$e_{aq}^- + NO_3^- \rightarrow NO_3^{2-}$	$k = 9.7 \times 10^{9}\ M^{-1}\ s^{-1}$	[27]
3.6	$\bullet OH + Cl^- \rightarrow ClOH^-$	$k = 4.3 \times 10^{9}\ M^{-1}\ s^{-1}$	[30]

Based on the measured ΔE in Figures 3.2c and 3.2d, we propose the following interfacial reaction mechanisms: For the negative polarity plasma, at relatively high ferricyanide-to-ferrocyanide concentration ratios, the reduction of ferricyanide by e_{aq}^- dominated, resulting in a decrease in ferricyanide concentration and a negative ΔE. At lower ratios, the rates of these two reactions became comparable, and in some cases, net oxidation occurred, causing only a slight decrease or even an increase in ferricyanide concentration. Conversely, for the positive polarity plasma, at relatively low ferricyanide-to-ferrocyanide concentration ratios, oxidation of ferrocyanide by •OH radicals dominated, leading to an increase in ferricyanide concentration and a positive ΔE. At higher ratios, this dominance weakened, and the ferricyanide concentration increased only slightly or even decreased, indicating minimal changes in the solution potential or a negative ΔE.

At the plasma-generated electrochemical potential, that is, $\Delta E = 0$, the net ferricyanide concentration change is zero. By setting $\frac{d[Fe(CN)_6^{3-}]}{dt} = 0$, we derived Equation 3.2, which describes the effective concentration ratio between e_{aq}^- and •OH. This ratio was calculated using the reported rate constants (Table 3.2) and the ferricyanide-to-ferrocyanide concentration ratios where $\Delta E = 0$. Based on this analysis, we find that for the negative polarity plasma, the effective e_{aq}^--to-•OH concentration ratio was ~ 8.7 (Figure 3.2a), and for the positive polarity plasma, the effective •OH-to-e_{aq}^- concentration ratio was ~ 12.1 (Figure 3.2b).

$$\frac{[e_{aq}^-]}{[\cdot OH]} = \frac{k_{OH}\,[Fe(CN)_6^{4-}]}{k_{eaq}\,[Fe(CN)_6^{3-}]} \quad \text{(Equation 3.2)}$$

We conducted additional experiments to correlate reactions driven by high-energy species with the measured plasma-generated electrochemical potentials, which we also interpret as effective concentration ratios. As shown previously, both the measured potentials and effective concentration ratios depend on plasma polarity. We hypothesized that, at a fixed polarity, these two quantities can also be modulated by competing interfacial reactions, specifically, the reaction of water with e_{aq}^- ($2\ e_{aq}^- + 2\ H_2O \rightarrow H_2 + 2\ OH^-$; Reaction 3.3) and the recombination reaction of •OH ($2\ \cdot OH \rightarrow H_2O_2$; Reaction 3.4), which are primary consumption pathways for these reactive species if not reacting with the redox couple.[27, 29] This hypothesis is tested by varying the plasma operating parameters, current and pulse width, which adjust the peak current within each pulse. As the peak current changes, the rates of the competing reactions vary, leading to a dependence on the plasma parameters. Within the tested parameters, for a given current (1.0, 1.5, and 2.0 mA), the total charge input per pulse was held constant while the pulse width (5, 10, 30, and 50 μs) was varied. The corresponding current profiles are shown in Figure 3.3. For a fixed current, an increase in pulse width resulted in a lower peak current value. While for a fixed pulse width, an increase in current resulted in a higher peak current value.

The data in Figure 3.4a show the plasma-generated electrochemical potentials for the negative polarity plasma with the specified currents and pulse widths. Although the dependence was less pronounced than the polarity effect, the potentials decreased with decreasing current and increasing pulse width, indicating a plasma parameter-dependent shift. The measured potentials were below the formal potential of the redox couple, indicating that the reduction reaction was the dominant reaction pathway. Conversely, the data in Figure 3.4b show the positive polarity case at the same operating conditions. A comparable dependence on current and pulse width was observed. The measured potentials were above the formal potential of the redox couple, indicating that the oxidation reaction was the dominant reaction pathway. These results aligned with our hypothesis that the plasma-generated electrochemical potential is a function of plasma parameters.

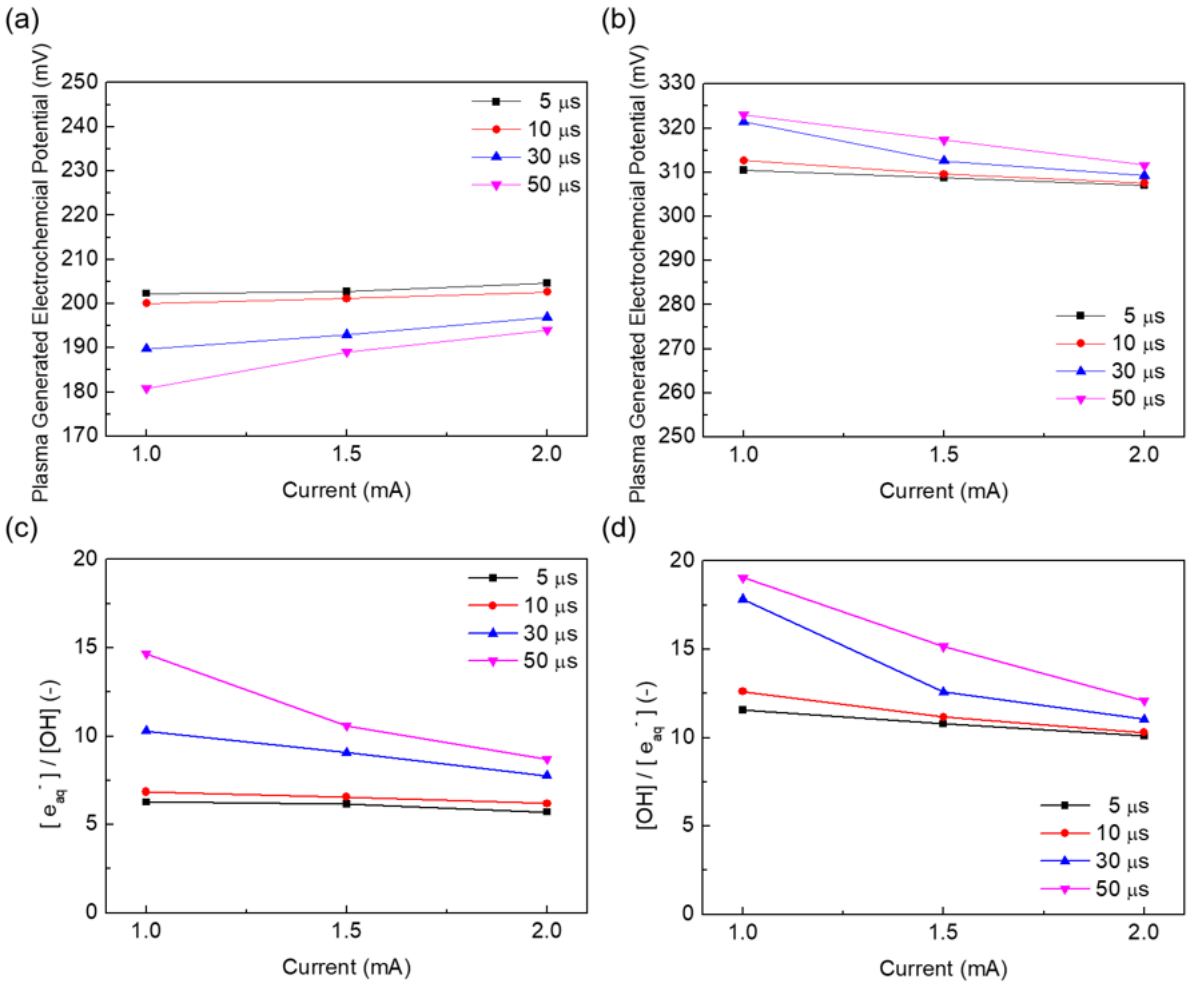


Figure 3.4 Plasma-generated electrochemical potentials for (a) negative polarity plasma and (b) positive polarity plasma. High-energy species ratios for (c) negative polarity plasma and (d) positive polarity plasma.

From Equation 3.2, the effective concentration ratios of e_{aq}^- and •OH are calculated from the plasma-generated electrochemical potentials and shown in Figures 3.4c and 3.4d. The data in Figure 3.4c show the effective concentration ratios of e_{aq}^--to-•OH for the negative polarity plasma. The decline in the ratio with increasing current and decreasing pulse width might result from consumption of e_{aq}^- via Reaction 3.3, which exhibits an apparent second-order rate dependence on the e_{aq}^- concentration (Equation 3.3). For a fixed current input, shortening the pulse width increased the peak current, elevating the interfacial e_{aq}^- concentration over a shorter

on-time. This increase in e_{aq}^- concentration led to a higher consumption of e_{aq}^- by Reaction 3.3, which exhibits a second-order consumption rate of e_{aq}^-, reducing the effective e_{aq}^- concentration probed by the redox couple and therefore the ratios. For a fixed pulse width, the ratios showed little dependence on current. The observed slight decrease at higher current may reflect an increased gas-to-liquid •OH flux, as reported previously.[11]

$$\frac{d[e_{aq}^-]}{dt} = -k_{eaq}[e_{aq}^-][Fe(CN)_6^{3-}] - k_{H2O}[e_{aq}^-]^2[H_2O]^2 \quad \text{(Equation 3.3)}$$

$$\frac{d[\cdot OH]}{dt} = -k_{OH}[\cdot OH][Fe(CN)_6^{4-}] - k_{H2O2}[\cdot OH]^2 \quad \text{(Equation 3.4)}$$

The •OH-to-e_{aq}^- effective concentration ratios for the positive polarity plasma are presented in Figure 3.4d. The ratios exhibited a trend similar to that observed for the negative polarity plasma, which may be attributed to the recombination of •OH to form H_2O_2 (Reaction 3.4). This reaction also follows an apparent second-order rate dependence on the •OH concentration (Equation 3.4). Comparing the two polarities at the same current and pulse width, the positive polarity plasma showed higher effective concentration ratios of •OH-to-e_{aq}^- than the e_{aq}^--to-•OH effective concentration ratios observed for the negative polarity plasma. This might result from the longer lifetime and higher penetration depth of •OH, as reflected by the lower rate constant of Reaction 3.4 compared with Reaction 3.3.

In addition to the consumption reactions and the gas-to-liquid mass transfer of neutral radicals (especially •OH)[11] mentioned above, we also note that the contributions from other non-Faradaic processes (non-charge transfer), such as the generation of the e_{aq}^- and •OH from photolysis,[31] and from mass transfer-limitations[32-33] may also influence the measured potentials and the effective concentration ratios for both polarities. Here, we further discuss these factors. From the literature, Yue *et al.* demonstrated the time-dependence of electron and •OH fluxes in a pulse, illustrated in Figure 3.5.[11] In our work, the no-net conversion from the negative polarity

PDSE might result from the discrepancy in time between the two fluxes. When the pulse is on, electron flux is more dominant and tends to drive reduction reactions. When the pulse is off, •OH flux becomes dominant and oxidizes the redox couple, leading to an overall no-net conversion.

On the other hand, the positive polarity PDSE might involve the generation of both •OH and e_{aq}^- from the cation charge transfer. Martin *et al.* measured a yield of approximately one electron and two •OH per incident ion.[25] In their case, they used a continuous argon (Ar) plasma with water and assumed the cations to be argon ions (Ar^+). The yields of reactive species they measured may not apply to our pulsed He-water system, but the generation of reactive species via cation bombardment should be similar. We also note that photolysis processes might play a role in the system, leading to the generation of •OH, hydrogen atoms (•H), and e_{aq}^-.[31]The complexity of the interface makes decoupling these processes challenging, whereas our system provides an estimate of their overall contribution.

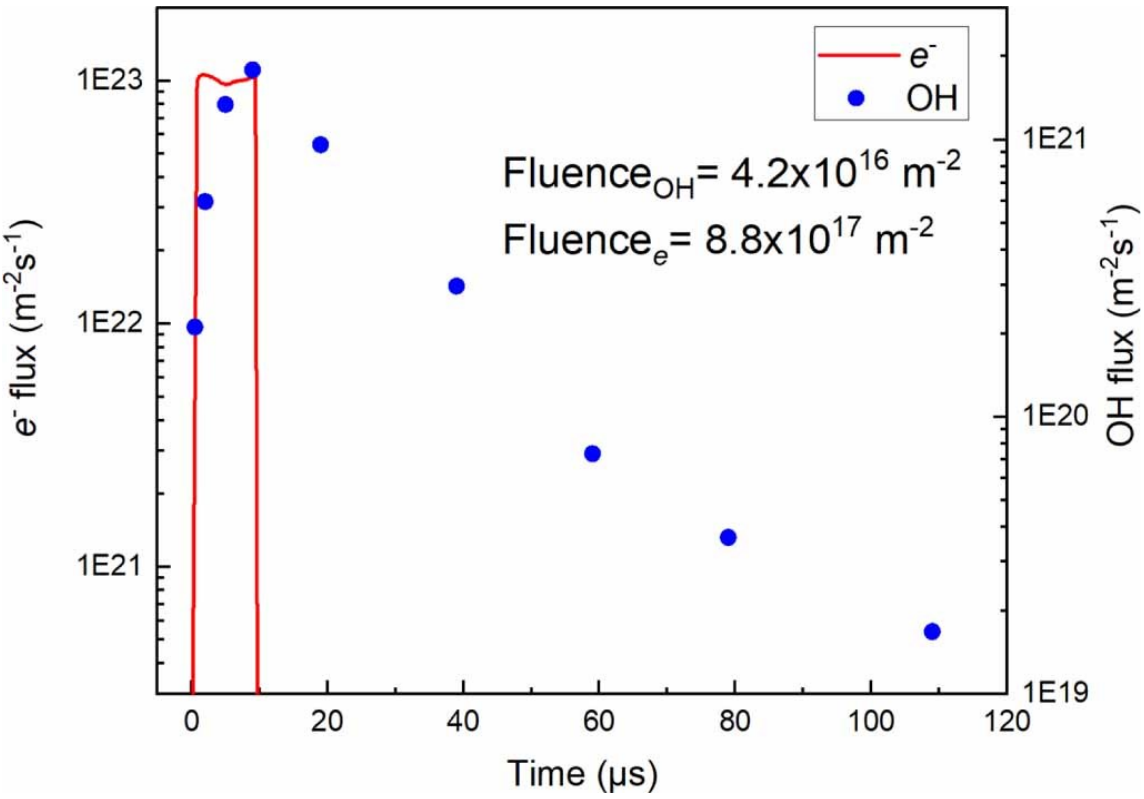


Figure 3.5 The electron and •OH fluxes to the liquid surface as a function of time for a voltage pulse width of 9 μs. The electron flux was estimated from the interfacial surface area and the current. The •OH flux was estimated by the number density gradient times the diffusion coefficient of •OH near the liquid interface. Adapted from [11].

The effect of the local chemical environment on the measured plasma-generated electrochemical potentials and the effective concentration ratios was further demonstrated by introducing scavengers of high-energy species. We hypothesized that, under identical plasma parameters, scavenging these species would introduce additional consumption pathways alongside the Reactions 3.3 and 3.4, thereby altering the measured plasma-generated electrochemical potentials and the effective concentration ratios. To test this hypothesis, nitrate ions (NO_3^-), which scavenge e_{aq}^- ($e_{aq}^- + NO_3^- \rightarrow NO_3^{2-}$; Reaction 3.5), were introduced into the solution for the negative polarity plasma. For the positive polarity plasma, chlorine ions (Cl^-), which quench •OH (•OH + $Cl^- \rightarrow ClOH^-$; Reaction 3.6), were introduced.[30]

The measured potentials for the negative polarity plasma are illustrated in Figure 3.6a with and without 100 mM KNO_3. Under the same plasma parameters, an increase was observed while adding NO_3^-, suggesting that the reduced form (ferrocyanide) became less dominant. The measured potentials for the positive polarity plasma are plotted in Figure 3.6b with and without 100 mM KCl. Under the same plasma parameters, a decrease was observed while adding Cl^-, suggesting that the oxidized form (ferricyanide) became less dominant. These shifts are consistent with the hypothesis that the plasma-generated electrochemical potentials are governed by reactions involving high-energy species and are dependent on changes in the local chemical environment.

Meanwhile, the addition of scavengers demonstrated that the introduction of additional consumption pathways influences the effective concentration ratios. The data in Figure 3.6c show that for the negative polarity plasma, the e_{aq}^--to-•OH effective concentration ratios decreased with 100 mM KNO_3, as NO_3^- scavenges e_{aq}^-. Similarly, the data in Figure 3.6d show that for the positive polarity plasma, the •OH-to-e_{aq}^- effective concentration ratios also decreased with 100 mM KCl, as Cl^- quenches •OH. These findings show that additional consumption reactions lower the effective concentration ratios, underscoring the importance of the local chemical environment in PDSE. These experiments also confirm that e_{aq}^- and •OH are the dominant species in a PDSE system.

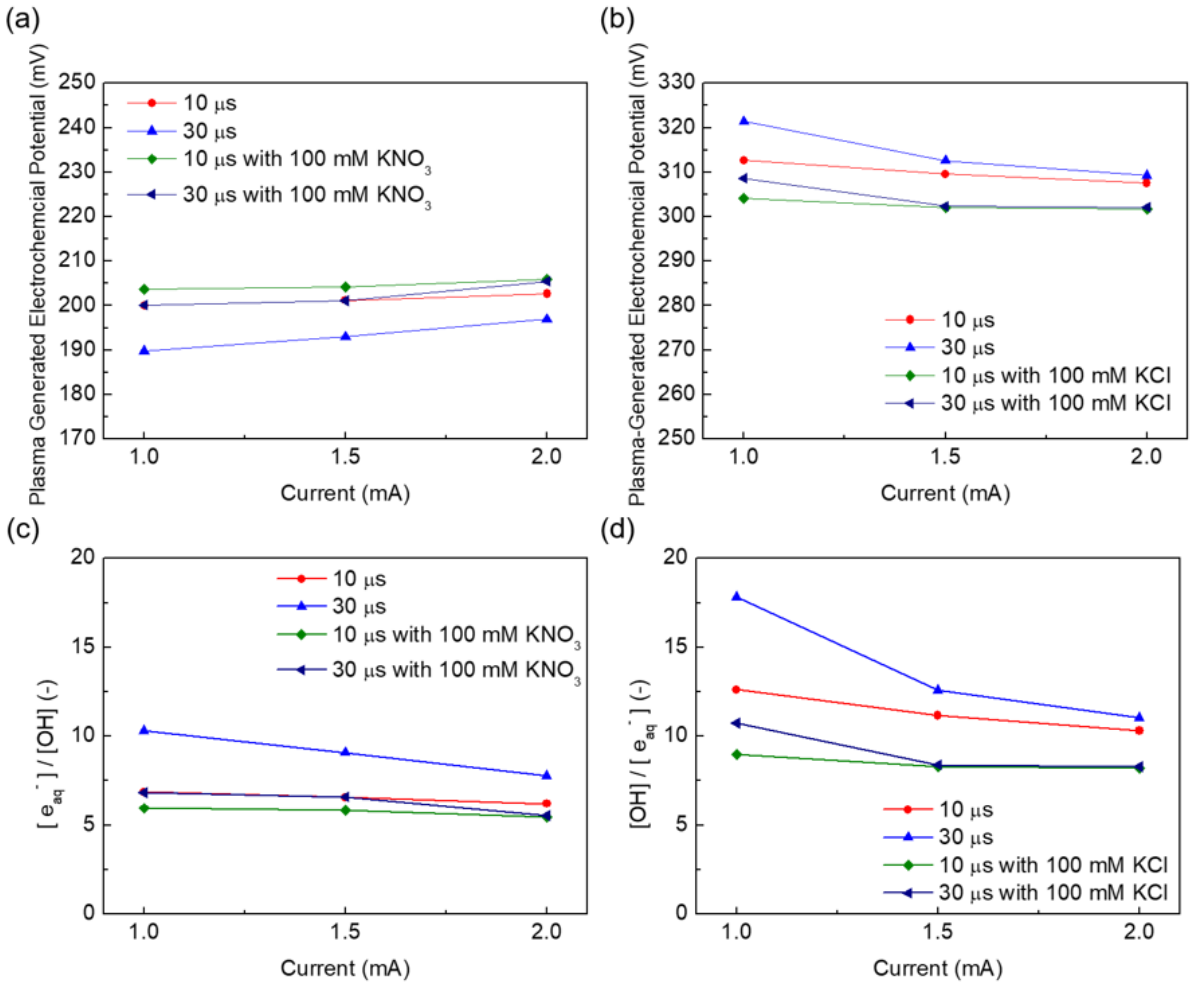


Figure 3.6 Plasma-generated electrochemical potentials for (a) negative polarity plasma with 100 mM KNO_3 and (b) positive polarity plasma with 100 mM KCl. High-energy species ratios for (c) negative polarity plasma with 100 mM KNO_3 and (d) positive polarity plasma with 100 mM KCl.

We also performed electrochemical experiments to directly compare PDSE with conventional electrochemical systems. The plasma electrode was replaced by a rotating Pt disk electrode, illustrated in Figure 3.7a. The Pt disk is rotating at 500 rpm. We applied fixed electrode potentials to the electrode for 10 minutes. The applied electrode potentials (310 mV and 190 mV) were close to the plasma-generated electrochemical potentials measured under PDSE. The electrode and solution potentials here were also versus the same reference electrode used for the electrochemical probe. The initial and final solution potentials were measured with

the probe configuration. The data in Figure 3.7b illustrate the solution potential shifts versus the initial solution potentials for two applied potentials. The initial solution potentials were 195, 250, and 305 mV. The data show that the solution potentials of the redox couple shifted toward the applied electrode potentials. For the applied electrode potential of 190 mV, solutions with higher solution potentials shifted more negatively, while for the applied potential of 310 mV, solutions with lower initial solution potentials shifted more positively. It is also demonstrated that the solution potential shifts became negligible when the solution potential and the electrode potential were close. These results resemble the PDSE case, where the solution potentials shifted toward the plasma-generated electrochemical potentials.

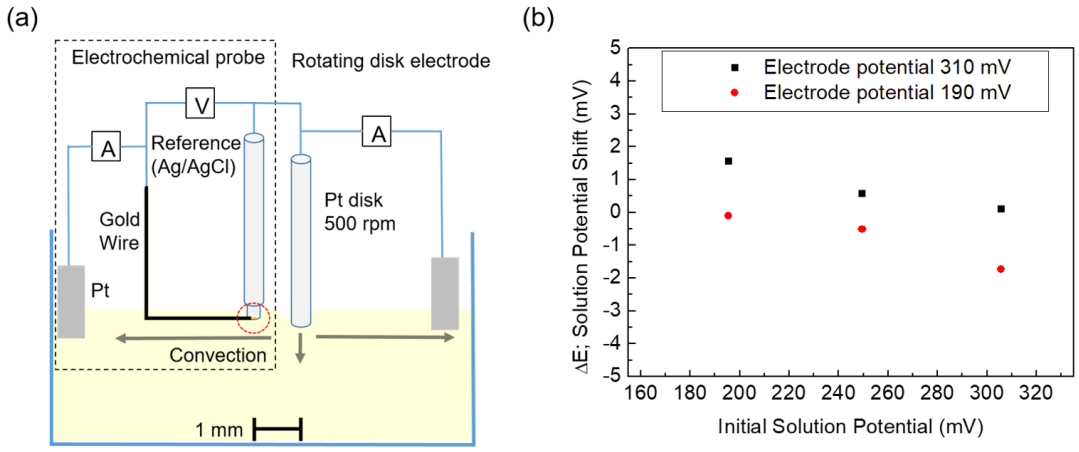


Figure 3.7 (a) Schematic of the Pt electrode setup and the electrochemical probe with a three-electrode setup. (b) The measured solution potential shifts versus the initial solution potentials after applying 310 mV and 190 mV to the Pt electrode at 500 rpm. The electrode potentials were applied against an Ag/AgCl reference electrode.

We also compared the solution potential shifts with the addition of high-energy species scavengers, NO_3^- and Cl^-. The addition of NO_3^- was used to resemble negative polarity plasma conditions, while the addition of Cl^- was used to resemble positive polarity plasma conditions. The data in Figure 3.8a illustrate the solution potential shifts for an initial solution potential of

195 mV. We applied electrode potentials for both 190 and 310 mV with and without 100 mM NO_3^-. The solution potential shifts were unchanged by NO_3^-, confirming that the reduction reaction in a conventional electrochemical system is not affected by these scavengers. Similarly, for an initial solution potential of 305 mV, we applied the two electrode potentials with and without adding 100 mM Cl^-. As no change in the solution potential shifts was observed, illustrated in Figure 3.8b, it is confirmed that the oxidation reaction in a conventional electrochemical system is not affected by the scavengers. Collectively, these experiments showed that the solution potential shifts toward a characteristic interfacial potential in both cases (conventional electrochemistry: electrode potential; PDSE: plasma-generated electrochemical potential). However, because the reaction mechanisms differ, adding scavengers led to different effects on the solution potential shifts.

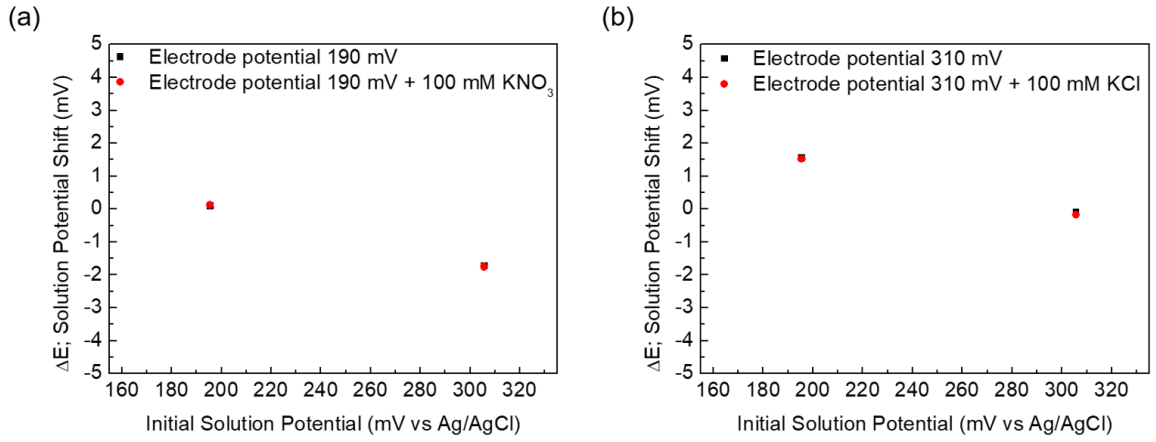


Figure 3.8 Solution potential shifts versus initial solution potentials for (a) an applied electrode potential of 190 mV with and without 100 mM KNO_3, and (b) an applied electrode potential of 310 mV with and without 100 mM KCl. The data indicate that these scavengers do not affect reduction or oxidation in the conventional electrochemical system.

3.5 Conclusions

In conclusion, we characterized plasma-liquid interactions using an electrochemical probe methodology that bridges the understanding of PDSE with conventional electrochemical approaches. We employed a gold wire probe to measure the OCP at the interface of plasma and a solution containing a ferricyanide/ferrocyanide redox couple. These measurements allowed us to shed light on how applying plasma impacts the electrochemical potential at the interface. We extended these studies by using the measured potential to determine the effective local concentrations of highly reactive species (mainly e_{aq}^- and •OH that drive chemical transformations at the plasma-liquid interfaces). These measurements quantified the relative concentrations of e_{aq}^- and •OH radicals as a function of plasma polarity and various input parameters. We also observed that solution potential shifts in PDSE showed a similar tendency to those obtained by applying a fixed electrode potential in a conventional electrochemical system, whereas adding scavengers led to different results due to differences in reaction mechanisms.

3.6 References

1. Bruggeman, P. J.; Frontiera, R. R.; Kortshagen, U.; Kushner, M. J.; Linic, S.; Schatz, G. C.; Andaraarachchi, H.; Chaudhuri, S.; Chen, H.-T.; Clay, C. D.; Dias, T. C.; Doyle, S.; Jones, L. O.; Meyer, M.; Mueller, C. M.; Nam, J. H.; Raisanen, A.; Rich, C. C.; Srivastava, T.; Xu, C.; Xu, D.; Zhang, Y., Advances in Plasma-Driven Solution Electrochemistry. *The Journal of Chemical Physics* **2025,** *162* (7),

2. Bruggeman, P. J.; Frontiera, R. R.; Kortshagen, U. R.; Kushner, M. J.; Linic, S.; Schatz, G. C.; Andaraarachchi, H.; Exarhos, S.; Jones, L. O.; Mueller, C. M.; Rich, C. C.; Xu, C.; Yue,

Y.; Zhang, Y., Plasma-Driven Solution Electrolysis. *Journal of Applied Physics* **2021,** *129* (20), 200902.

3. Richmonds, C.; Witzke, M.; Bartling, B.; Lee, S. W.; Wainright, J.; Liu, C.-C.; Sankaran, R. M., Electron-Transfer Reactions at the Plasma–Liquid Interface. *Journal of the American Chemical Society* **2011,** *133* (44), 17582-17585.

4. Rumbach, P.; Bartels, D. M.; Sankaran, R. M.; Go, D. B., The Solvation of Electrons by an Atmospheric-Pressure Plasma. *Nature Communications* **2015,** *6* (1), 7248.

5. Wang, J.; Üner, N. B.; Dubowsky, S. E.; Confer, M. P.; Bhargava, R.; Sun, Y.; Zhou, Y.; Sankaran, R. M.; Moore, J. S., Plasma Electrochemistry for Carbon–Carbon Bond Formation Via Pinacol Coupling. *Journal of the American Chemical Society* **2023,** *145* (19), 10470-10474.

6. Srivastava, T.; Chaudhuri, S.; Rich, C. C.; Schatz, G. C.; Frontiera, R. R.; Bruggeman, P., Probing Time-Resolved Plasma-Driven Solution Electrochemistry in a Falling Liquid Film Plasma Reactor: Identification of HO_2^- as a Plasma-Derived Reducing Agent. *The Journal of Chemical Physics* **2024,** *160* (9),

7. Cserfalvi, T.; Mezei, P., Operating Mechanism of the Electrolyte Cathode Atmospheric Glow Discharge. *Fresenius' Journal of Analytical Chemistry* **1996,** *355* (7), 813-819.

8. Clay, C. D.; Mueller, C. M.; Rich, C. C.; Schatz, G. C.; Bruggeman, P. J.; Frontiera, R. R., Evidence for Superoxide-Initiated Oxidation of Aniline in Water by Pulsed, Atmospheric Pressure Plasma. *The Journal of Physical Chemistry Letters* **2024,** *15* (27), 6918-6926.

9. Xu, C.; Chaudhuri, S.; Held, J.; Andaraarachchi, H. P.; Schatz, G. C.; Kortshagen, U. R., Silver Nanoparticle Synthesis in Glycerol by Low-Pressure Plasma-Driven Electrolysis: The Roles of Free Electrons and Photons. *The Journal of Physical Chemistry Letters* **2023,** *14* (44), 9960-9968.

10. Nayak, G.; Wang, J.; Li, R.; Aranzales, D.; Thagard, S. M.; Bruggeman, P. J., Non-OH-Driven Liquid-Phase Chemistry in Water Microdroplets. *Plasma Processes and Polymers* **2023,** *20* (5), 2200222.

11. Yue, Y.; Exarhos, S.; Nam, J.; Lee, D.; Linic, S.; Bruggeman, P. J., Quantification of Plasma Produced OH and Electron Fluxes at the Liquid Anode and Their Role in Plasma Driven Solution Electrochemistry. *Plasma Sources Science and Technology* **2022,** *31* (12), 125008.

12. Hefny, M. M.; Pattyn, C.; Lukes, P.; Benedikt, J., Atmospheric Plasma Generates Oxygen Atoms as Oxidizing Species in Aqueous Solutions. *Journal of Physics D: Applied Physics* **2016,** *49* (40), 404002.

13. Delgado, H. E.; Elg, D. T.; Bartels, D. M.; Rumbach, P.; Go, D. B., Chemical Analysis of Secondary Electron Emission from a Water Cathode at the Interface with a Nonthermal Plasma. *Langmuir* **2020,** *36* (5), 1156-1164.

14. Hawtof, R.; Ghosh, S.; Guarr, E.; Xu, C.; Mohan Sankaran, R.; Renner, J. N., Catalyst-Free, Highly Selective Synthesis of Ammonia from Nitrogen and Water by a Plasma Electrolytic System. *Science Advances* **2019,** *5* (1), eaat5778.

15. Chen, H.-T.; Lee, D.; Linic, S., Formation of Mixed Bimetallic Nanoparticles of Immiscible Metals through Plasma-Induced Reduction of Precursors in Solutions: A Case Study of Ag–Pt Alloy Nanoparticles. *Chemistry of Materials* **2023,** *35* (16), 6557-6565.

16. Lee, D.; Chen, H.-T.; Linic, S., Plasma-Induced Selective Propylene Epoxidation Using Water as the Oxygen Source. *JACS Au* **2023,** *3* (4), 997-1003.

17. Bloomquist, C. K.; Naumov, D.; Yang, A.; Mathison, R.; Herzog, B. D.; Tenn, W. J., III; Modestino, M. A.; Aydil, E. S., Exploring the Balance between Faradaic and Non-Faradaic

Processes in Organic Chemical Reactions at Plasma-Liquid Interfaces. *Journal of the American Chemical Society* **2025,** *147* (16), 13937-13947.

18. Vanraes, P.; Bogaerts, A., The Essential Role of the Plasma Sheath in Plasma–Liquid Interaction and Its Applications—a Perspective. *Journal of Applied Physics* **2021,** *129* (22),

19. Bruggeman, P. J.; Kushner, M. J.; Locke, B. R.; Gardeniers, J. G. E.; Graham, W. G.; Graves, D. B.; Hofman-Caris, R. C. H. M.; Maric, D.; Reid, J. P.; Ceriani, E.; Fernandez Rivas, D.; Foster, J. E.; Garrick, S. C.; Gorbanev, Y.; Hamaguchi, S.; Iza, F.; Jablonowski, H.; Klimova, E.; Kolb, J.; Krcma, F.; Lukes, P.; Machala, Z.; Marinov, I.; Mariotti, D.; Mededovic Thagard, S.; Minakata, D.; Neyts, E. C.; Pawlat, J.; Petrovic, Z. L.; Pflieger, R.; Reuter, S.; Schram, D. C.; Schröter, S.; Shiraiwa, M.; Tarabová, B.; Tsai, P. A.; Verlet, J. R. R.; von Woedtke, T.; Wilson, K. R.; Yasui, K.; Zvereva, G., Plasma–Liquid Interactions: A Review and Roadmap. *Plasma Sources Science and Technology* **2016,** *25* (5), 053002.

20. Bard, A. J.; Faulkner, L. R., *Electrochemical Methods: Fundamentals and Applications*. Sec. ed.; John Wiley & Sons: New York, 2001.

21. Boettcher, S. W.; Oener, S. Z.; Lonergan, M. C.; Surendranath, Y.; Ardo, S.; Brozek, C.; Kempler, P. A., Potentially Confusing: Potentials in Electrochemistry. *ACS Energy Letters* **2021,** *6* (1), 261-266.

22. Oldham, T.; Chen, M.; Sharkey, S.; Parker, K. M.; Thimsen, E., Electrochemical Characterization of the Plasma-Water Interface. *Journal of Physics D: Applied Physics* **2020,** *53* (16), 165202.

23. Isaacs, H. S.; Vyas, B., Scanning Reference Electrode Techniques in Localized Corrosion. Brookhaven National Lab., Upton, NY (USA): United States, 1979.

24. Oldham, T.; Thimsen, E., Electrochemical Structure of the Plasma–Liquid Interface. *The Journal of Physical Chemistry C* **2022,** *126* (2), 1222-1229.

25. Martin, D. C.; Elg, D. T.; Delgado, H. E.; Nguyen, H. M.; Rumbach, P.; Bartels, D. M.; Go, D. B., Optical and Chemical Measurements of Solvated Electrons Produced in Plasma Electrolysis with a Water Cathode. *Langmuir* **2024,** *40* (28), 14224-14232.

26. Thai, V.-P.; Saito, N.; Nakamura, T.; Takahashi, K.; Sasaki, T.; Kikuchi, T., Effect of Voltage Polarity and Supply Frequency on the Properties of Plasma Contacting Liquid Electrodes and Gold Nanoparticle Synthesis. *Plasma Sources Science and Technology* **2022,** *31* (1), 015006.

27. Buxton, G. V.; Greenstock, C. L.; Helman, W. P.; Ross, A. B., Critical Review of Rate Constants for Reactions of Hydrated Electrons, Hydrogen Atoms and Hydroxyl Radicals (·OH/·O^- in Aqueous Solution. *Journal of Physical and Chemical Reference Data* **1988,** *17* (2), 513-886.

28. Tian, W.; Kushner, M. J., Atmospheric Pressure Dielectric Barrier Discharges Interacting with Liquid Covered Tissue. *Journal of Physics D: Applied Physics* **2014,** *47* (16), 165201.

29. Madden, K. P.; Mezyk, S. P., Critical Review of Aqueous Solution Reaction Rate Constants for Hydrogen Atoms. *Journal of Physical and Chemical Reference Data* **2011,** *40* (2), 023103.

30. Jayson, G. G.; Parsons, B. J.; Swallow, A. J., Some Simple, Highly Reactive, Inorganic Chlorine Derivatives in Aqueous Solution. Their Formation Using Pulses of Radiation and Their Role in the Mechanism of the Fricke Dosimeter. *Journal of the Chemical Society, Faraday Transactions 1: Physical Chemistry in Condensed Phases* **1973,** *69* (0), 1597-1607.

31. Heit, G.; Neuner, A.; Saugy, P.-Y.; Braun, A. M., Vacuum-UV (172 nm) Actinometry. The Quantum Yield of the Photolysis of Water. *The Journal of Physical Chemistry A* **1998,** *102* (28), 5551-5561.

32. Delgado, H. E.; Radomsky, R. C.; Martin, D. C.; Bartels, D. M.; Rumbach, P.; Go, D. B., Effect of Competing Oxidizing Reactions and Transport Limitation on the Faradaic Efficiency in Plasma Electrolysis. *Journal of The Electrochemical Society* **2019,** *166* (6), E181-E186.

33. Nayak, G.; Oinuma, G.; Yue, Y.; Santos Sousa, J.; Bruggeman, P. J., Plasma-Droplet Interaction Study to Assess Transport Limitations and the Role of·OH, O·,H·,$O_2(s^1\Delta_g)$,O_3, He(2^3S) and Ar($1s_5$) in Formate Decomposition. *Plasma Sources Science and Technology* **2021,** *30* (11), 115003.

Chapter 4 Formation of Mixed Bimetallic Nanoparticles of Immiscible Metals through Plasma-Induced Reduction of Precursors in Solutions: A Case Study of Ag−Pt Alloy Nanoparticles

4.1 Summary

Bimetallic alloy nanomaterials exhibit promising properties in various applications. The synthesis of these nanomaterials is often challenging due to the immiscibility of the constituent metals. To overcome this issue, complex synthetic strategies relying on difficult-to-control reduction conditions have been utilized, which show that rapid reduction and quenching are required to kinetically trap immiscible metal atoms in single nanoparticles. In this study, we demonstrate a simpler synthetic strategy to form well-mixed bimetallic nanoparticles of immiscible metals. We exploit the interactions between pulsed plasma and solutions charged with metal precursor salts to rapidly form metal atoms. We demonstrate that the minimal requirements for the formation of alloys include the following: (1) the metal precursor reduction rates are high enough to allow the kinetic trapping of metal monomers, (2) the reduction rates are similar for the respective metal precursors, ensuring a consistent mixing during the growth process, and (3) the nucleation process is controlled to avoid the “burst nucleation” which takes place when the local concentrations of reduced metal atom monomers exceed a critical threshold. Dongho Lee proposed the relationship between rate constants and the reduction potentials, chose the platinum precursor, and revised the manuscript. Han-Ting Chen performed the experiments,

proposed the thermal polyol method and the nucleation theory, and drafted the manuscript. They contributed equally to this work. This paper is published in *Chemistry of Materials*.[1]

4.2 Introduction

Bimetallic alloy nanoparticles exhibit unique chemical and physical properties compared to their individual constituent metals.[2] In some instances; however, it is challenging to synthesize targeted bimetallic nanoparticles due to the intrinsic immiscibility of two metals.[3-5] For example, silver and more broadly 4d transition metals are not very miscible with most other metals.[6-7] Synthesis of these nanomaterials generally requires strategies that involve the kinetic trapping of two metal salts into a single molecular structure (bimetallic molecular precursor) and then rapidly reducing these structures by utilizing strong reducing environments, such as high particle energy radiation (i.e., γ rays),[8] high temperature,[9-11] or high intensity visible light.[12] These strategies are challenged by the complexities and limitations associated with the synthesis of the bimetallic molecular precursors that ensure the mixing of the metals before reduction reactions.[13] Moreover, the high-temperature reduction, followed by a quenching, often leads to sintering and agglomeration of the nanoparticles, making them not well-suited for applications that require high surface-to-volume ratios, such as heterogeneous catalysis and electrocatalysis.[14] The utilization of visible light also requires high light intensity and can only be applied to those materials that can readily absorb light. It is clear that to avoid the agglomeration problem and develop a more general method for bimetallic nanomaterial synthesis, other methods that lead to a rapid co-reduction of precursors in liquid solutions (i.e., water) are required.

Herein, we propose a strategy to synthesize bimetallic materials that contain metals that are not readily miscible. We illustrate the approach in a case study of bimetallic silver (Ag)-platinum (Pt) nanoparticles. The strategy employs direct-current (DC) plasma which interacts

with a liquid solution charged with Pt- and Ag-metal salts.[15-16] We demonstrate that under certain conditions, discussed below, these plasma-liquid interactions generate a highly reactive plasma-liquid interfacial environment that triggers a rapid co-reduction of two metal salts and the synthesis of Ag-Pt alloy nanomaterials.[17] We note that plasma co-reduction strategies have been employed previously to synthesize inherently miscible metal alloys, such as gold-silver,[18] copper-palladium,[19] and gold-palladium.[20] We also discuss below the impact of precursor concentrations and pulse settings on the nanoparticle nucleation and growth process. We anticipate that similar plasma-induced rapid co-reduction strategies can be developed to synthesize alloys of other immiscible metals.

4.3 Experimental Section

One-pot Ag-Pt nanoparticles were synthesized using pulsed DC plasma-liquid interactions (Figure 4.1a). In a typical synthesis, silver nitrate ($AgNO_3$) and tetraammineplatinum(II) nitrate ($Pt(NH_3)_4(NO_3)_{2)}$ were added to 3 ml of ethylene glycol (EG) or water (18.2 MΩ·cm at 25 °C). The concentration of each solution is specified in each experiment. For the plasma generation, we incorporated a high voltage generator and a function generator into a pulser, which then sent the signal into a plasma jet.[21] In a plasma jet, a ballast resistance (500 Ω) was connected to a tungsten needle. That tungsten needle igniting plasma was also inserted into a quartz capillary tube with a 2 mm inner diameter and a 3mm outer diameter. The helium working gas with a flow rate of 3 standard liters per minute was used throughout this work. The needle-to-liquid distance was 15 mm. In our plasma pulse setting, the frequency was 1 kHz; namely, one single period is 1000 μs. The plasma on-time in the period was set as the pulse width, which is 20 μs. The grounding electrode was a graphite rod. The plasma-liquid interaction was allowed to react for 10 minutes. The current profiles were measured by a Rogowski coil

(Pearson 2877) and recorded with an oscilloscope (Tektronix DPO 2022B). The synthesized nanoparticles in EG were washed three times in water through centrifugation and redispersed in water after the final wash. The solution was then dried at 70 °C for further characterization. For the pulse-width-effect experiments, the total charge input was controlled by the reaction time. For the 40 μs pulse width, the reaction time was 5 minutes.

Scanning transmission electron microscopy (STEM) and energy dispersive X-ray spectroscopy (EDS) were performed on a TFS Talos F200X G2 operated at a 200 kV accelerating voltage. The bright-field images were processed by a filter to subtract the amorphous background signals.[22] The bright-field STEM line profiles were smoothed by the Savitzky-Golay algorithm[23] with a polynomial degree of 2. STEM samples were prepared by drop-casting the above-mentioned solution on a carbon-on-copper 300 mesh grid. Elemental mapping of the nanoparticles was generated using the Ag Lα and Pt M transition peaks. Besides, we overlapped the EDS element mapping data with the dark-field STEM image and converted the net EDS signals into a line scan to reveal the elemental composition and distribution of Ag and Pt. X-ray photoelectron spectra (XPS) were acquired using a Kratos Axis Ultra XPS with a monochromatic Al source. The measured binding energy was calibrated with respect to the adventitious carbon 1s peak at 284.6 eV. Regional Pt 4f and Ag 3d scans were acquired with a dwell time of 120 s using 20 and 90 sweeps, respectively. Peak fitting was performed using CasaXPS software. The composition was calculated using built-in relative sensitivity factors (RSF). Powder X-ray diffraction (XRD) data were acquired using a Rigaku Miniflex X-ray diffractometer with Cu−Kα X-ray source operated at 40 kV and 15 mA and a scan speed of 2° min^{-1}. The XRD data was smoothed by the Savitzky-Golay algorithm[23] with a polynomial degree of 2. Ultraviolet-visible (UV-vis) extinction spectra were acquired using a ThermoFisher

Scientific Evolution 300 spectrophotometer in transmission mode for colloidal solutions of nanoparticles. The UV-vis spectrum of $Ag_{0.2}Pt_{0.8}$-$NP_{(EG)}$ was measured after diluting the product solution 3.4 times with EG.

To reveal the onset reduction potentials of metal salt precursor solutions, we utilized a three-electrode rotating disk electrode (RDE) setup with Pt and glassy carbon (both 8 mm in diameter) as the working electrode materials and a clean Pt wire as the counter electrode. The potentials were measured with respect to a reference electrode. In aqueous solutions, the reference electrode was a mercury-mercury sulfate electrode ($Hg/HgSO_4$, $E_{Hg/HgSO4}$ = 650 mV vs NHE) to avoid the formation of $AgCl_{(s)}$. The conversion between a mercury-mercury sulfate electrode and an NHE is $E_{NHE} = E_{Hg/HgSO4} + 0.650$ V. While in EG solutions, the reference electrode was a silver-silver nitrate electrode ($Ag/AgNO_3$, $E_{Ag/AgNO3}$ = 541 mV vs NHE). The conversion between a silver-silver nitrate electrode and an NHE is $E_{NHE} = E_{Ag/AgNO3} + 0.541$ V. At the working electrode, linear sweep voltammetry was applied with a scan rate of 10 mV s^{-1}. The voltage was scanned from the upper potential limit to the lower potential limit. Electrochemical reactions occurred on the electrode surface as the voltage was applied, and the reaction rate was measured as the current. The disk rotating speed was 2500 rpm. The detailed procedures were reported elsewhere.[24-25] Besides, 100 mM potassium nitrate (KNO_3) was also added to the solution as a supporting electrolyte.

The temperature measurement was performed with FLIR One Pro LT iOS Pro-Grade Thermal Camera for Smartphones (Teledyne FLIR) throughout 10 minutes of plasma-liquid interactions. For the thermal reduction method, 3 ml of EG solution containing 0.1 mM $AgNO_3$ and 10 mM $Pt(NH_3)_4(NO_3)_2$ was heated to 160 °C for 10 minutes following the previously

reported preparation method.[26-27] The same cleaning procedure mentioned above was also carried out after cooling it to room temperature.

4.4 Results and Discussions

The sketch in Figure 4.1a shows the pulsed DC atmospheric-pressure plasma setup used in our study. The plasma was generated between a tungsten needle as a cathode and the surface of the solution as an anode. Our experiments were performed using two different solutions, an EG and an aqueous solution. The solutions interacted with pulsed DC plasma for 10 minutes under a fixed voltage of -2 kV. The plasma pulse duration was 20 μs, and it was applied to the solution at 1 kHz frequency, i.e., the plasma was on for 20 μs and off for 980 μs in a single period of 1000 μs. The data in Figures 4.1b and 4.1c show plasma-induced current profiles in the aqueous and EG solutions, respectively. The current profiles are very similar to each other, indicating that the solvents had little effect on the plasma discharge behavior.

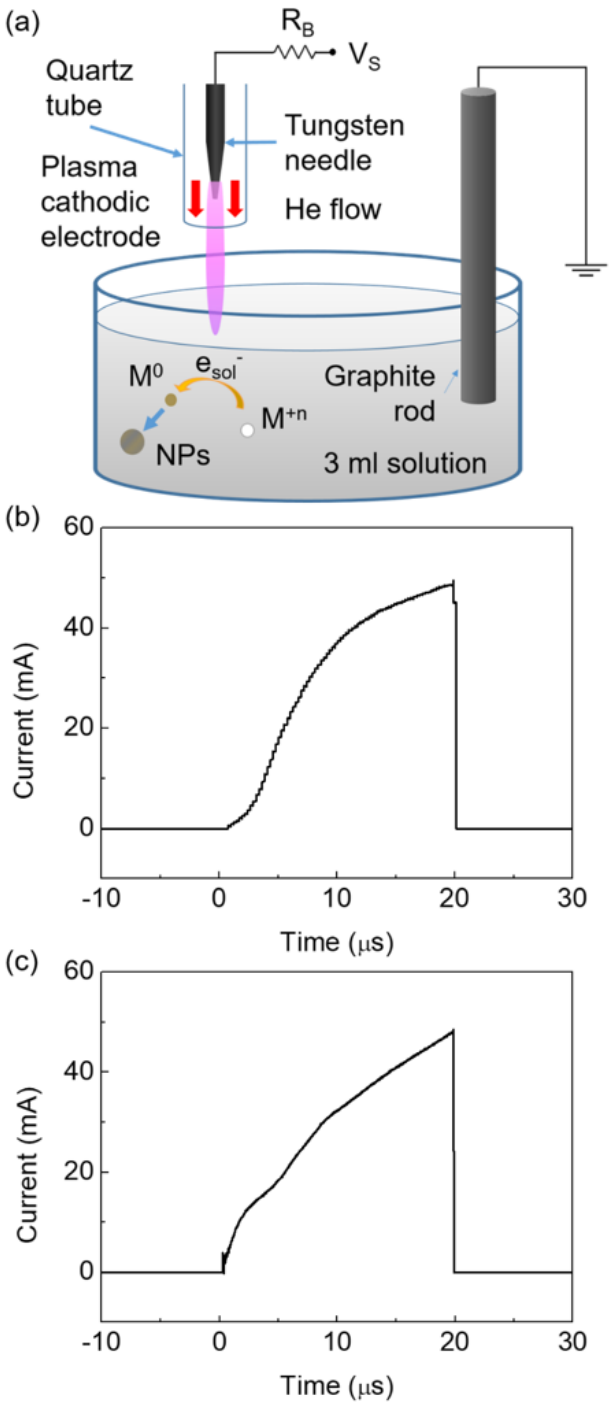


Figure 4.1 (a) Schematic of the pulsed DC plasma setup with applied voltage *Vs* and ballast resistance R_B. The M^{+n} metal ions are reduced to M^0 zerovalent atoms by the solvated electrons in the liquid. The current versus time for a single plasma pulse with a 20 μs pulse width while interacting with (b) aqueous and (c) EG solution, respectively. The fixed voltage is -2 kV, and the frequency is 1 kHz. Both solutions contain 0.1 mM $AgNO_3$ and 10 mM $Pt(NH_3)_4(NO_3)_2$.

We used $AgNO_3$ and $Pt(NH_3)_4(NO_3)_2$ as the Ag and Pt precursor salts, respectively. Instead of the commonly used Pt precursor, e.g., K_2PtCl_4[12] or K_2PtCl_6[28], where Pt ions are in the form of an anion, we chose $Pt(NH_3)_4(NO_3)_2$ to avoid the separation of the Ag and Pt precursor ions in the electrochemical plasma system due to their migration to the two different electrodes ($Pt(NH_3)_4^{2+}$ and Ag^+ are both cations), as well as to prevent the formation of $AgCl_{(s)}$. As the standard reduction potential of Ag^+ is more positive than that of $Pt(NH_3)_4^{2+}$ in aqueous solution, in our synthesis, we used 0.1 mM $AgNO_3$ and 10 mM $Pt(NH_3)_4(NO_3)_2$ to decrease the gaps in the reduction potentials.[2, 29] We also monitored the temperature of the solution with an infrared camera and found a limited temperature increase relative to the room temperature, i.e., the temperature increased from 25.2 °C (Figure 4.2a) to 47.6 °C (Figure 4.2b) with negligible fluctuations during the 10-minute plasma interactions. The negligible change of UV-vis extinction spectra indicates that no spontaneous reduction reactions are observed after heating the solution to both 25°C and 48°C for 10 minutes (Figure 4.3).

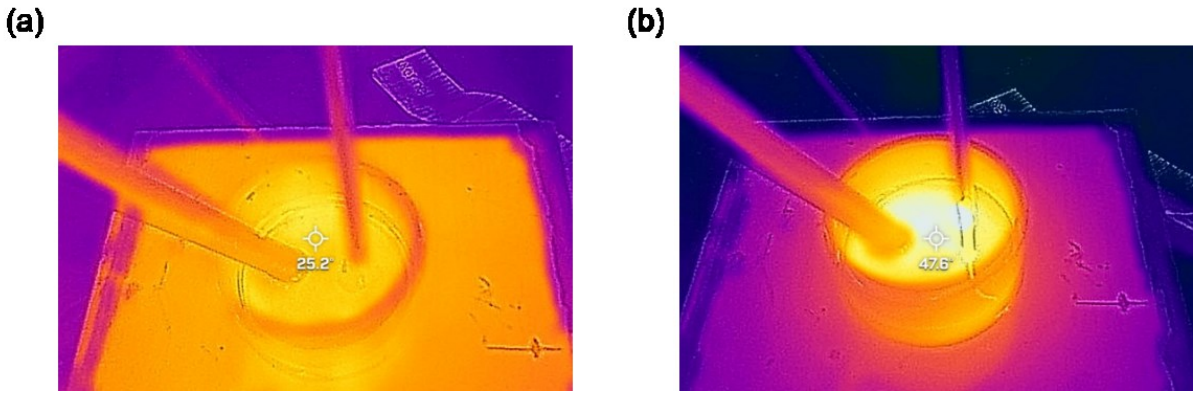


Figure 4.2 Infrared-measured temperature distribution of the EG solution containing 0.1 mM $AgNO_3$ and 10 mM $Pt(NH_3)_4(NO_3)_2$ is shown in (a) before plasma-liquid interactions and (b) after ten minutes of plasma-liquid interaction when the temperature reached equilibrium.

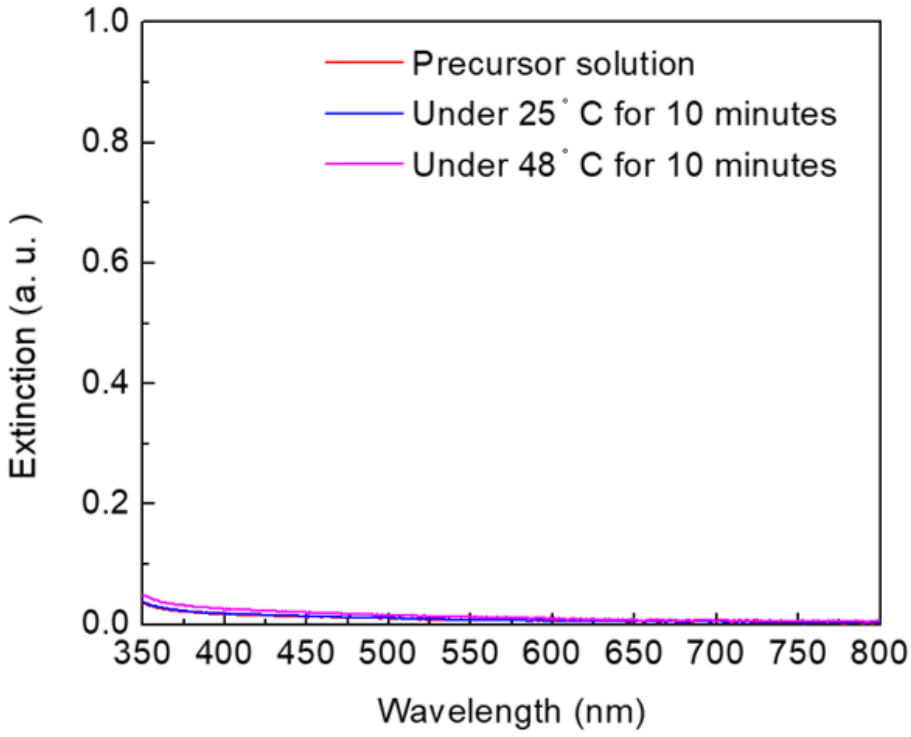


Figure 4.3 Ultraviolet-visible extinction spectra of the precursor solution (0.1 mM $AgNO_3$ and 10 mM $Pt(NH_3)_4(NO_3)_2$ in EG solution) at room temperature and after heating the precursor solution to 25°C and 48°C for 10 minutes. The negligible changes in the UV-vis extinction spectra indicate that no spontaneous reduction reaction occurs at 25°C and 48°C.

The nanoparticles, synthesized in the two solvents, were characterized using STEM and EDS. The image in Figure 4.4a shows that nanoparticles synthesized in the EG solution had a diameter of approximately 10 nm. The elemental mapping data obtained using EDS in Figure 4.4b show that both Pt and Ag atoms were uniformly distributed in individual nanoparticles. The EDS line scan (Figure 4.4c) further illustrates a homogeneous structure with the Pt-to-Ag atomic ratio of about 80% to 20%. These nanoparticles are denoted as $Ag_{0.2}Pt_{0.8}$-$NP_{(EG)}$. Further characterizations, including the UV-vis extinction spectrum and the nanoparticle size distribution of $Ag_{0.2}Pt_{0.8}$-$NP_{(EG)}$, are also measured. The UV-vis extinction spectrum of the $Ag_{0.2}Pt_{0.8}$-$NP_{(EG)}$ in Figure 4.5a does not show a plasmonic peak in the range of visible light as the main constituent metal is Pt.[30] The data in Figure 4.5b illustrate the average size of the $Ag_{0.2}Pt_{0.8}$-

$NP_{(EG)}$ to be 10.5 ± 2.0 nm. We also compared the Ag-Pt nanoparticles synthesized using plasma pulses in the EG solution ($Ag_{0.2}Pt_{0.8}$-$NP_{(EG)}$) with the nanoparticles synthesized under the same conditions in the aqueous solution of the identical precursors. The image in Figure 4.4d shows that the nanoparticles formed in the aqueous solution aggregated and formed a structure with an average diameter of 206.3 ± 20.5 nm. The elemental EDS mapping data in Figure 4.4e show that the structure is mainly composed of Ag with a very small amount of Pt. The EDS line scan (Figure 4.4f) confirms this observation, showing strong Ag signals and negligible Pt signals throughout the structure.

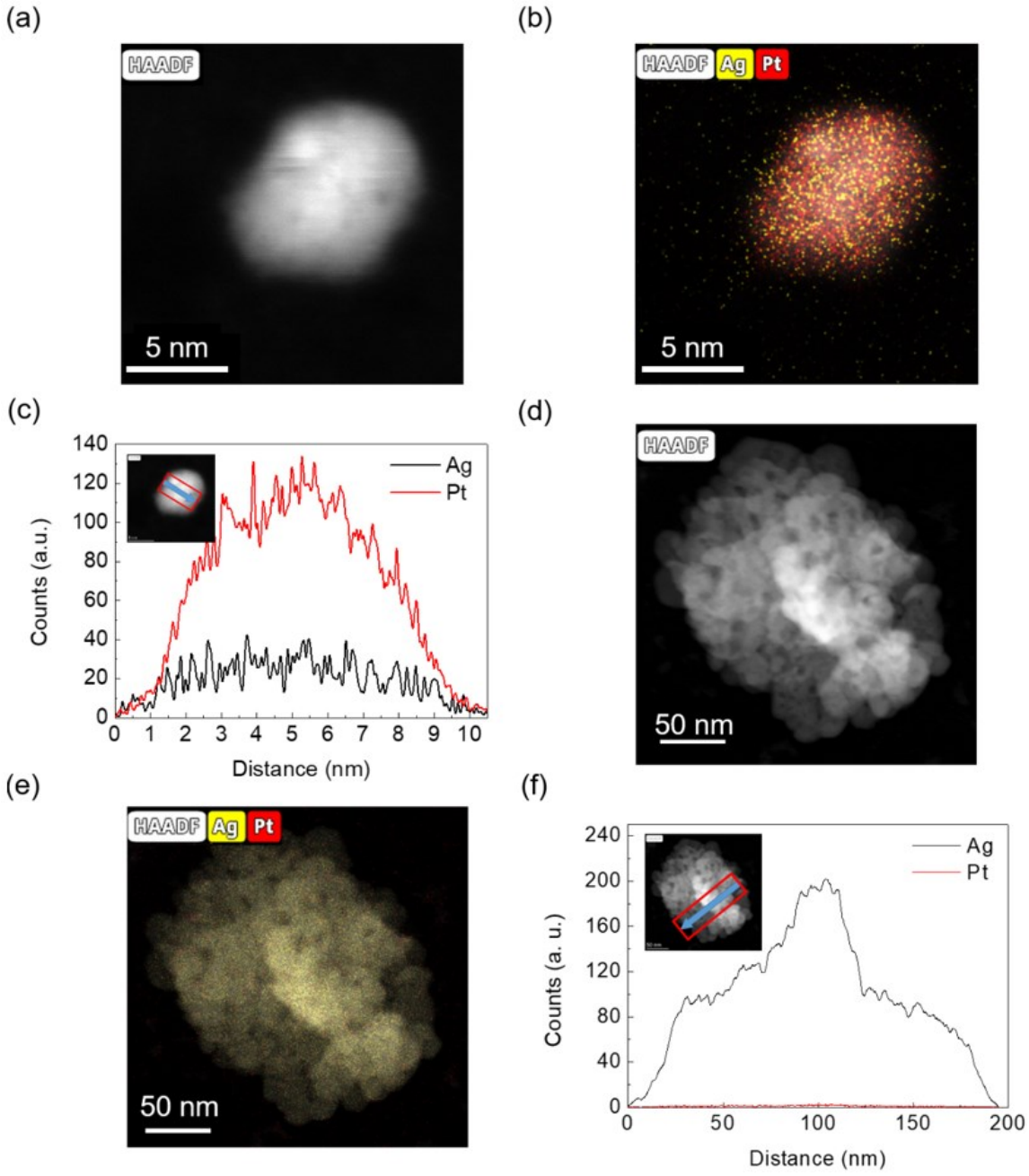


Figure 4.4 (a) The dark-field STEM image, (b) overlapping Ag and Pt EDS mapping data with the STEM image, and (c) EDS line scan of the Ag and Pt net signals of $Ag_{0.2}Pt_{0.8}$-$NP_{(EG)}$ synthesized in EG. (d) The dark-field STEM image, (e) overlapping Ag and Pt EDS mapping data with the STEM image, and (f) EDS line scan of the Ag and Pt net signals of a nanoparticle synthesized in aqueous solution. The dark-field STEM images were acquired by the high-angle annular dark-field detector (HAADF).

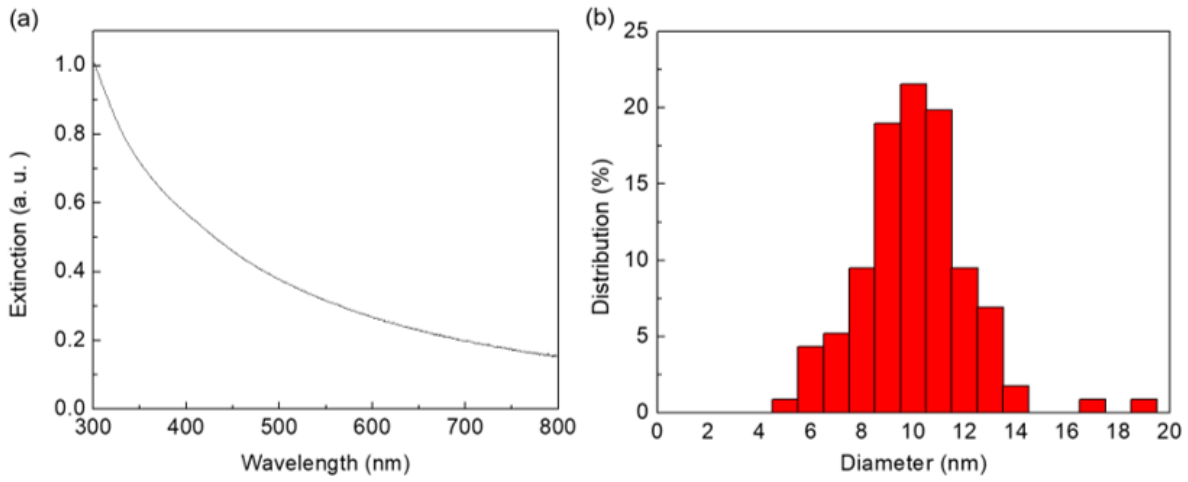


Figure 4.5 (a) UV-vis extinction spectrum of $Ag_{0.2}Pt_{0.8}$-$NP_{(EG)}$ in EG solution. (b) Size distribution of $Ag_{0.2}Pt_{0.8}$-$NP_{(EG)}$. The average nanoparticle size is 10.5 ± 2.0 nm.

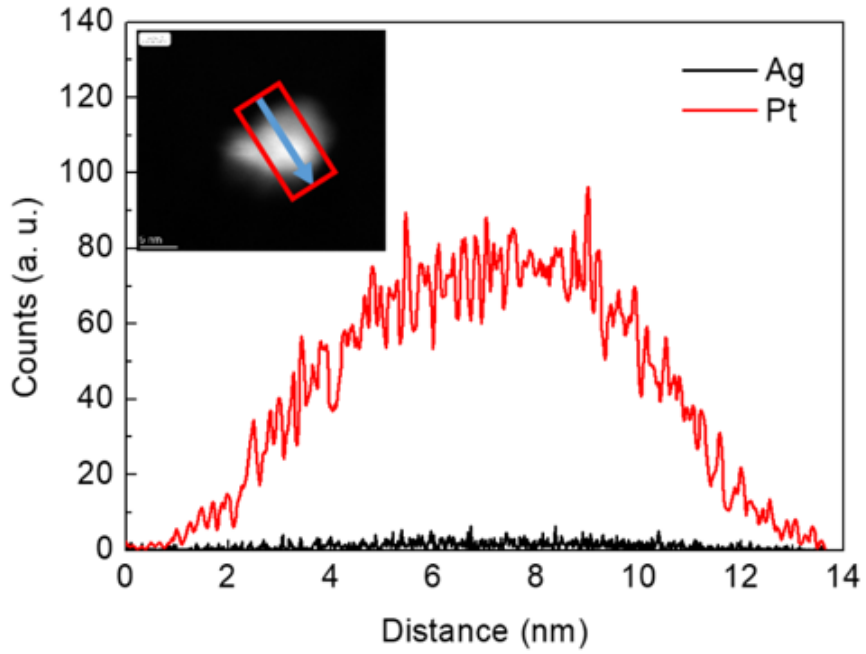


Figure 4.6 EDS line scan of Pt-$NP_{(EG)}$ exhibits Ag and Pt signals. Ag signals are negligible, confirming it as a Pt monometallic nanoparticle.

To further establish that there is a mixing of Pt and Ag atoms in $Ag_{0.2}Pt_{0.8}$-$NP_{(EG)}$, we performed XPS and XRD on the alloy nanoparticles and compared the data to those obtained for

the monometallic Pt-$NP_{(EG)}$ nanoparticles. Monometallic nanoparticles of Pt were synthesized by applying the same plasma condition to the 10 mM $Pt(NH_3)_4(NO_3)_2$ EG solution. The dark-field STEM image and EDS line scan of these Pt-$NP_{(EG)}$ nanoparticles in Figure 4.6 indicate that the nanoparticles have a diameter of approximately 12 nm. The Pt 4f core level XPS spectrum of Pt-$NP_{(EG)}$ displays peak positions at 71.3 eV ($4f_{7/2}$) and 74.5 eV ($4f_{5/2}$), corresponding to the metallic Pt^0 state.[31-32] On the other hand, the XPS data in Figure 4.7a show that compared to the Pt 4f core level XPS spectrum measured for Pt-$NP_{(EG)}$, the Pt 4f core level in $Ag_{0.2}Pt_{0.8}$-$NP_{(EG)}$ is shifted by -0.3 eV in the direction of lower binding energy. The observed shift from the data is consistent in its direction and magnitude with previous theoretical and experimental results, showing the atomic mixing of Pt and Ag that should yield the shifts in the Pt core electronic states.[33-34]

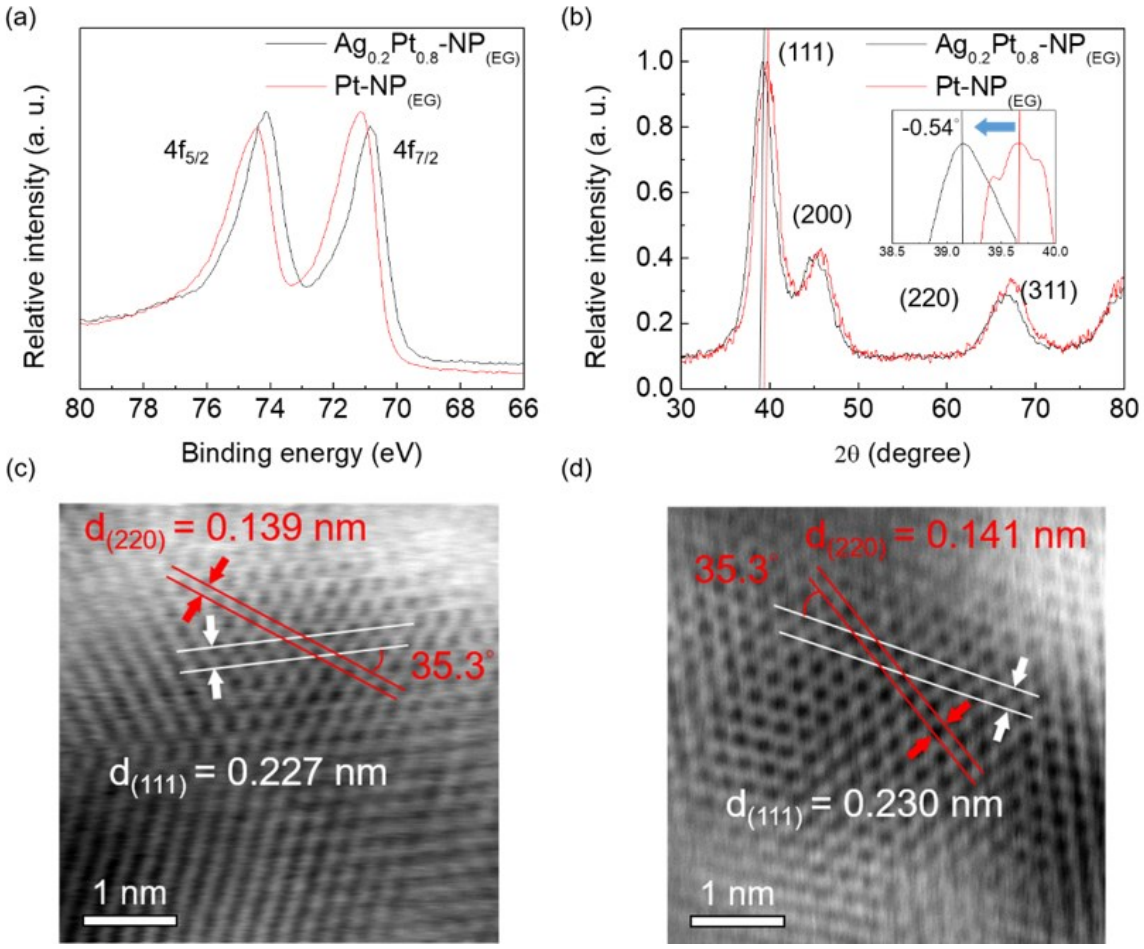


Figure 4.7 (a) The Pt 4f XPS core scan comparison between $Ag_{0.2}Pt_{0.8}$-$NP_{(EG)}$ and Pt-$NP_{(EG)}$, a shift is clearly shown. (b) The XRD pattern comparison between $Ag_{0.2}Pt_{0.8}$-$NP_{(EG)}$ and Pt-$NP_{(EG)}$. The peak position of the $Ag_{0.2}Pt_{0.8}$-$NP_{(EG)}$ (111) facet shifts to the one of the Ag (111) facet. (c) The bright-field STEM image of Pt-$NP_{(EG)}$ along with its lattice structure of a cubic structure. (d) The bright-field STEM image of $Ag_{0.2}Pt_{0.8}$-$NP_{(EG)}$ along with its lattice structure of a cubic structure. The reported lattice constants were measured with a pixel size of 0.718 pm.

We also measured the XRD spectra of the $Ag_{0.2}Pt_{0.8}$-$NP_{(EG)}$ and Pt-$NP_{(EG)}$ nanoparticles. The data in Figure 4.7b show that the Pt-$NP_{(EG)}$ exhibits the XRD spectra consistent with the spectra reported for monometallic Pt crystallites of the face-centered cubic structure (PDF Number: 1-1190).[35] On the other hand, the XRD spectrum measured for the $Ag_{0.2}Pt_{0.8}$-$NP_{(EG)}$ nanoparticles shows changes in the diffraction patterns that are suggestive of a slight increase in the lattice constant of the alloy compared to monometallic Pt nanoparticles. These changes are consistent with the fact that the atomic diameter of Ag is slightly larger compared to Pt,

therefore, leading to an increase in the lattice constant for the alloy structures.[36] The lattice constant shift was also further confirmed by the high resolution bright-field STEM images of Pt-$NP_{(EG)}$ (Figure 4.7c) and $Ag_{0.2}Pt_{0.8}$-$NP_{(EG)}$ (Figure 4.7d). The lattice constants for the (111) and (220) facets of Pt-$NP_{(EG)}$ were measured to be 0.227 nm and 0.139 nm, respectively, which is consistent with monometallic Pt (PDF Number: 1-1190).[35] On the other hand, the lattice constants for the same (111) and (220) facets of $Ag_{0.2}Pt_{0.8}$-$NP_{(EG)}$ were measured to be 0.230 nm and 0.141 nm, respectively. The data are consistent with the XRD data discussed above, which showed an increase in the lattice constant for the alloys compared to monometallic Pt nanoparticles. We also note that the measured lattice constant for the alloy is smaller than the lattice constant for monometallic Ag crystallites (PDF Number: 1-1164).[37]

Collectively, the data in Figures 4.4 and 4.7 show that under the conditions of pulsed plasma, it is possible to synthesize an alloy of Ag and Pt in the form of relatively small nanoparticles in EG solution. On the other hand, under identical conditions, in aqueous solution, the plasma-induced reduction process resulted in a negligible mixing of Ag and Pt. We hypothesized that the nature of the solution (water versus EG) affects the reduction potentials of the two precursors and that in EG the difference in the reduction potentials for the Ag and Pt salts is lower than in water. As a zero-order approximation, metal ions with more positive reduction potentials tend to have faster reduction rates.[2] That is, if the reduction potential difference is smaller, the reduction rates of the metal ions would be more comparable, which can lead to the formation of a kinetically stable alloy state that traps the immiscible metal atoms. Here, we assume that the reduction reaction rate can be estimated by the measured onset reduction potential, and the formation of alloys will benefit from similar reduction reaction rates of the two different precursors. This lower reduction potential difference would presumably

result in more even reduction rates that allow for the immiscible metal atoms to be trapped in the kinetically stable alloy state.

To test the hypothesis, we measured the onset reduction potentials of reduction reactions for the two different precursor salts in EG and aqueous solutions by performing linear sweep voltammetry on a rotating disk electrode.[24-25] The rotating disk electrode setup ensures that a boundary layer with a fixed concentration gradient on the electrode surface is maintained due to the introduction of convection, i.e., the resistance due to the mass transport of salt molecules to the electrode surface does not govern the outcome in the low overpotential regions (close to the onset reduction potential). This allows us to rigorously measure the potentials associated with the kinetic reduction. The current profile (as the function of the voltage applied to the electrode) is therefore divided into reaction-controlled (low overpotential) and mass-transfer-controlled (high overpotential) regions.[38] In the reaction-controlled region, the current as a function of applied potential can be reasonably well described by the Tafel equation, $E - E_{red} = A \log(\frac{i}{i_0})$, where E is the applied potential, E_{red} is the onset reduction potential, A is the Tafel slope, i is the current, and i_0 is the exchange current.[38] At the onset reduction potential of the reduction reaction ($E = E_{red}$), the current begins to increase exponentially as the applied potential increases. Therefore, we took the logarithm (log) of the current (i) and plotted it versus the applied potential (E) to identify the linear region. The starting potential of the linear region is reported as the onset reduction potential (E_{red}) under the specific set of conditions. The onset reduction potential reflects the tendency of a reduction reaction to take place.[25]

We measured E_{red}, using a glassy carbon electrode, for the $AgNO_3$ solution from 0.1 mM to 40 mM salt concentrations, and the $Pt(NH_3)_4(NO_3)_2$ solution from 10 mM to 100 mM salt concentrations. The measured current versus applied potential profiles are plotted in Figures 4.8

and 4.9. The data in Figure 4.10 show the measured onset reduction potentials as the function of the metal salt precursor concentrations following the Nernstian behavior in both solutions. The Nernst equation is given by: $E_{red} = E^0 - 2.303 \frac{RT}{nF} \log (Q)$, where E_{red} is the onset reduction potential, E_0 is the standard onset reduction potential, R is the gas constant, T is the absolute temperature, n is the number of electrons transferred, F is the Faraday constant, and log (Q) is the logarithm of the reaction quotient.

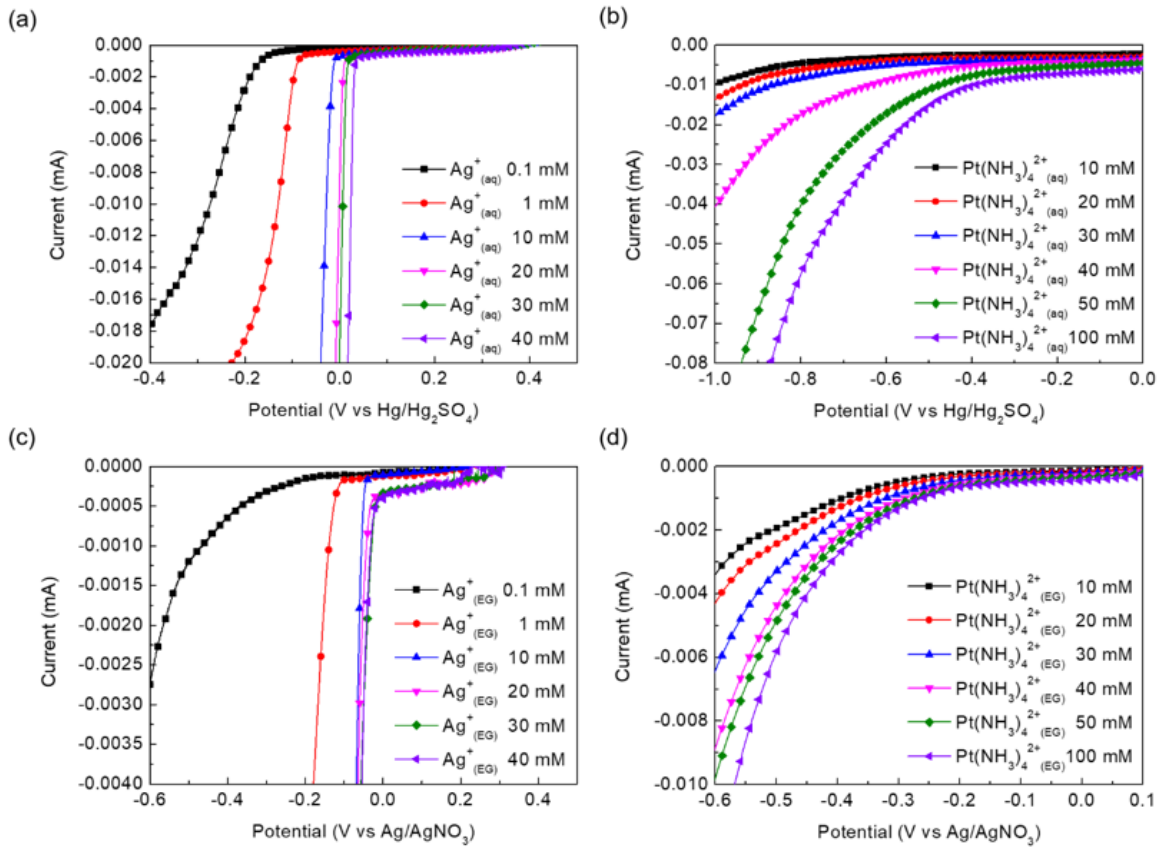


Figure 4.8 Current versus potential profiles from linear sweep voltammetry are shown for (a) silver precursor in aqueous solution, (b) platinum precursor in aqueous solution, (c) silver precursor in ethylene glycol solution, and (d) platinum precursor in ethylene glycol solution.

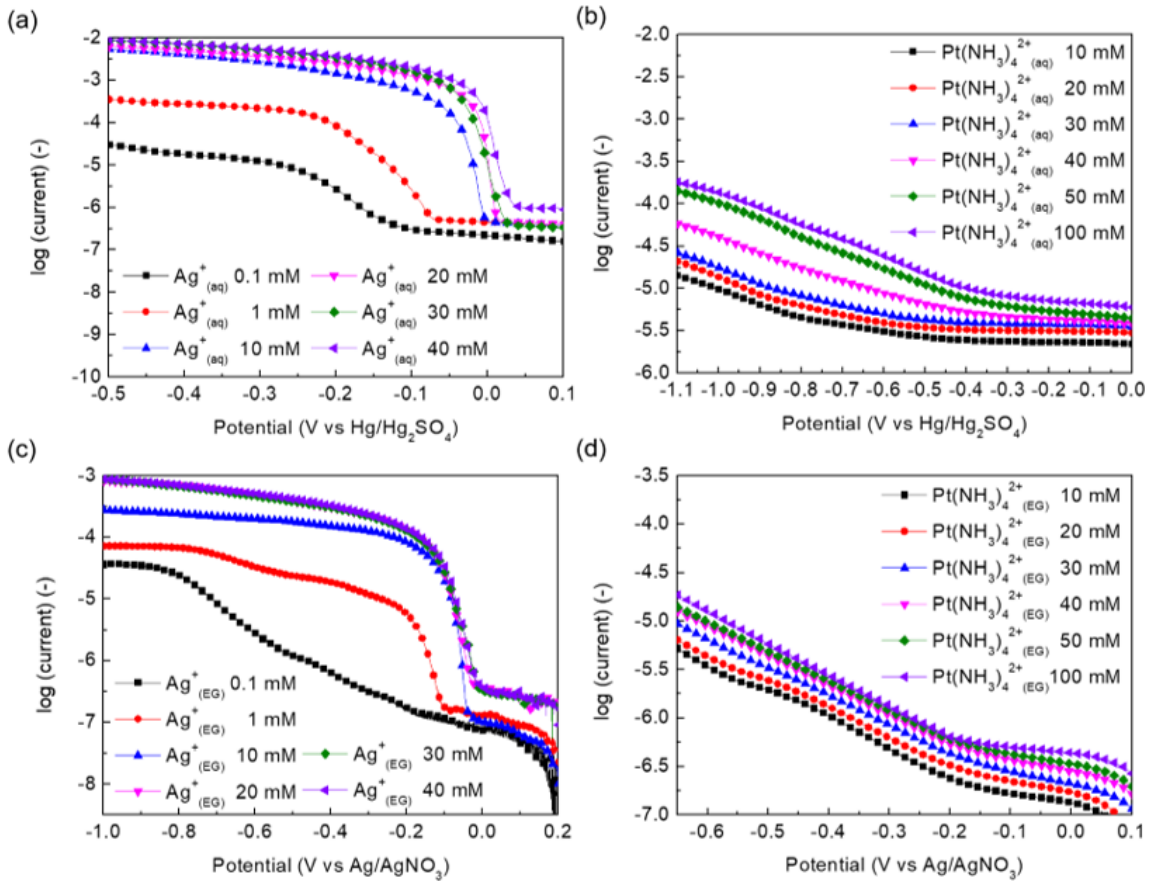


Figure 4.9 Logarithm of current versus potential profiles from linear sweep voltammetry are shown for (a) silver precursor in aqueous solution, (b) platinum precursor in aqueous solution, (c) silver precursor in ethylene glycol solution, and (d) platinum precursor in ethylene glycol solution. Each condition contains six different concentrations.

The data in Figure 4.10a show that in aqueous solution the onset reduction potential of 10 mM $Pt(NH_3)_4(NO_3)_2$ was measured to be 180 mV versus NHE, while the onset reduction potential of 0.1 mM $AgNO_3$ was 520 mV (versus NHE). The measured 340 mV difference between the onset reduction potential of the two metal salt precursors is very large, indicating that it is almost impossible to reduce these precursors at similar reduction rates in this environment. In contrast to the aqueous solution case, in the EG solution (Figure 4.10b), the onset reduction potential of 0.1 mM $AgNO_3$ was measured to be 322 mV versus NHE, which is relatively close to that of 10 mM $Pt(NH_3)_4(NO_3)_2$, which was measured to be 326 mV versus

NHE. These measured onset reduction potentials suggest that for the two precursors, these potentials should be relatively comparable for alloy formation to take place.

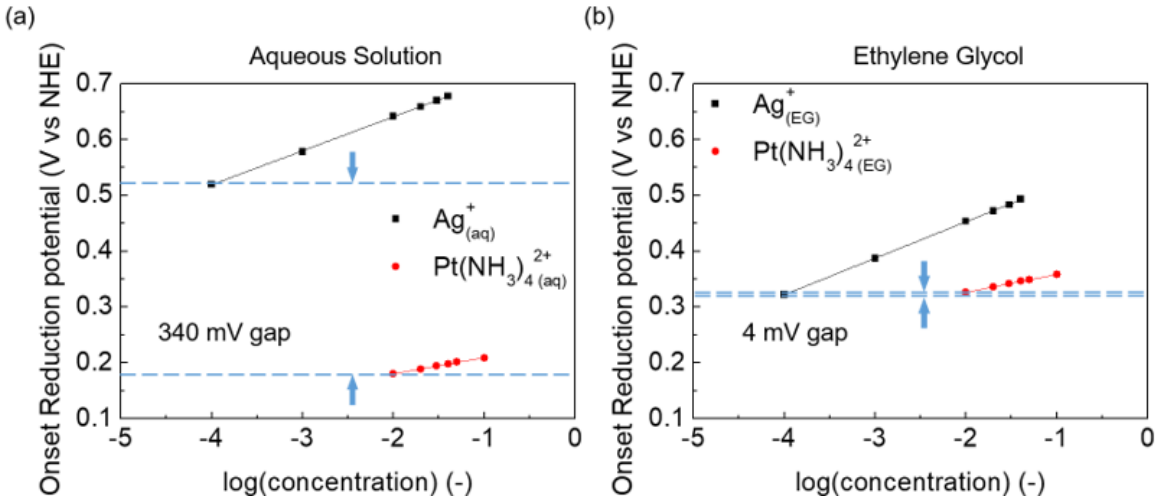


Figure 4.10 The onset reduction potential versus the log of the concentration of Ag (Ag^+) and Pt ($Pt(NH_3)_4^{2+}$) precursor in (a) aqueous solution and (b) EG solution. A 340 mV onset reduction potential gap is observed between two metal salt precursors in aqueous solution (0.1 mM Ag^+: 520 mV; 10 mM $Pt(NH_3)_4^{2+}$: 180 mV), while a negligible difference is found in EG solution (0.1 mM Ag^+: 322 mV; 10 mM $Pt(NH_3)_4^{2+}$: 326 mV).

The onset reduction potential shifts of the metal salt precursors in EG compared to water may result from the interactions between the solvent and the metal salt precursor. The solvent molecules stabilize the metal ions, acting as electron donors and partially replacing the coordination sites on the metal ions due to the large excess number of solvent molecules over the ligand molecules. These interactions shift the reduction potentials of the metal precursors with varying directions and magnitudes between different solvents.[39-40] In our case, as the onset reduction potential of Ag^+ is negatively shifted and the onset reduction potential of $Pt(NH_3)_4^{2+}$ is positively shifted in the EG solution, the onset reduction potential gap between the two precursors therefore decreases. It allows us to match the onset reduction potentials in EG, resulting in the formation of alloy nanoparticles.

In addition to the relatively similar reduction rates between the two metal salts, other critical variables that can affect the process of nanoparticle synthesis are nucleation and growth. The nucleation of Ag nanoparticles is known to be governed by the LaMer mechanism[41], while that of Pt is governed by the Finke-Watzky mechanism[42]. The LaMer mechanism involves three stages: (i) the rapid increase in the concentration of free metal atom monomers, (ii) the "burst-nucleation" of the monomers to form clusters after the monomer concentration exceeds the nucleation threshold concentration, and (iii) the growth by diffusion and attachment.[43] The Finke-Watzky mechanism includes two stages: slow nucleation without a required threshold concentration for nucleation and autocatalytic surface-mediated growth.[43] Based on the above nucleation and growth mechanisms, we hypothesized that when it comes to Ag-Pt bimetallic synthesis, if the Ag atom concentration exceeds the nucleation threshold concentration, Ag atoms will nucleate rapidly and form Ag clusters. The attachment of the Ag clusters to each other will lead to a preferential formation of segregated Ag monometallic nanoparticles rather than the formation of Ag-Pt bimetallic nanoparticles. Therefore, to avoid the formation of Ag monometallic nanoparticles and form only bimetallic alloy nanoparticles, it is necessary to avoid exceeding the nucleation threshold concentration of Ag atoms in the Ag-Pt mixed precursor solutions.

To test this hypothesis, we manipulated the concentrations of the Ag and Pt precursors and measured how it impacts the outcome of the synthesis process. In one experiment, instead of the above-discussed conditions where 0.1 mM $AgNO_3$ and 10 mM $Pt(NH_3)_4(NO_3)_2$ EG solutions were used, we increased the concentration of the metal salt precursors in EG to 0.36 mM $AgNO_3$ and 100 mM $Pt(NH_3)_4(NO_3)_2$. At these higher concentration conditions, both precursors in EG have an onset reduction potential of ~358 mV (vs NHE). Under these high concentration

conditions, we anticipated a potential nucleation of the Ag clusters, leading to the formation of Ag monometallic nanoparticles. In another experiment, we decreased the concentrations of the precursors to 0.078 mM $AgNO_3$ and 3 mM $Pt(NH_3)_4(NO_3)_2$, keeping the same reduction potential of both precursors at ~311 mV (vs NHE). Under the same plasma setting, the induced current profiles of the three conditions (Figure 4.11a) show a negligible difference, indicating that the plasma discharge behavior was not significantly affected by changing the precursor concentrations.

The nanoparticles synthesized under these conditions were characterized by STEM and EDS. The dark-field STEM image of the nanoparticles synthesized for the (0.36 mM $AgNO_3$ and 100 mM $Pt(NH_3)_4(NO_3)_2$) solution is shown in Figure 4.11b. The EDS mapping in Figure 4.11c shows that two types of nanoparticles with different atomic ratios were formed, including Ag monometallic nanoparticles with less than 1% Pt signals (Figure 4.11d) and a porous Ag-Pt alloy nanoparticle (Figure 4.11e) with Pt to Ag atomic ratio of 80% to 20%. These results suggest that as the concentration of the precursor increased, not only Ag-Pt alloy nanoparticles were formed but also monometallic Ag nanoparticles.

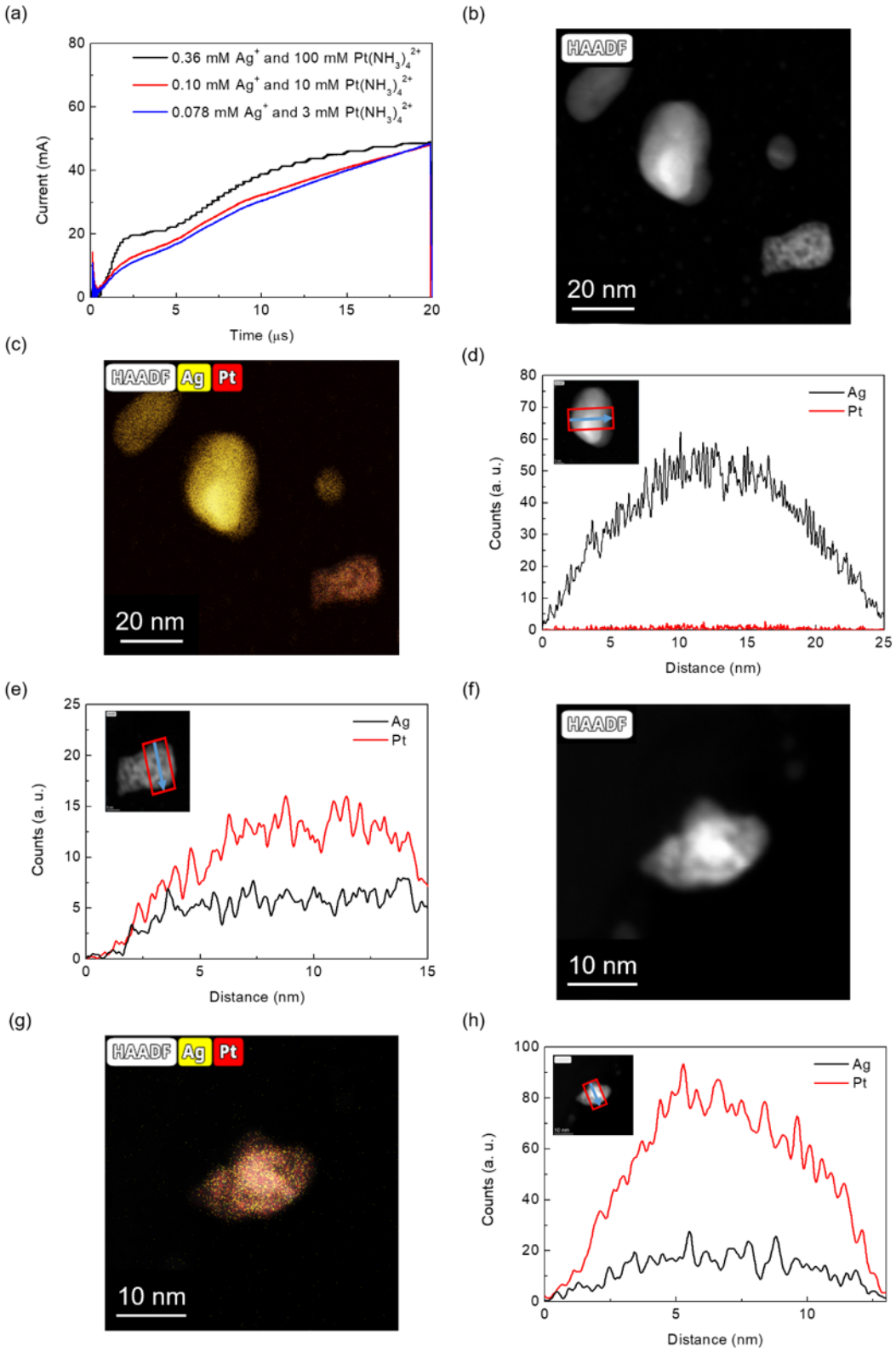


Figure 4.11 (a) The current profile of the three concentration conditions with matched reduction potentials. The current profiles show negligible differences. (b) The dark-field STEM image and (c) overlapping Ag and Pt EDS mapping data with the STEM image of nanoparticles synthesized in ethylene glycol solution containing 0.36 mM

$AgNO_3$ and 100 mM $Pt(NH_3)_4(NO_3)_2$. (d) The corresponding EDS line scan of the nanoparticle in the middle with only Ag signals. (e) The corresponding EDS line scan of the nanoparticles in the bottom-right with both Pt and Ag signals. (f) The dark-field STEM image and (g) overlapping Ag and Pt EDS mapping data with the STEM image of a nanoparticle synthesized in ethylene glycol solution containing 0.078 mM $AgNO_3$ and 3 mM $Pt(NH_3)_4(NO_3)_2$. (h) The corresponding EDS line scan of the nanoparticle with both Ag and Pt signals.

To further reveal the formation of the porous structure, we did a thorough EDS mapping of one of the alloy nanoparticles (Figures 4.12 a and b). In Figure 4.12c, the pore is located at about 2.5 nm with a dramatic HAADF signal decrease. At the same position, we observed a decline in Ag signals and relatively stable Pt signals, which implies that the formation of pores is attributed to the etching of Ag atoms on the surface. We hypothesize that the etching is probably due to NH_3, the ligand of the Pt precursor. The etching by NH_3 with other oxidative agents and its ability to change the morphology were previously reported.[44] As the etching effect was only observed under this condition, we assume that it may result from the increased reduction reaction rate of Pt precursors (as the reduction potential increased) that released more NH_3 compared to other conditions.

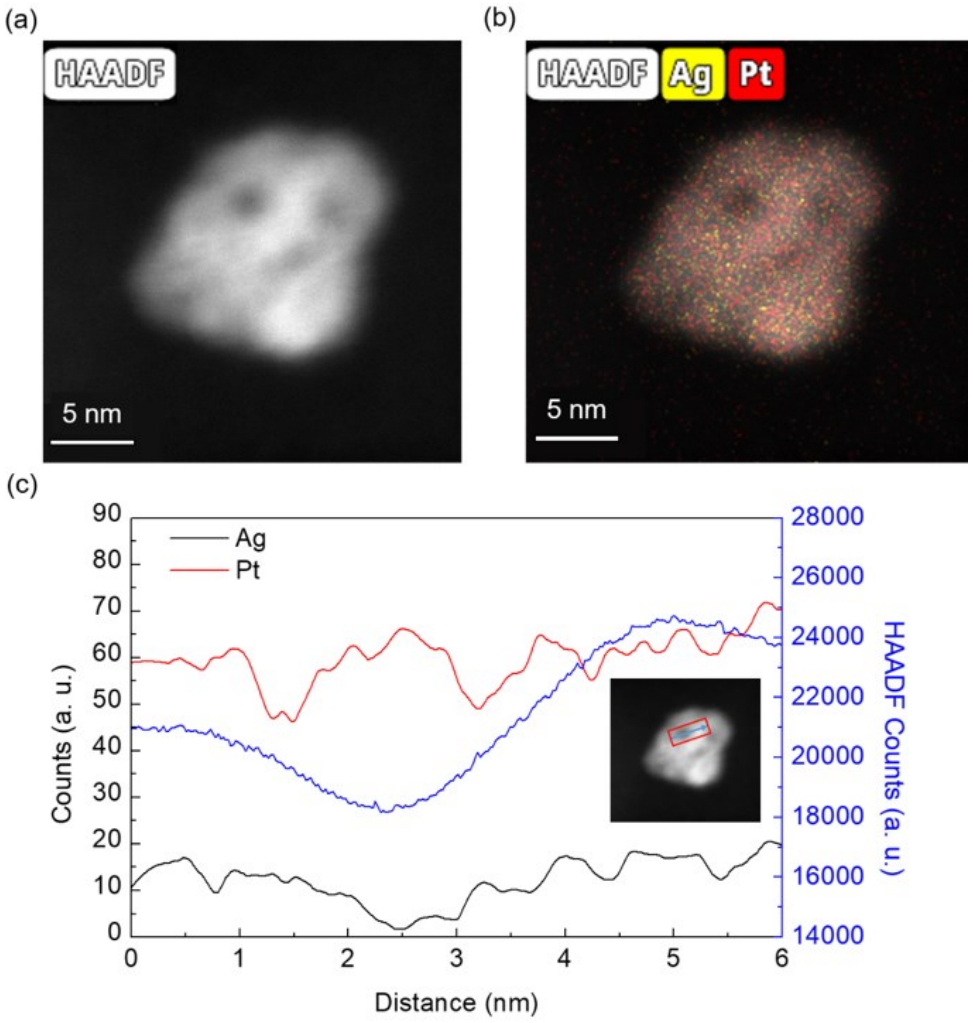


Figure 4.12 (a) Dark-field STEM image and (b) overlapping Ag and Pt EDS mapping data with the STEM image of a nanoparticle synthesized in ethylene glycol solution containing 0.36 mM $AgNO_3$ and 100 mM $Pt(NH_3)_4(NO_3)_2$. (c) EDS line scan of the net Ag, net Pt, and high-angle annular dark-field detector (HAADF) signals. The line scan focused on a pore and indicated a decrease in Ag signals.

On the other hand, the experiments conducted at lower precursor concentrations (0.078 mM $AgNO_3$ and 3 mM $Pt(NH_3)_4(NO_3)_2$) showed that the synthesized nanoparticles (Figure 4.11f) were almost exclusively the $Ag_{0.2}Pt_{0.8}$-$NP_{(EG)}$ alloy nanoparticles. This is demonstrated by the EDS data and dark-field STEM image (Figure 4.11g) that show uniformly distributed Pt and Ag signals in a single nanostructure. The EDS line scan in Figure 4.11h indicates a Pt to Ag atomic ratio of 80% to 20%. Low-magnification STEM images and EDS mappings of multiple

nanoparticles are illustrated in Figure 4.13. The result suggests that in our reaction condition, if the Ag precursor concentration exceeds a certain value (between 0.1 and 0.3 mM), the resulting concentration of Ag monomers may surpass the nucleation threshold concentration, which leads to the formation of Ag monometallic nanoparticles.

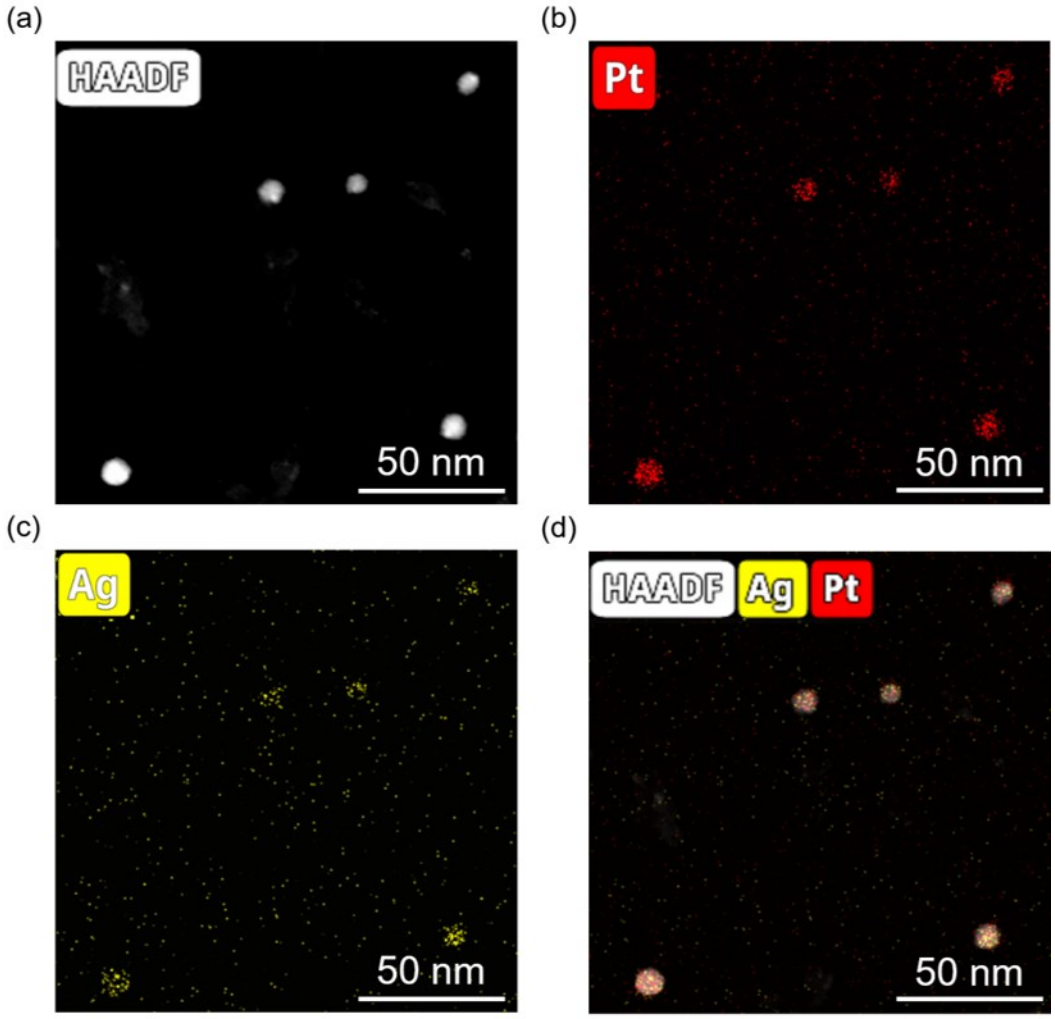


Figure 4.13 (a) Low-magnification dark-field STEM image, (b) EDS Pt mapping data, (c) EDS Ag mapping data, and (d) overlapping Ag and Pt EDS mapping data with the STEM image of the nanoparticles synthesized in ethylene glycol solution containing 0.078 mM $AgNO_3$ and 3 mM $Pt(NH_3)_4(NO_3)_2$.

The data above demonstrated that low metal precursor concentrations and the relatively equal reduction potentials seem to be required prerequisites for ensuring that only the alloy nanoparticles are formed. It is critical to analyze how and why these prerequisites yield alloy nanoparticles under pulsed plasma reduction conditions, while the alloys are not formed under different reduction conditions. Our hypothesis is that in the case of pulsed plasma, when the pulse is on, electrons are rapidly transferred to the liquid phase, reducing the metal salts to atoms (e.g., Ag atoms are formed). When the pulse is off, without electrons, the reduction process is stopped, and the Ag atom concentration stops increasing. Similar effects of pulsed or continuous current on the nucleation process in electroplating have been discussed previously.[45] This is fundamentally different from thermal reduction (or most other reduction processes) where the timescales associated with heating and cooling are significantly longer and do not allow for a high degree of control over the reduction process.

To test the hypothesis, we analyzed the effect of the pulse width on the same EG solution containing 0.1 mM $AgNO_3$ and 10 mM $Pt(NH_3)_4(NO_3)_2$. In these experiments, we used a 40 μs pulse width instead of the 20 μs pulse width discussed earlier, while ensuring that the total charge input remained identical by adjusting the reaction time. We hypothesized that using a short pulse width would prevent the local concentration of Ag atoms from reaching the nucleation threshold concentration, while a longer pulse might exceed the nucleation threshold. The current profiles for the 20 and 40 μs pulse widths are plotted in Figure 4.14a. For the plasma pulse width of 40 μs, two types of nanoparticles were formed (Figure 4.14b). The EDS line scans show that the larger nanoparticle (Figure 4.14d) was an Ag monometallic nanoparticle, while the smaller nanoparticle was an alloy nanoparticle of Ag and Pt (Figure 4.14e). These results suggest that the rapid plasma-induced reduction reaction is necessary for the formation of alloy

nanoparticles, but the local concentration of monomers must be kept low enough to prevent reaching the nucleation threshold concentration. We show that pulsed plasma allows for a high degree of control over these local processes.

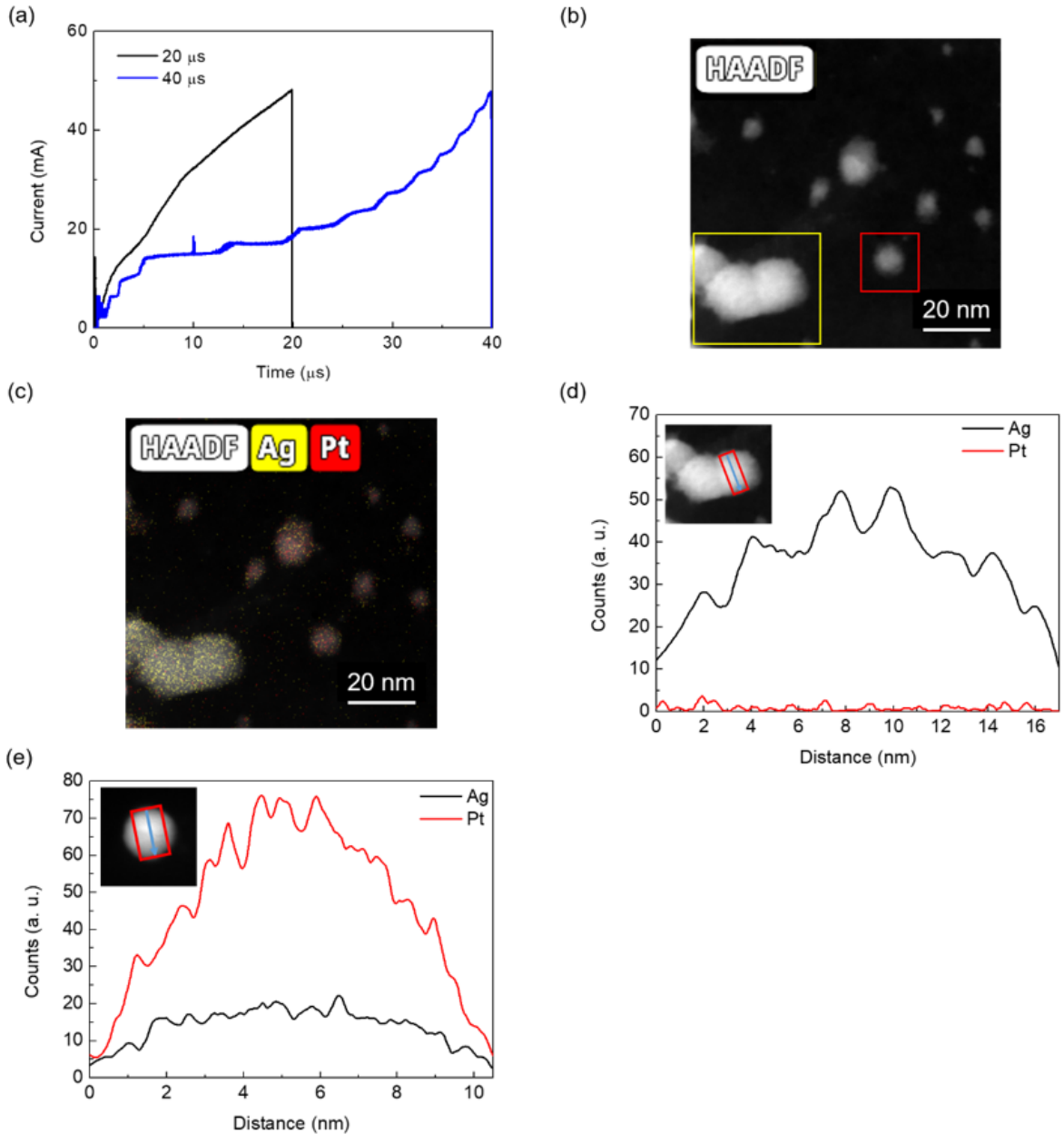


Figure 4.14 (a) Current profiles of plasma discharge with 20 μs and 40 μs pulse width in the ethylene glycol solution containing 0.1 mM $AgNO_3$ and 10 mM $Pt(NH_3)_4(NO_3)_2$. (b) Dark-field STEM image and (c) overlapping Ag and Pt EDS mapping data with the STEM image of the samples synthesized with a 40 μs pulse width. (d) EDS line scan of the nanoparticle marked with a yellow rectangle on the bottom left of (b) with mainly Ag signals. (e) EDS line scan

of the nanoparticle marked with a red square of (b) with both Ag and Pt signals. The Pt-to-Ag atomic ratio is about 80 to 20%.

Moreover, this hypothesis was further tested as we compared the nanoparticles synthesized using the pulsed plasma-liquid interactions ($Ag_{0.2}Pt_{0.8}$-$NP_{(EG)}$) to those synthesized using a thermal reduction of the same EG solution. In these thermal experiments, the EG solution containing 0.1 mM $AgNO_3$ and 10 mM $Pt(NH_3)_4(NO_3)_2$ was heated to 160 °C, which was sufficient to reduce the two metal salts.[26-27] The STEM images and elemental EDS line scans of the nanoparticles (Figures 4.15a-h) showed that the samples contained segregated Ag and Pt monometallic nanoparticles. That is, there were no bimetallic nanoparticles formed using the thermal reduction method. These results consistently demonstrate the advantages provided by the pulsed plasma approach.

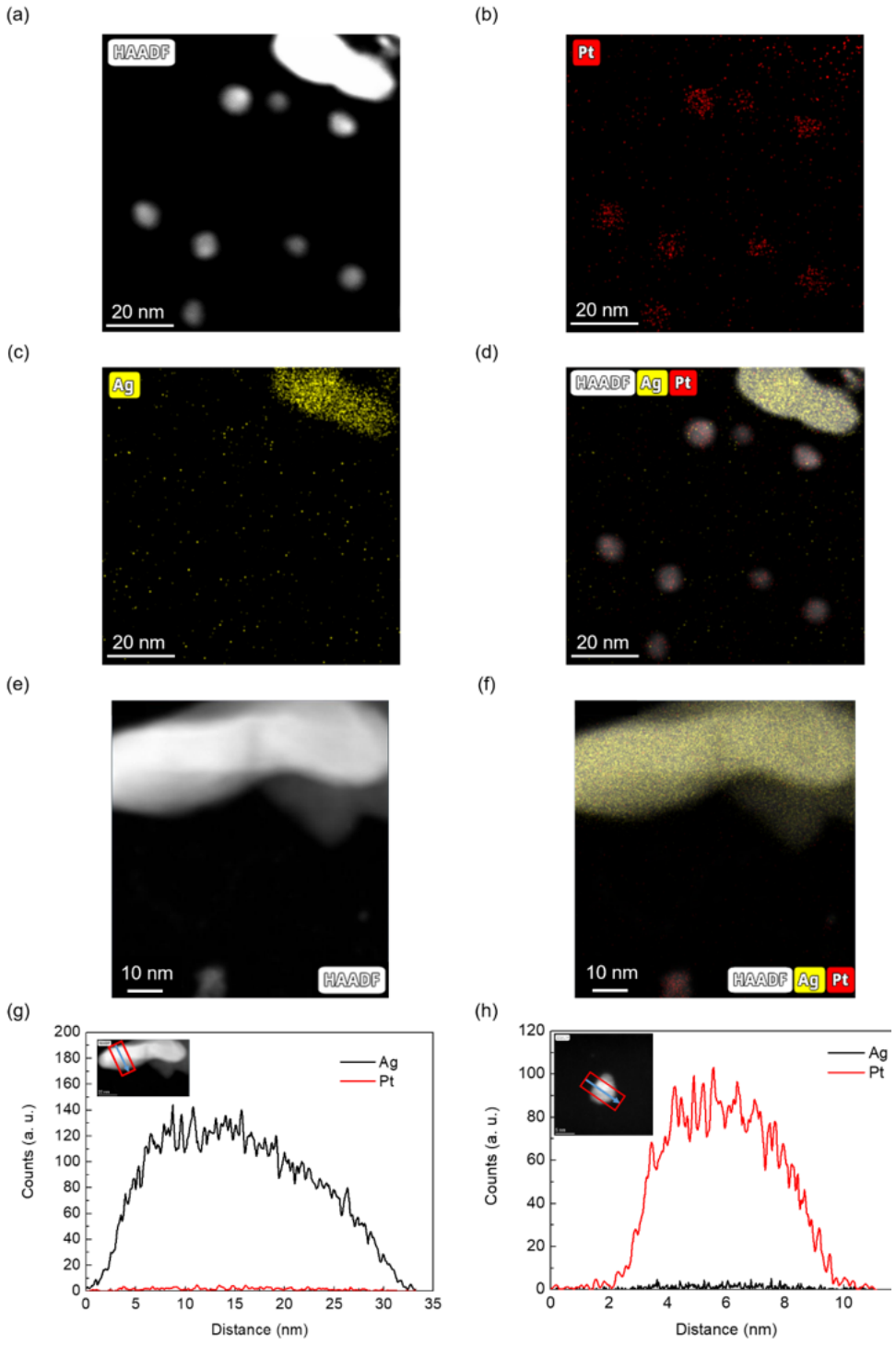


Figure 4.15 (a) Low-magnification dark-field STEM image, (b) EDS Pt mapping data, (c) EDS Ag mapping data, and (d) overlapping Ag and Pt EDS mapping data with the STEM image of the nanoparticles synthesized from thermal reduction. From another spot in the same sample, we conducted measurements again with the line scans as shown in the following figures. (e) Dark-field STEM image and (f) overlapping Ag and Pt EDS mapping data with STEM image of the nanoparticles synthesized from thermal reduction. (g) Corresponding EDS line scan of the nanoparticles at the top with only Ag signals. (h) Corresponding EDS line scan of the nanoparticle in the bottom with only Pt signals.

4.5 Conclusions

In conclusion, we have successfully demonstrated a synthetic strategy to form mixed bimetallic nanoparticles of immiscible metals. The interactions between pulsed plasma and metal precursor salts under certain conditions enable the formation of alloys. Our findings reveal that there are three key requirements for the exclusive formation of alloy nanoparticles without monometallic ones: (1) high reduction rates of metal precursors, facilitating the kinetic trapping of immiscible metal atoms into alloy nanoparticles, (2) similar reduction rates for the respective metal salt precursors, ensuring consistent mixing during the growth process, and (3) careful control of the nucleation process to prevent "burst nucleation", which occurs when local concentrations of reduced metal atom monomers exceed a critical threshold. We believe that this synthetic strategy has the potential to be applied in the synthesis of various alloys of immiscible metals, opening new possibilities in the field of nanomaterial synthesis.

4.6 References

1. Chen, H.-T.; Lee, D.; Linic, S., Formation of Mixed Bimetallic Nanoparticles of Immiscible Metals through Plasma-Induced Reduction of Precursors in Solutions: A Case Study of Ag–Pt Alloy Nanoparticles. *Chemistry of Materials* **2023,** *35* (16), 6557-6565.

2. Gilroy, K. D.; Ruditskiy, A.; Peng, H.-C.; Qin, D.; Xia, Y., Bimetallic Nanocrystals: Syntheses, Properties, and Applications. *Chemical Reviews* **2016,** *116* (18), 10414-10472.

3. Li, H.; Luo, L.; Kunal, P.; Bonifacio, C. S.; Duan, Z.; Yang, J. C.; Humphrey, S. M.; Crooks, R. M.; Henkelman, G., Oxygen Reduction Reaction on Classically Immiscible Bimetallics: A Case Study of RhAu. *The Journal of Physical Chemistry C* **2018,** *122* (5), 2712-2716.

4. Duan, Z.; Timoshenko, J.; Kunal, P.; House, S. D.; Wan, H.; Jarvis, K.; Bonifacio, C.; Yang, J. C.; Crooks, R. M.; Frenkel, A. I.; Humphrey, S. M.; Henkelman, G., Structural Characterization of Heterogeneous RhAu Nanoparticles from a Microwave-Assisted Synthesis. *Nanoscale* **2018,** *10* (47), 22520-22532.

5. García, S.; Zhang, L.; Piburn, G. W.; Henkelman, G.; Humphrey, S. M., Microwave Synthesis of Classically Immiscible Rhodium–Silver and Rhodium–Gold Alloy Nanoparticles: Highly Active Hydrogenation Catalysts. *ACS Nano* **2014,** *8* (11), 11512-11521.

6. Okamoto, H.; Schlesinger, M. E.; Mueller, E. M., *Alloy Phase Diagrams*. ASM International: 2016; Vol. 3.

7. Guo, H.; Li, H.; Jarvis, K.; Wan, H.; Kunal, P.; Dunning, S. G.; Liu, Y.; Henkelman, G.; Humphrey, S. M., Microwave-Assisted Synthesis of Classically Immiscible Ag–Ir Alloy Nanoparticle Catalysts. *ACS Catalysis* **2018,** *8* (12), 11386-11397.

8. Zhang, Z.; Nenoff, T. M.; Huang, J. Y.; Berry, D. T.; Provencio, P. P., Room Temperature Synthesis of Thermally Immiscible Ag−Ni Nanoalloys. *The Journal of Physical Chemistry C* **2009,** *113* (4), 1155-1159.

9. Holewinski, A.; Idrobo, J.-C.; Linic, S., High-Performance Ag–Co Alloy Catalysts for Electrochemical Oxygen Reduction. *Nature Chemistry* **2014,** *6* (9), 828-834.

10. Thomas, J. M.; Johnson, B. F. G.; Raja, R.; Sankar, G.; Midgley, P. A., High-Performance Nanocatalysts for Single-Step Hydrogenations. *Accounts of Chemical Research* **2003,** *36* (1), 20-30.

11. Rutledge, R. D.; Morris, W. H.; Wellons, M. S.; Gai, Z.; Shen, J.; Bentley, J.; Wittig, J. E.; Lukehart, C. M., Formation of FePt Nanoparticles Having High Coercivity. *Journal of the American Chemical Society* **2006,** *128* (44), 14210-14211.

12. Aslam, U.; Linic, S., Kinetic Trapping of Immiscible Metal Atoms into Bimetallic Nanoparticles through Plasmonic Visible Light-Mediated Reduction of a Bimetallic Oxide Precursor: Case Study of Ag–Pt Nanoparticle Synthesis. *Chemistry of Materials* **2016,** *28* (22), 8289-8295.

13. Marbella, L. E.; Chevrier, D. M.; Tancini, P. D.; Shobayo, O.; Smith, A. M.; Johnston, K. A.; Andolina, C. M.; Zhang, P.; Mpourmpakis, G.; Millstone, J. E., Description and Role of Bimetallic Prenucleation Species in the Formation of Small Nanoparticle Alloys. *Journal of the American Chemical Society* **2015,** *137* (50), 15852-15858.

14. Zhang, S.; Chen, C.; Cargnello, M.; Fornasiero, P.; Gorte, R. J.; Graham, G. W.; Pan, X., Dynamic Structural Evolution of Supported Palladium–Ceria Core–Shell Catalysts Revealed by in situ Electron Microscopy. *Nature Communications* **2015,** *6* (1), 7778.

15. Bruggeman, P. J.; Frontiera, R. R.; Kortshagen, U. R.; Kushner, M. J.; Linic, S.; Schatz, G. C.; Andaraarachchi, H.; Exarhos, S.; Jones, L. O.; Mueller, C. M.; Rich, C. C.; Xu, C.; Yue, Y.; Zhang, Y., Plasma-Driven Solution Electrolysis. *Journal of Applied Physics* **2021,** *129* (20), 200902.

16. Maguire, P.; Rutherford, D.; Macias-Montero, M.; Mahony, C.; Kelsey, C.; Tweedie, M.; Pérez-Martin, F.; McQuaid, H.; Diver, D.; Mariotti, D., Continuous in-Flight Synthesis for on-Demand Delivery of Ligand-Free Colloidal Gold Nanoparticles. *Nano Letters* **2017,** *17* (3), 1336-1343.

17. Chen, Q.; Li, J.; Li, Y., A Review of Plasma–Liquid Interactions for Nanomaterial Synthesis. *Journal of Physics D: Applied Physics* **2015,** *48* (42), 424005.

18. Yan, T.; Zhong, X.; Rider, A. E.; Lu, Y.; Furman, S. A.; Ostrikov, K., Microplasma-Chemical Synthesis and Tunable Real-Time Plasmonic Responses of Alloyed Au_xAg_{1-x} Nanoparticles. *Chemical Communications* **2014,** *50* (24), 3144-3147.

19. Di, L.; Xu, W.; Zhan, Z.; Zhang, X., Synthesis of Alumina Supported Pd–Cu Alloy Nanoparticles for CO Oxidation Via a Fast and Facile Method. *RSC Advances* **2015,** *5* (88), 71854-71858.

20. Shirai, H.; Nguyen, M. T.; Čempel, D.; Tsukamoto, H.; Tokunaga, T.; Liao, Y.-C.; Yonezawa, T., Preparation of Au/Pd Bimetallic Nanoparticles by a Microwave-Induced Plasma in Liquid Process. *Bulletin of the Chemical Society of Japan* **2017,** *90* (3), 279-285.

21. Yue, Y.; Kondeti, V. S. S. K.; Sadeghi, N.; Bruggeman, P. J., Plasma Dynamics, Instabilities and OH Generation in a Pulsed Atmospheric Pressure Plasma with Liquid Cathode: A Diagnostic Study. *Plasma Sources Science and Technology* **2022,** *31* (2), 025008.

22. Kilaas, R., Optimal and near-Optimal Filters in High-Resolution Electron Microscopy. *Journal of Microscopy* **1998,** *190* (1-2), 45-51.

23. Savitzky, A.; Golay, M. J. E., Smoothing and Differentiation of Data by Simplified Least Squares Procedures. *Analytical Chemistry* **1964,** *36* (8), 1627-1639.

24. Bonet, F.; Guéry, C.; Guyomard, D.; Herrera Urbina, R.; Tekaia-Elhsissen, K.; Tarascon, J. M., Electrochemical Reduction of Noble Metal Species in Ethylene Glycol at Platinum and Glassy Carbon Rotating Disk Electrodes. *Solid State Ionics* **1999,** *126* (3), 337-348.

25. Bonet, F.; Guéry, C.; Guyomard, D.; Herrera Urbina, R.; Tekaia-Elhsissen, K.; Tarascon, J. M., Electrochemical Reduction of Noble Metal Compounds in Ethylene Glycol. *International Journal of Inorganic Materials* **1999,** *1* (1), 47-51.

26. Wang, Y.; Ren, J.; Deng, K.; Gui, L.; Tang, Y., Preparation of Tractable Platinum, Rhodium, and Ruthenium Nanoclusters with Small Particle Size in Organic Media. *Chemistry of Materials* **2000,** *12* (6), 1622-1627.

27. Herricks, T.; Chen, J.; Xia, Y., Polyol Synthesis of Platinum Nanoparticles: Control of Morphology with Sodium Nitrate. *Nano Letters* **2004,** *4* (12), 2367-2371.

28. Zhao, S.-Y.; Chen, S.-H.; Wang, S.-Y.; Li, D.-G.; Ma, H.-Y., Preparation, Phase Transfer, and Self-Assembled Monolayers of Cubic Pt Nanoparticles. *Langmuir* **2002,** *18* (8), 3315-3318.

29. Goldberg, R. N.; Hepler, L. G., Thermochemistry and Oxidation Potentials of the Platinum Group Metals and Their Compounds. *Chemical Reviews* **1968,** *68* (2), 229-252.

30. Yao, T.; Liu, S.; Sun, Z.; Li, Y.; He, S.; Cheng, H.; Xie, Y.; Liu, Q.; Jiang, Y.; Wu, Z.; Pan, Z.; Yan, W.; Wei, S., Probing Nucleation Pathways for Morphological Manipulation of Platinum Nanocrystals. *Journal of the American Chemical Society* **2012,** *134* (22), 9410-9416.

31. Alnot, M.; Gorodetskii, V.; Cassuto, A.; Ehrhardt, J. J., Auger Electron Spectroscopy, X-Ray Photoelectron Spectroscopy, Work Function Measurements and Photoemission of Adsorbed Xenon on Thin Films of Pt-Re(111) Alloys. *Thin Solid Films* **1987,** *151* (2), 251-262.

32. Romeo, M.; Majerus, J.; Legare, P.; Castellani, N. J.; Leroy, D. B., Photoemission Study of Pt Adlayers on Ni(111). *Surface Science* **1990,** *238* (1), 163-168.

33. Schaal, M. T.; Hyman, M. P.; Rangan, M.; Ma, S.; Williams, C. T.; Monnier, J. R.; Medlin, J. W., Theoretical and Experimental Studies of Ag–Pt Interactions for Supported Ag–Pt Bimetallic Catalysts. *Surface Science* **2009,** *603* (4), 690-696.

34. Rodriguez, J. A.; Kuhn, M., Electronic and Chemical Properties of Ag/Pt(111) and Cu/Pt(111) Surfaces: Importance of Changes in the d Electron Populations. *The Journal of Physical Chemistry* **1994,** *98* (44), 11251-11255.

35. Davey, W. P., Precision Measurements of the Lattice Constants of Twelve Common Metals. *Physical Review* **1925,** *25* (6), 753-761.

36. Lubarda, V. A., On the Effective Lattice Parameter of Binary Alloys. *Mechanics of Materials* **2003,** *35* (1), 53-68.

37. Jette, E. R.; Foote, F., Precision Determination of Lattice Constants. *The Journal of Chemical Physics* **1935,** *3* (10), 605-616.

38. Bard, A. J.; Faulkner, L. R., *Electrochemical Methods: Fundamentals and Applications*. Sec. ed.; John Wiley & Sons: New York, 2001.

39. Gutmann, V., *The Donor-Acceptor Approach to Molecular Interactions*. 1 ed.; Springer New York: New York, 1978; p XVI, 279.

40. Lay, P. A.; McAlpine, N. S.; Hupp, J. T.; Weaver, M. J.; Sargeson, A. M., Solvent-Dependent Redox Thermodynamics of Metal Amine Complexes. Delineation of Specific Solvation Effects. *Inorganic Chemistry* **1990,** *29* (21), 4322-4328.

41. Richards, V. N.; Rath, N. P.; Buhro, W. E., Pathway from a Molecular Precursor to Silver Nanoparticles: The Prominent Role of Aggregative Growth. *Chemistry of Materials* **2010,** *22* (11), 3556-3567.

42. Besson, C.; Finney, E. E.; Finke, R. G., A Mechanism for Transition-Metal Nanoparticle Self-Assembly. *Journal of the American Chemical Society* **2005,** *127* (22), 8179-8184.

43. Thanh, N. T. K.; Maclean, N.; Mahiddine, S., Mechanisms of Nucleation and Growth of Nanoparticles in Solution. *Chemical Reviews* **2014,** *114* (15), 7610-7630.

44. Mulvihill, M. J.; Ling, X. Y.; Henzie, J.; Yang, P., Anisotropic Etching of Silver Nanoparticles for Plasmonic Structures Capable of Single-Particle SERS. *Journal of the American Chemical Society* **2010,** *132* (1), 268-274.

45. Holmbom, G.; Jacobson, B. E., Nucleation and Initial Growth of Pulse-Plated Gold on Crystalline and Amorphous Substrates. *Journal of The Electrochemical Society* **1988,** *135* (11), 2720-2725.

Chapter 5 Plasma-Anode Reaction Mechanisms: Direct Cation Oxidation Versus Hydroxyl-Radical Mediation

5.1 Summary

Charge transfer at the plasma-liquid interface is critical to plasma-driven solution electrolysis (PDSE). Still, the reaction mechanism under a plasma-anode/liquid-cathode configuration remains unclear. We evaluate two mechanisms at a plasma-anode/water-cathode interface: (1) a cascading pathway in which cation-water reactions generate •OH that oxidizes solutes, and (2) a direct cation-solute pathway without intermediate involvement. Isopropanol alcohol (IPA) oxidation serves as a probe molecule due to its lower O-H bond dissociation enthalpy change than that of water. We discovered that this reaction was not suppressed by intermediate-scavenging experiments, which suggests a direct cation-IPA reaction. Moreover, we demonstrated that the IPA reaction rate constants depended on plasma parameters and that the Faradaic efficiency trends differed between the above-mentioned two mechanisms. These results identify a direct cation-substrate oxidation reaction pathway and highlight the need for mechanism understanding.

5.2 Introduction

Plasma-driven solution electrolysis (PDSE) is an emerging electrochemical system in which one or both electrodes are replaced with a gas discharge.[1-2] The plasma-liquid interface functions as an “electrode” that drives unique solution chemistry with plasma-induced species, including electrons, ions, photons, and neutral radicals.[3-4] These species enable chemical

processes that are difficult to achieve via traditional electrolysis or thermal routes.[4-6] The reactivity and structure of this interface are governed by plasma-operating parameters, including applied voltage waveform and frequency, feed-gas composition, and applied power.[4, 7-10] In particular, differences in frequency, radio-frequency (RF) discharges, dielectric-barrier discharges (DBD), and direct-current (DC) plasmas lead to distinct reactive-species fluxes and interfacial characteristics.[11-14]

Among these discharge modes, DC plasmas impose a well-defined current flow direction as the plasma electrode functions exclusively as either an anode or a cathode for a given polarity. At the DC plasma-liquid interface, charge transfer plays a crucial role as the electric field drives electrons and ions across the sheath into the liquid, where they initiate reactions.[15] In a plasma-cathode system, electrons are the primary charge carriers injected from the plasma phase into the liquid phase, where they rapidly solvate to form solvated electrons (e_{sol}^-).[16-18] e_{sol}^- are strong reducing agents with a reduction potential of -2.9V versus NHE (normal hydrogen electrode) that mainly drive reduction reactions.[19-20]

Conversely, in a plasma-anode system, the charge transfer mechanism and the cascading reactions remain unclear. Instead of simply flipping the electron-flow direction, the low secondary-electron emission coefficient of the water surface makes electron emission from the water surface challenging.[21-22] As illustrated in Figure 5.1, the secondary-electron emission coefficient was estimated to be 10^{-5} with argon discharge, based on Paschen's law (see Chapter 1).

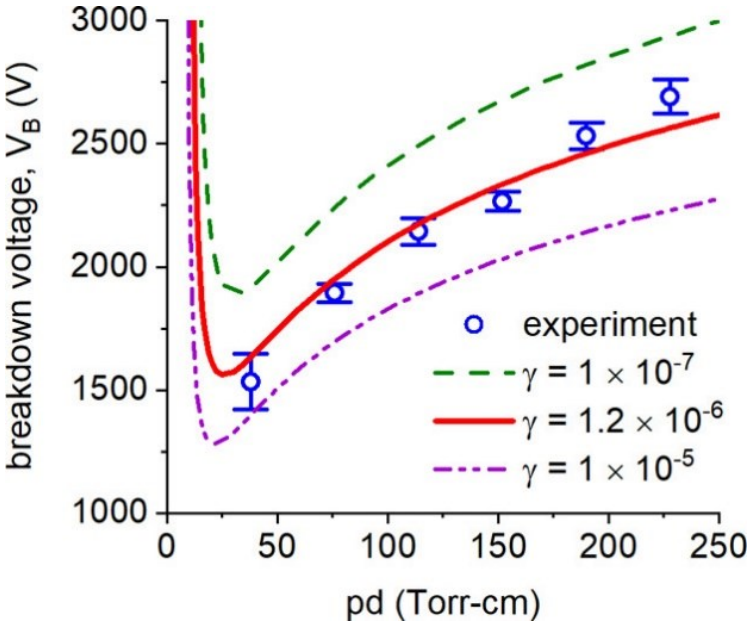


Figure 5.1 Breakdown voltage as a function of pd (pressure times distance). Fitting results suggest that the secondary-electron emission coefficient is at most 10^{-5}. Adapted from [21].

Given the low coefficient, it is believed that ions, especially cations, are the primary charge carriers that sustain the current, with average energies below ~10 eV.[23] In plasma-water systems, these cations are believed to react with water within a short penetration depth to form hydroxyl radicals (•OH), which then drive oxidation reactions or lead to hydrogen peroxide (H_2O_2) formation.[24-25] For instance, Martin *et al.* proposed that approximately one e_{sol}^- and two •OH are yielded per incident argon ion.[26] The possible reactions that lead to the formation of these reactive species are plotted in Figure 5.2.

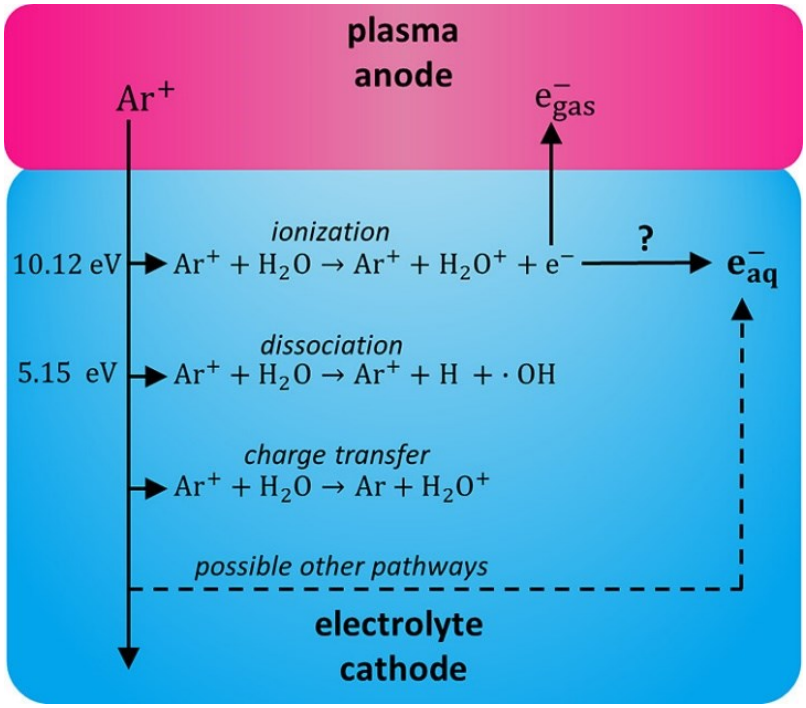


Figure 5.2 Diagram of possible processes driven by plasma ions injected into water for an argon anode glow discharge electrolysis. Adapted from [26].

Here, we propose an alternative reaction mechanism for charge transfer-induced reactions in a plasma-anode/water-cathode configuration. Instead of the cation-invoked cascading reaction mechanism, in which cation-water reactions generate •OH that subsequently drives oxidation reactions, cations may react directly with other liquid-phase species without intermediate formation. We deliberately selected isopropyl alcohol (IPA) as a target molecule because its O-H bond exhibits a lower dissociation enthalpy change than the first O-H bond of water.[27-28] Thus, relative to H-OH bond cleavage of water to form •OH, O-H cleavage in IPA should be more favorable, making IPA more likely to react with cations at the plasma-liquid interface. We distinguished this pathway using intermediate-scavenging experiments, which quenched reactive intermediates, especially •OH. The results demonstrated that the addition of scavengers did not measurably affect the IPA oxidation rate, consistent with a direct cation-IPA route. Furthermore,

the Faradaic efficiency (reaction per incident ion) responded differently to changes in pulse width for the two mechanisms, underscoring the importance of identifying the reaction pathway.

5.3 Experimental Section

We used the pulsed DC helium (He) plasma with both plasma-cathode (negative polarity) and plasma-anode (positive polarity) configurations. For plasma generation, high-voltage power supplies (negative polarity: Spellman SL10N300; positive polarity: Spellman SL10PN300) were integrated with a function generator (Tektronix AFG2021) and a pulse generator (DEI PVX-4110), which was connected to a plasma jet. The plasma jet used in this study is similar to the one reported in the previous literature.[29] Within the plasma jet, a ballast resistance (500 Ω) was connected in series with a tungsten needle. The tungsten needle was inserted inside a quartz tube; through which He was supplied as the working gas at a flow rate of 200 standard cubic centimeters per minute (sccm). The pulsed discharge was operated at a repetition frequency of 1 kHz; namely, one single period was 1000 μs. The plasma on-time, defined by the pulse width, was varied to 3, 5, and 10 μs depending on the experimental conditions. For the H-cell setup, a Nafion membrane (Nafion 115) with an O-ring was installed between the two chambers to separate the cells while maintaining current continuity. Both chambers were vigorously stirred with stir bars at 800 rpm. A clean platinum wire served as the grounding electrode in one chamber, while the plasma was ignited in the other. Discharge current profiles were measured using a Rogowski coil (Pearson 2877) and recorded with an oscilloscope (Tektronix DPO 2022B). The entire H-cell was submerged in a water bath maintained at approximately 20 °C. 100 mM of potassium sulfate (K_2SO_4) was also added to the solution as the supporting electrolyte.

Isopropanol alcohol (IPA, C_3H_8O) and acetone (C_3H_6O) were added to deionized water (18.2 MΩ·cm at 25 °C) with specific concentrations. The outlet gases (He flow rate 200 sccm) were connected to the Agilent 7890B/5977A series gas chromatograph/mass selective detector (GC-MS) system and were analyzed every 16 min. The column is selected to be water-resistant due to the inevitable injection of vapor. Also, we used a solvent delay to prevent possible damage to the GC filament. 100 mM of K_2SO_4 was added to align with the experimental conditions. Calibration lines were established by measuring the GC-MS characteristic peak area at known concentrations, as specified in Figure 5.3. The manual injection of the liquid phase solution was not available with this setup due to the addition of the supporting electrolyte.

The use of a plasma-cathode configuration resulted from a comparison with the consumption rate of IPA with high concentrations. During these experiments, when the IPA initial concentrations were extremely high, the contribution from charge-induced reactions was relatively negligible. That is, the main consumption pathway of IPA resulted from the evaporation due to the possible temperature increase at the interface. This consumption rate constant was compared to the one measured with a plasma-cathode configuration. It turned out that the rate constants from plasma-cathode configurations were higher than those from the evaporation processes measured at high initial temperatures with the same plasma parameters (current input and pulse width). Therefore, the consumption rates from the plasma-cathode configurations were used to calibrate the non-Faradaic processes. Without the calibration, the Faradaic efficiency might be higher than 100%.

During the process, the pressure buildup especially in the plasma chamber should be noticed and prevented. As the chamber was connected to a GC-MS, the gas pressure was higher than the atmospheric pressure due to the gas flow across the the GC-MS. If the pressure buildup

was significant, the liquid level of the two chambers were observed to be significantly different. It often resulted from the wrong installation of the membrane and the O-ring, which can be fixed by tightening the clip that held the two chambers. Meanwhile, the sealing with an O-ring should also be intact to prevent liquid leakage to the water bath. Otherwise, the reaction condition might be off with wrong IPA concentrations or a larger gas gap between the needle tip and the liquid surface.

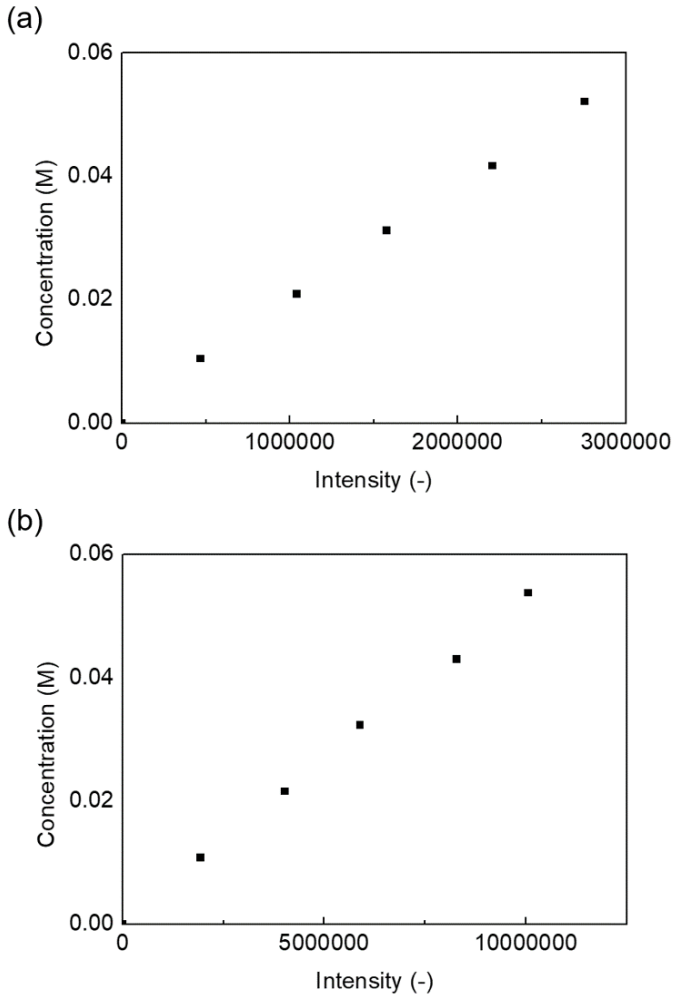


Figure 5.3 The measured intensity from a GC-MS versus the known concentration of (a) IPA and (b) acetone in the liquid phase. Both curves show linear behaviors and can be used as calibration lines.

Ferricyanide ($K_3[Fe(CN)_6]$) and Ferrocyanide ($K_4[Fe(CN)_6]\bullet 3H_2O$) were dissolved in deionized water (18.2 MΩ·cm at 25 °C). The redox couple is specifically chosen due to its pH independence. The concentrations of the redox species were specified for each experimental condition. 100 mM of K_2SO_4 was also in the solution as the supporting electrolyte. The total concentration of 500 mM of the redox couple is close to the solubility limits, which might be affected due to the addition of the supporting electrolyte. For the scavenging experiments, the scavengers were added to both chambers in an H-cell to avoid the ion strength difference. KCl was added as a scavenger for •OH. For the redox couple-plasma interaction experiments, the H-cell setup was also utilized to separate the concentration changes. The initial concentrations of the two chambers were identical. The solution with the redox couple was diluted 30 times with water to measure the absorbance at 420 nm using a Thermo Scientific Evolution 300 ultraviolet-visible (UV-vis) spectrophotometer. The calibration line in Figure 5.4 was established with known concentrations of the redox couple. The current profiles with the redox couple and with the IPA were similar due to the high conductivity of the solutions.

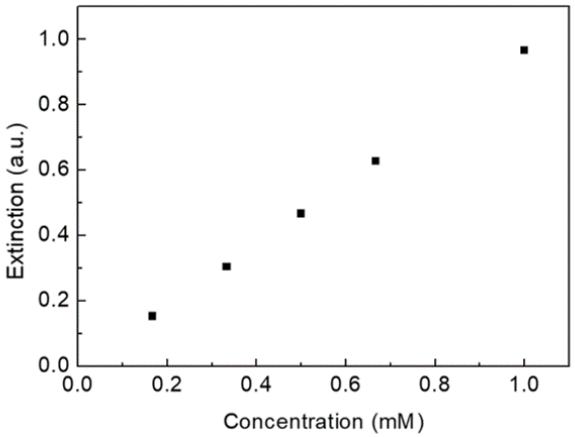


Figure 5.4 Known ferricyanide concentrations versus the extinction values from UV-vis spectra, which illustrates a linear behavior.

5.4 Results and Discussions

The experimental setup is illustrated in Figure 5.5a. An H-cell configuration with a semipermeable membrane was used to separate the plasma electrode from the grounding electrode.[29] In the plasma-electrode chamber, a tungsten needle was inserted with a 200 sccm He flow. The tungsten needle was connected to a power supply and a pulser to ignite plasma. Both chambers contained an aqueous solution with 100 mM K_2SO_4 as the supporting electrolyte, while 20 mM IPA was added to the plasma chamber. The entire H-cell was submerged in a water bath maintained at approximately 20 °C.

The plasma chamber was connected to a GC-MS for analysis of the gas-phase composition. By leveraging the equilibrium between the liquid and gas phases, these measurements were used to quantify liquid-phase species and their concentrations. In Figure 5.5b, the GC-MS spectra obtained during plasma-liquid interactions are presented. The plasma was operated under a plasma-anode configuration with three different current values (2.5, 3, and 3.5 mA) at a pulse width of 10 μs. The corresponding current profiles are shown in Figure 5.6. Two peaks were observed in the GC-MS spectra, corresponding to IPA (retention time 9.7 min) and acetone (retention time 9.4 min). The appearance of the acetone signal can be attributed to plasma-liquid interactions, as its intensity increased with increasing current values. The area under a characteristic GC-MS peak reflects the gas-phase concentration of a species and, via gas-liquid equilibrium, can be correlated to its liquid-phase concentration. These correlations for IPA and acetone are shown in Figures 5.3a and 5.3b, respectively. With these calibrations, measured GC-MS peak areas can be converted to liquid-phase concentrations of IPA and acetone.

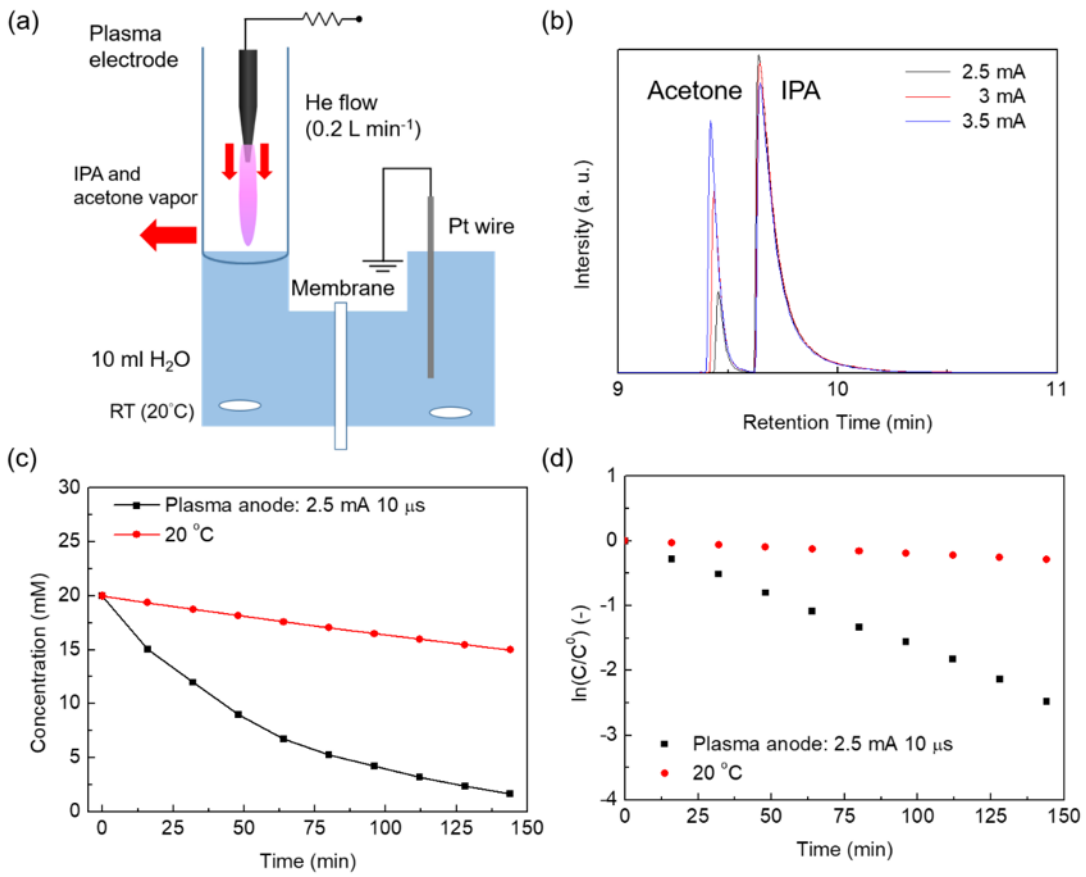


Figure 5.5 (a) Plasma reactor with an H-cell configuration. Both chambers were stirred to mitigate the mass-transfer limitations. (b) GC-MS spectra with three current values. The peaks are assigned to acetone and IPA, respectively. (c) The IPA concentration versus reaction time for a plasma-anode configuration (pulse width 10 μs, current 2.5 mA) and for 20 ˚C IPA evaporation. (d) Natural-log scale concentrations normalized by the initial concentration versus reaction time, converted from (c).

Using the GC-MS calibration, we quantified the time-dependent change in liquid-phase IPA concentration during plasma-liquid interaction. The data in Figure 5.5c show the IPA concentration versus time for a plasma-anode configuration (pulse width 10 μs and current 2.5 mA). The IPA consumption with the plasma-liquid interaction far exceeded evaporation at 20 ˚C. The measured liquid-phase IPA concentrations were converted to a natural-log scale and normalized by the initial concentration (C_0), denoted as $\ln(C/C_0)$. The data in Figure 5.5d suggest that plotting $\ln(C/C_0)$ versus time yields a linear trend, indicating that the consumption of IPA is

a first-order reaction with respect to its concentration. The first-order rate constant, obtained from the slope, is 0.0168 min^{-1} for the plasma anode at 10 μs and 2.5 mA. In Figure 5.7, the acetone concentrations versus time under the specific plasma condition are also shown. Acetone concentration decayed faster than IPA due to its higher volatility.[30] Therefore, we used IPA consumption as a more reliable indicator of the reaction kinetics of the IPA-to-acetone conversion.

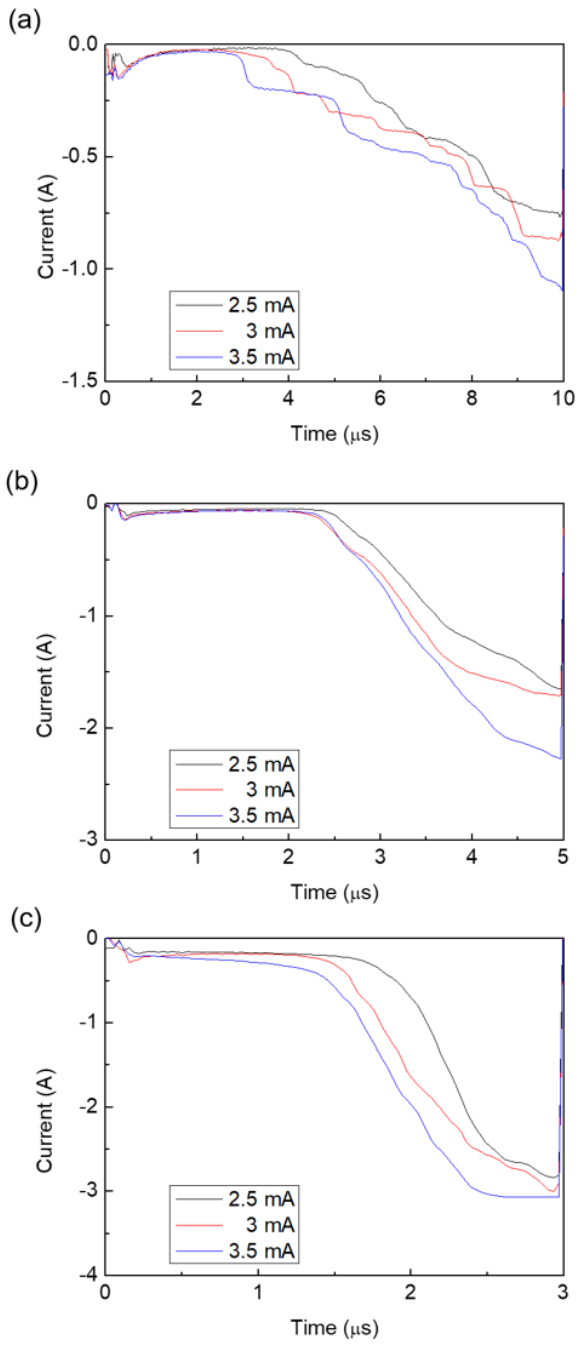


Figure 5.6 The measured current profiles for the plasma anode with the current values 2.5, 3, and 3.5 mA for pulse widths (a) 10 μs, (b) 5 μs, and (c) 3 μs. For a given current value, the total charge transfer per pulse is calculated and controlled by applying different voltages. During the pulse with a specified current value and a pulse width, a constant voltage is applied to the high-voltage electrode.

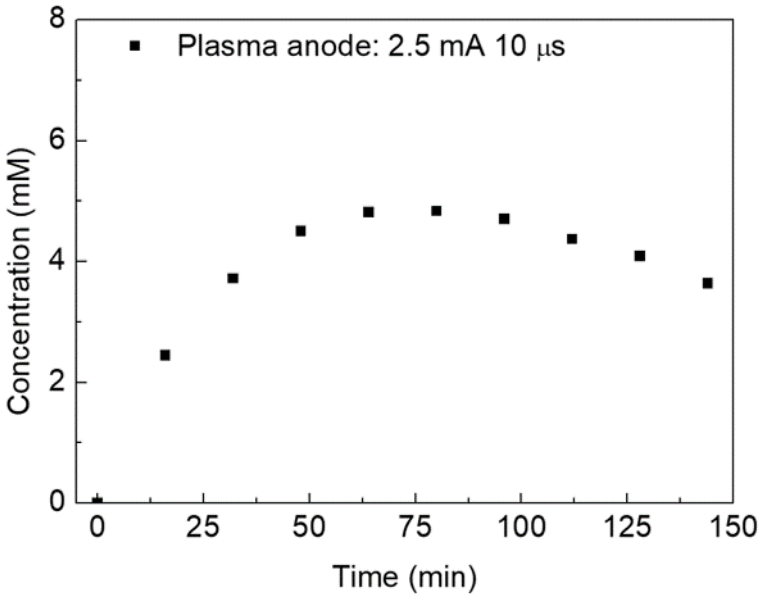


Figure 5.7 Measured acetone concentration versus plasma-liquid interaction time. Acetone concentrations plateaued and decreased due to its high volatility.

IPA to acetone was employed as a probe reaction to elucidate the reaction pathway at the plasma-liquid interface under a plasma-anode configuration. In a plasma-anode configuration, where cations are the primary charge carriers, two possible reaction pathways may occur: (1) cations react with interfacial water molecules to generate short-lived reactive intermediates, most notably e_{sol}^- and •OH, which then react with liquid-phase species; and (2) cations undergo direct reactions with target molecules, with minimal contribution from reactive intermediates. To distinguish between the two pathways, we implemented an intermediate-scavenging approach. For the first mechanism involving reactive intermediates, since IPA to acetone is an oxidation reaction, •OH is expected to be the primary oxidant. A high rate constant for the •OH and IPA reaction in the liquid phase has been reported.[31-32] We therefore hypothesize that quenching •OH with scavengers should decrease the IPA consumption rate and thereby lower the apparent first-order rate constant if the IPA-to-acetone conversion is mediated by •OH. This hypothesis is tested by the introduction of ferrocyanide ions and Cl^-, both of which react rapidly with •OH,

listed in Reaction 5.2 and Reaction 5.3.[32-33] The rate constants of the reactions are listed in Table 5.1.

Table 5.1 Rate constants for the reactions

#	Reaction	Rate constant	References
5.1	$IPA + \bullet OH \rightarrow C_3H_6OH + H_2O$	$k = 1.9 \times 10^9\ M^{-1}\ s^{-1}$	[32]
5.2	$Fe(CN)_6^{3-} + \bullet OH \rightarrow Fe(CN)_6^{4-} + OH^-$	$k = 1.1 \times 10^{10}\ M^{-1}\ s^{-1}$	[32]
5.3	$\bullet OH + Cl^- \rightarrow ClOH^-$	$k = 4.3 \times 10^9\ M^{-1}\ s^{-1}$	[33]
5.4	$2\ \bullet OH \rightarrow H_2O_2$	$k = 5.5 \times 10^9\ M^{-1}\ s^{-1}$	[32]

The $\ln(C/C_0)$ curves versus time with and without ferricyanide/ferrocyanide redox couple are illustrated in Figure 5.8a with a plasma-anode configuration at 2.5 mA and pulse width 10 μs. Ferrocyanide (reduced form) scavenges •OH to form ferricyanide (oxidized form), listed in Reaction 5.2. Ferrocyanide was tested at 0, 90, and 450 mM, with ferricyanide added to 0, 10, and 50 mM. Control experiments confirmed that the redox couple did not measurably react with IPA, indicating that the reaction is only driven by the plasma-liquid interactions. The three curves exhibited indistinguishable consumption rates and rate constants, indicating that the addition of ferrocyanide as an •OH scavenger did not affect the IPA-to-acetone reaction rate. Similarly, Cl^-, which scavenges •OH (Reaction 5.3), was added to the solution. The data in Figure 5.8b present the $\ln(C/C_0)$ curves versus time with and without Cl^-. The addition of 400 and 800 mM of Cl^- did not alter the $\ln(C/C_0)$ curves and the first-order rate constants, confirming that •OH scavengers did not affect the IPA-to-acetone conversion.

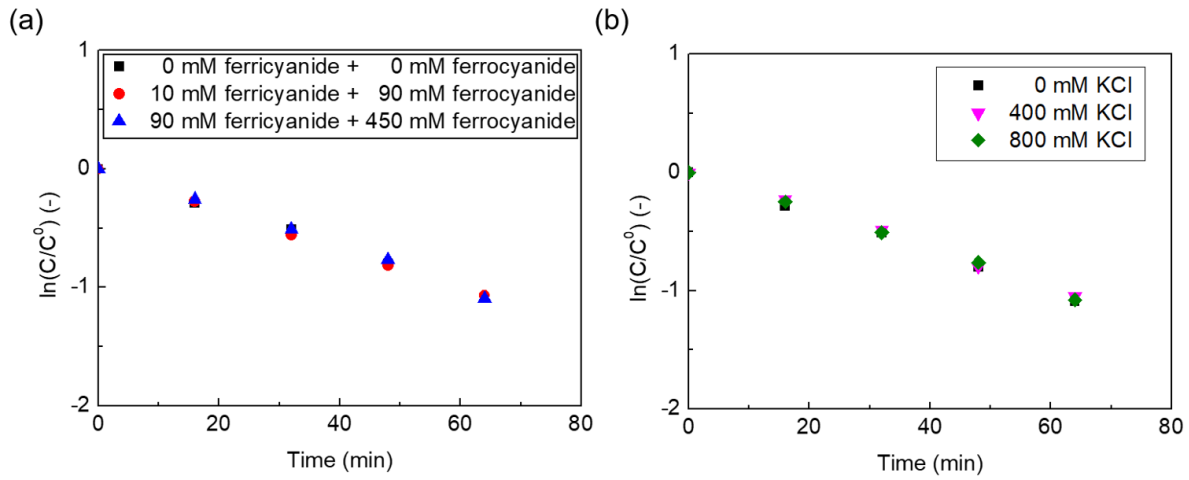


Figure 5.8 (a) $\ln(C/C_0)$ versus time for solutions containing different concentrations of ferricyanide/ferrocyanide redox couple. (b) $\ln(C/C_0)$ versus time with 0, 400, and 800 mM Cl^-. The two •OH scavengers both showed no measurable effect on the reaction. With a supporting electrolyte present in all cases, the addition of these salts did not alter the current or voltage profiles, which have been previously reported.[34]

Scavenging experiments indicate that the IPA-to-acetone oxidation reaction is unlikely to be mediated by •OH. Instead, the reaction may be driven by the direct reaction between IPA and cations. To further elucidate this reaction pathway, we measured the rate constants while systematically varying pulse width and discharge current, thereby modulating the peak current attained in each pulse. We hypothesized that, at fixed total charge input, the rate constant would be dependent on the pulse width, which altered the peak current and probably the ion energy distribution reaching the interface. To test the hypothesis, the contributions from other non-Faradaic processes, such as evaporation and probably ultraviolet (UV) photolysis, must be quantified and eliminated to reflect only the contributions from charge transfer.[4]

The non-Faradaic process contributions were measured with a plasma-cathode configuration. The corresponding current profiles are plotted in Figure 5.9. In this configuration, electrons are the primary charge carriers,[15] which are strong reducing agents and unlikely to drive the IPA oxidation reaction. Accordingly, the observed IPA loss is likely attributed to

evaporation and UV-induced photolysis, which are not driven by cation charge transfer. We assume that these processes resemble similar rates in both configurations. Namely, the rate constant differences between the two configurations are attributed to reflecting the cation-induced rate constants. The data in Figure 5.10a show the rate constants for plasma-cathode (negative polarity) and plasma-anode (positive polarity) configurations at currents of 2.5, 3, and 3.5 mA and pulse widths of 3, 5, and 10 μs. In general, the rate constant increased with increasing current and decreasing pulse width. Across all conditions, the plasma-anode configuration yielded higher rate constants than the plasma-cathode configuration, and the anode case exhibited greater dependence on the operating parameters.

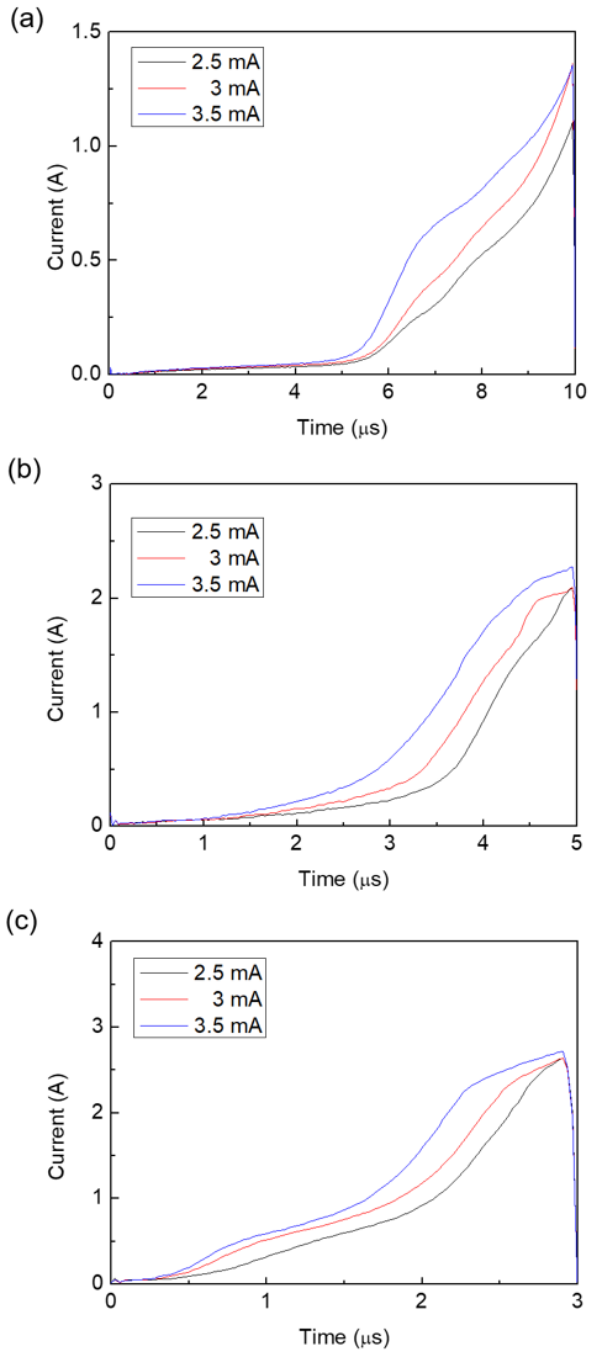


Figure 5.9 The measured current profiles for the plasma cathode with the current values 2.5, 3, and 3.5 mA for pulse widths (a) 10 μs, (b) 5 μs, and (c) 3 μs. For a given current value, the total charge transfer per pulse is calculated and controlled by applying different voltages. During the pulse with a specified current value and a pulse width, a constant voltage is applied to the high-voltage electrode.

As mentioned above, we attribute the difference in rate constants measured under the two configurations at identical current and pulse width conditions to cation-induced pathways. Accordingly, we define it as the cation-induced rate constant, which is illustrated in Figure 5.10b. This cation-induced rate constant increased with increasing current and decreasing pulse width, confirming our hypothesis that the rate constants were influenced by the pulse width. We noted that these rate constants exhibited a similar trend to the applied voltages, illustrated in Figure 5.11. Changes in the applied voltage likely modify the cation energy distribution during transfer across the plasma-liquid interface.[35] As the dissociation reaction rate of IPA may be dependent on ion energy distribution, increasing the fraction of cations that exceed activation thresholds for interfacial reactions may thereby elevate the measured rate constants.[36-37]

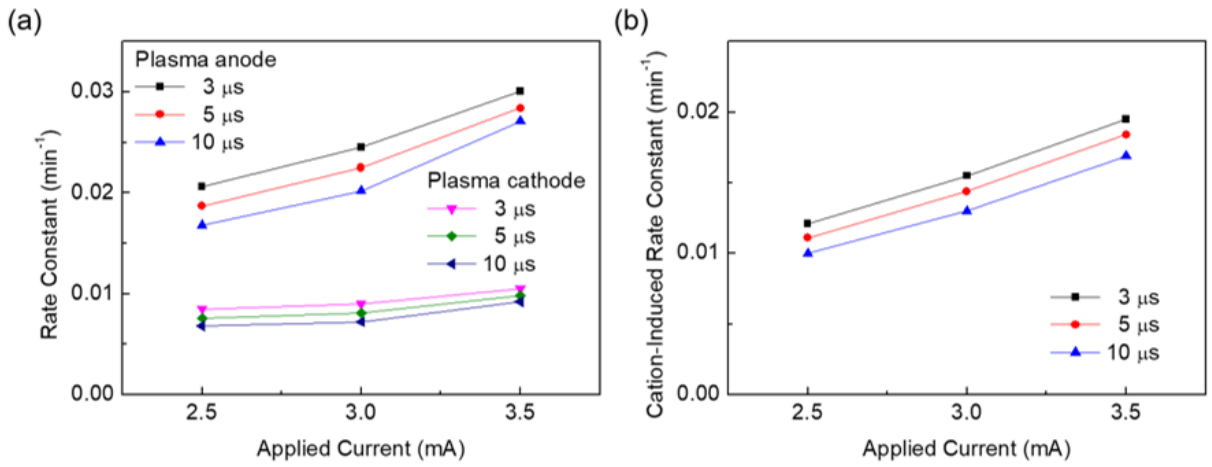


Figure 5.10 (a) Measured IPA consumption rate constant for both plasma-anode and plasma-cathode configurations. (b) Rate constants after eliminating the contribution from the non-Faradaic processes. These rate constants are attributed to cation-induced IPA reactions.

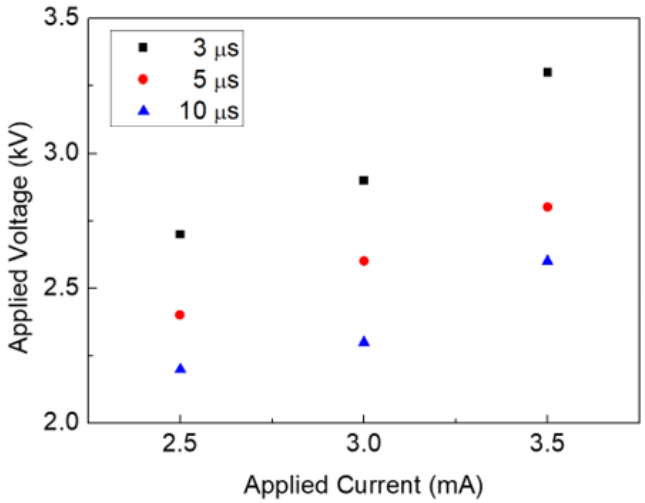


Figure 5.11 The applied voltages versus the applied current with 3, 5, and 10 μs pulse width. The voltages increased while the current increased and while the pulse width decreased.

We also design experiments to further distinguish between the two proposed reaction routes. In this experiment, we used ferricyanide/ferrocyanide redox couple, which is mentioned to be •OH scavengers.[32] The ferrocyanide-to-ferricyanide conversion is known to be mediated by •OH, as established in Chapter 3 and corroborated here by the use of •OH scavengers (Cl^-), which reduced the conversion. We hypothesized that these two reaction pathways would exhibit distinct dependences on plasma parameters, pulse width and current, reflecting their reaction mechanisms. For the redox couple part, solutions containing 10 mM ferricyanide and 90 mM ferrocyanide interacted with the plasma-anode configuration for 32 minutes in the same reactor setup.

The total ferricyanide molar increase normalized to charge input, defined as the Faradaic efficiency, is shown in Figure 5.12a for the plasma-anode configuration at currents of 2.5, 3, and 3.5 mA and pulse widths of 3, 5, and 10 μs. The over 100% faradaic efficiencies are plausibly due to the generation of more than one •OH per incident cation and to non-Faradaic contributions, such as mass transfer of gas phase-generated •OH into the liquid phase.[26, 29, 38] The

Faradaic efficiency decreased with increasing current and decreasing pulse width, likely due to mass-transfer limitations and •OH recombination reaction (Reaction 5.4) to H_2O_2.[39]

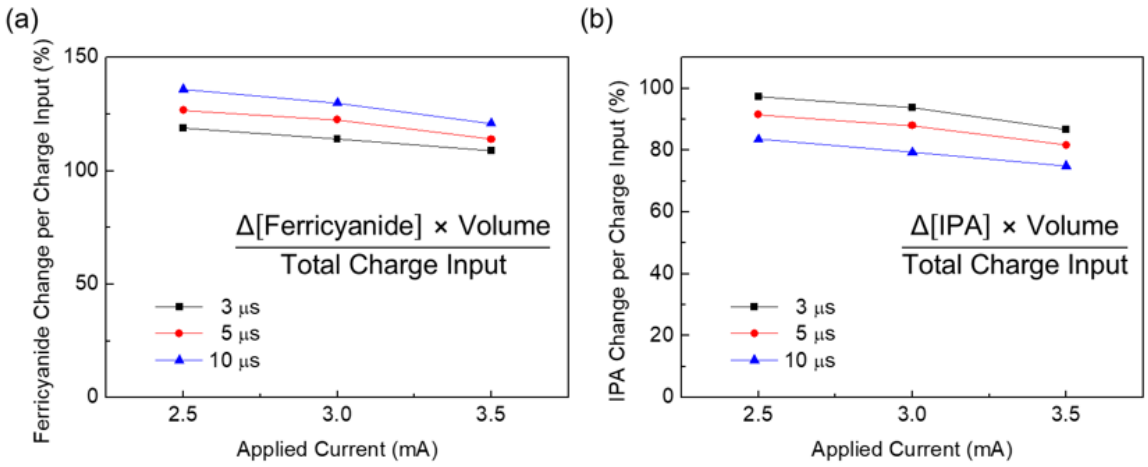


Figure 5.12 (a) Oxidation of ferrocyanide to ferricyanide driven by plasma-liquid interaction in a plasma-anode configuration. (b) Oxidation of IPA to acetone under the same conditions. The molar changes are normalized to the charge input.

The cation-induced IPA molar change per charge input under the same plasma conditions is illustrated in Figure 5.12b. Non-Faradaic contributions were removed by subtracting the IPA loss measured under the plasma-cathode configuration. In contrast to the ferrocyanide oxidation in Figure 5.12a, IPA conversion exhibits higher Faradaic efficiency at shorter pulse widths. This distinct response to pulse width variation likely arises from the reaction pathway, as the ferrocyanide oxidation reaction is mediated by •OH, while the IPA-to-acetone conversion is driven by direct cation-IPA reactions. Accordingly, the optimal plasma parameters may depend on the reaction mechanism, underscoring the need to identify the reaction pathway.

5.5 Conclusions

In conclusion, we used the IPA-to-acetone conversion as a case study to investigate the charge-transfer reaction mechanism under a plasma-anode configuration. The reaction displayed first-order reaction kinetics, and the rate constants were unchanged with the addition of •OH scavengers, suggesting that this reaction is not •OH-mediated. Guided by the lower O-H bond dissociation energy of IPA relative to water, we propose an alternative reaction pathway in which interfacial cations directly react with IPA and initiate oxidation reactions without radical mediation. By comparing the measured rate constants from plasma-anode and plasma-cathode configurations, non-Faradaic IPA losses were eliminated. We find that the cation-induced rate constants increased with higher current and shorter pulse width, resembling the trend in applied voltage. We also illustrate that the Faradaic efficiency of the cation-induced IPA reaction responded differently to plasma parameter changes than that of the •OH-mediated ferrocyanide oxidation reaction.

5.6 References

1. Bruggeman, P. J.; Frontiera, R. R.; Kortshagen, U.; Kushner, M. J.; Linic, S.; Schatz, G. C.; Andaraarachchi, H.; Chaudhuri, S.; Chen, H.-T.; Clay, C. D.; Dias, T. C.; Doyle, S.; Jones, L. O.; Meyer, M.; Mueller, C. M.; Nam, J. H.; Raisanen, A.; Rich, C. C.; Srivastava, T.; Xu, C.; Xu, D.; Zhang, Y., Advances in Plasma-Driven Solution Electrochemistry. *The Journal of Chemical Physics* **2025,** *162* (7),

2. Bruggeman, P. J.; Frontiera, R. R.; Kortshagen, U. R.; Kushner, M. J.; Linic, S.; Schatz, G. C.; Andaraarachchi, H.; Exarhos, S.; Jones, L. O.; Mueller, C. M.; Rich, C. C.; Xu, C.; Yue, Y.; Zhang, Y., Plasma-Driven Solution Electrolysis. *Journal of Applied Physics* **2021,** *129* (20), 200902.

3. Bloomquist, C. K.; Naumov, D.; Yang, A.; Mathison, R.; Herzog, B. D.; Tenn, W. J., III; Modestino, M. A.; Aydil, E. S., Exploring the Balance between Faradaic and Non-Faradaic Processes in Organic Chemical Reactions at Plasma-Liquid Interfaces. *Journal of the American Chemical Society* **2025,** *147* (16), 13937-13947.

4. Bruggeman, P. J.; Kushner, M. J.; Locke, B. R.; Gardeniers, J. G. E.; Graham, W. G.; Graves, D. B.; Hofman-Caris, R. C. H. M.; Maric, D.; Reid, J. P.; Ceriani, E.; Fernandez Rivas, D.; Foster, J. E.; Garrick, S. C.; Gorbanev, Y.; Hamaguchi, S.; Iza, F.; Jablonowski, H.; Klimova, E.; Kolb, J.; Krcma, F.; Lukes, P.; Machala, Z.; Marinov, I.; Mariotti, D.; Mededovic Thagard, S.; Minakata, D.; Neyts, E. C.; Pawlat, J.; Petrovic, Z. L.; Pflieger, R.; Reuter, S.; Schram, D. C.; Schröter, S.; Shiraiwa, M.; Tarabová, B.; Tsai, P. A.; Verlet, J. R. R.; von Woedtke, T.; Wilson, K. R.; Yasui, K.; Zvereva, G., Plasma–Liquid Interactions: A Review and Roadmap. *Plasma Sources Science and Technology* **2016,** *25* (5), 053002.

5. Chen, H.-T.; Lee, D.; Linic, S., Formation of Mixed Bimetallic Nanoparticles of Immiscible Metals through Plasma-Induced Reduction of Precursors in Solutions: A Case Study of Ag–Pt Alloy Nanoparticles. *Chemistry of Materials* **2023,** *35* (16), 6557-6565.

6. Sharma, R. K.; Patel, H.; Mushtaq, U.; Kyriakou, V.; Zafeiropoulos, G.; Peeters, F.; Welzel, S.; van de Sanden, M. C. M.; Tsampas, M. N., Plasma Activated Electrochemical Ammonia Synthesis from Nitrogen and Water. *ACS Energy Letters* **2020**, 313-319.

7. Lee, D.; Chen, H.-T.; Linic, S., Plasma-Induced Selective Propylene Epoxidation Using Water as the Oxygen Source. *JACS Au* **2023,** *3* (4), 997-1003.

8. Chen, S.; Mei, K.; Luo, Y.; Ding, L.-X.; Wang, H., Selective Synthesis of Nitrate from Air Using a Plasma-Driven Gas-Liquid Relay Reaction System. *Journal of Energy Chemistry* **2023,** *85*, 439-446.

9. Xu, X.; Zhao, X.; Tang, J.; Duan, Y.; Tian, Y.-H., Direct Amination of Benzene with Molecular Nitrogen Enabled by Plasma-Liquid Interactions. *Angewandte Chemie International Edition* **2022,** *61* (24), e202203680.

10. Huang, Z.; Xiao, A.; Liu, D.; Lu, X.; Ostrikov, K., Plasma-Water-Based Nitrogen Fixation: Status, Mechanisms, and Opportunities. *Plasma Processes and Polymers* **2022,** *19* (4), 2100198.

11. Thai, V.-P.; Saito, N.; Nakamura, T.; Takahashi, K.; Sasaki, T.; Kikuchi, T., Effect of Voltage Polarity and Supply Frequency on the Properties of Plasma Contacting Liquid Electrodes and Gold Nanoparticle Synthesis. *Plasma Sources Science and Technology* **2022,** *31* (1), 015006.

12. Oldham, T.; Chen, M.; Sharkey, S.; Parker, K. M.; Thimsen, E., Electrochemical Characterization of the Plasma-Water Interface. *Journal of Physics D: Applied Physics* **2020,** *53* (16), 165202.

13. Hawtof, R.; Ghosh, S.; Guarr, E.; Xu, C.; Mohan Sankaran, R.; Renner, J. N., Catalyst-Free, Highly Selective Synthesis of Ammonia from Nitrogen and Water by a Plasma Electrolytic System. *Science Advances* **2019,** *5* (1), eaat5778.

14. Papalexopoulou, K.; Triantaphyllidou, I. E.; Skandalis, S. S.; Rassias, G.; Aggelopoulos, C. A., Optimization of Pulsed DBD Plasmas for the Degradation of Valsartan in Water − Application to Pharmaceutical Pollutants of Other Molecular Classes. *Chemical Engineering Journal* **2025,** *515*, 163732.

15. Richmonds, C.; Witzke, M.; Bartling, B.; Lee, S. W.; Wainright, J.; Liu, C.-C.; Sankaran, R. M., Electron-Transfer Reactions at the Plasma–Liquid Interface. *Journal of the American Chemical Society* **2011,** *133* (44), 17582-17585.

16. Elg, D. T.; Delgado, H. E.; Martin, D. C.; Sankaran, R. M.; Rumbach, P.; Bartels, D. M.; Go, D. B., Recent Advances in Understanding the Role of Solvated Electrons at the Plasma-Liquid Interface of Solution-Based Gas Discharges. *Spectrochimica Acta Part B: Atomic Spectroscopy* **2021,** *186*, 106307.

17. Novelli, F.; Chen, K.; Buchmann, A.; Ockelmann, T.; Hoberg, C.; Head-Gordon, T.; Havenith, M., The Birth and Evolution of Solvated Electrons in the Water. *Proceedings of the National Academy of Sciences* **2023,** *120* (8), e2216480120.

18. Rumbach, P.; Bartels, D. M.; Sankaran, R. M.; Go, D. B., The Solvation of Electrons by an Atmospheric-Pressure Plasma. *Nature Communications* **2015,** *6* (1), 7248.

19. Marcus, R. A., Theory of Electron-Transfer Reaction Rates of Solvated Electrons. *The Journal of Chemical Physics* **1965,** *43* (10), 3477-3489.

20. Wang, J.; Üner, N. B.; Dubowsky, S. E.; Confer, M. P.; Bhargava, R.; Sun, Y.; Zhou, Y.; Sankaran, R. M.; Moore, J. S., Plasma Electrochemistry for Carbon–Carbon Bond Formation Via Pinacol Coupling. *Journal of the American Chemical Society* **2023,** *145* (19), 10470-10474.

21. Delgado, H. E.; Elg, D. T.; Bartels, D. M.; Rumbach, P.; Go, D. B., Chemical Analysis of Secondary Electron Emission from a Water Cathode at the Interface with a Nonthermal Plasma. *Langmuir* **2020,** *36* (5), 1156-1164.

22. Maksimov, A. I.; Khlyustova, A. V., Properties of the Cathode Region of Low-Voltage Atmospheric-Pressure Discharges with Electrolytic Electrodes. *High Energy Chemistry* **2009,** *43* (6), 505-508.

23. Choi, J.; Iza, F.; Lee, J. K.; Ryu, C. M., Electron and Ion Kinetics in a DC Microplasma at Atmospheric Pressure. *IEEE Transactions on Plasma Science* **2007,** *35* (5), 1274-1278.

24. Cserfalvi, T.; Mezei, P., Operating Mechanism of the Electrolyte Cathode Atmospheric Glow Discharge. *Fresenius' Journal of Analytical Chemistry* **1996,** *355* (7), 813-819.

25. Hickling, A.; Linacre, J. K., Glow-Discharge Electrolysis. Part II. The Anodic Oxidation of Ferrous Sulphate. *Journal of the Chemical Society (Resumed)* **1954,** (0), 711-720.

26. Martin, D. C.; Elg, D. T.; Delgado, H. E.; Nguyen, H. M.; Rumbach, P.; Bartels, D. M.; Go, D. B., Optical and Chemical Measurements of Solvated Electrons Produced in Plasma Electrolysis with a Water Cathode. *Langmuir* **2024,** *40* (28), 14224-14232.

27. Kerr, J. A., Bond Dissociation Energies by Kinetic Methods. *Chemical Reviews* **1966,** *66* (5), 465-500.

28. Darwent, B. d.; National Standard Reference Data, S., *Bond Dissociation Energies in Simple Molecules*. U.S. Dept. of Commerce, National Bureau of Standards: Washington, D.C, 1970.

29. Yue, Y.; Exarhos, S.; Nam, J.; Lee, D.; Linic, S.; Bruggeman, P. J., Quantification of Plasma Produced OH and Electron Fluxes at the Liquid Anode and Their Role in Plasma Driven Solution Electrochemistry. *Plasma Sources Science and Technology* **2022,** *31* (12), 125008.

30. Yaws, C. L., *Chemical Properties Handbook : Physical, Thermodynamic, Environmental, Transport, Safety, and Health Related Properties for Organic and Inorganic Chemicals*. New York : McGraw-Hill, [1999] ©1999: 1999.

31. Yujing, M.; Mellouki, A., Temperature Dependence for the Rate Constants of the Reaction of OH Radicals with Selected Alcohols. *Chemical Physics Letters* **2001,** *333* (1), 63-68.

32. Buxton, G. V.; Greenstock, C. L.; Helman, W. P.; Ross, A. B., Critical Review of Rate Constants for Reactions of Hydrated Electrons, Hydrogen Atoms and Hydroxyl Radicals

(·OH/·O^- in Aqueous Solution. *Journal of Physical and Chemical Reference Data* **1988,** *17* (2), 513-886.

33. Jayson, G. G.; Parsons, B. J.; Swallow, A. J., Some Simple, Highly Reactive, Inorganic Chlorine Derivatives in Aqueous Solution. Their Formation Using Pulses of Radiation and Their Role in the Mechanism of the Fricke Dosimeter. *Journal of the Chemical Society, Faraday Transactions 1: Physical Chemistry in Condensed Phases* **1973,** *69* (0), 1597-1607.

34. Rumbach, P.; Clarke, J. P.; Go, D. B., Electrostatic Debye Layer Formed at a Plasma-Liquid Interface. *Physical Review E* **2017,** *95* (5), 053203.

35. Vanraes, P.; Bogaerts, A., The Essential Role of the Plasma Sheath in Plasma–Liquid Interaction and Its Applications—a Perspective. *Journal of Applied Physics* **2021,** *129* (22),

36. Prabhudesai, V. S.; Kelkar, A. H.; Nandi, D.; Krishnakumar, E., Functional Group Dependent Site Specific Fragmentation of Molecules by Low Energy Electrons. *Physical Review Letters* **2005,** *95* (14), 143202.

37. Kaneko, T.; Hatakeyama, R., Plasma–Liquid Interactions for Fabrication of Nanobiomaterials. 1 ed.; CRC Press: 2012.

38. Srivastava, T.; Chaudhuri, S.; Rich, C. C.; Schatz, G. C.; Frontiera, R. R.; Bruggeman, P., Probing Time-Resolved Plasma-Driven Solution Electrochemistry in a Falling Liquid Film Plasma Reactor: Identification of HO_2^- as a Plasma-Derived Reducing Agent. *The Journal of Chemical Physics* **2024,** *160* (9),

39. Xu, D.; Srivastava, T. K.; Bruggeman, P. J., Plasma-Induced Oxidation in Micro-Droplets: Quantifying H_2O_2 and OH Fluxes and Transport Limitations. *Plasma Chemistry and Plasma Processing* **2025,** *45* (3), 661-676.

Chapter 6 Conclusion and Future Directions

6.1 Overall Conclusions

In this dissertation, we develop a tool to characterize plasma-driven solution electrolysis (PDSE), identify a new application, and revisit a key reaction mechanism. We show that PDSE is a complex yet versatile system capable of driving both oxidation and reduction reactions simultaneously. By controlling plasma polarity, the interfacial chemistry can be shifted from reduction reaction-dominated to oxidation reaction-dominated. These reactions, driven by PDSE, proceed via transfer of high-energy species from the plasma to the liquid phase, including electrons, ions, radicals, and photons, that either react directly with the target molecule or first react with solvent molecules to initiate cascading reactions. An overview of these reactions and the mutual interactions between the phases is provided in Chapter 1.

Building on the analogy between PDSE and conventional electrochemical systems, we adopt conventional electrochemical terminology to describe PDSE. In conventional electrochemistry, the electron energy level (Fermi level) in an electrode is set by the applied potential versus a reference. When this electron energy level equals the energy level (solution potential) of a redox couple in the electrolyte, no net conversion of that redox couple occurs at the electrode surface. In PDSE, we discovered that, under certain initial solution potentials, an analogous net zero conversion also arose at the plasma-liquid interface. The solution potential at which this occurred under PDSE depended on plasma parameters, including polarity, pulse width, and applied current, along with the local chemical environment. Notably, whereas in

conventional electrochemistry no net conversion implies no net current across the interface, in PDSE there can still be net charge transfer across the plasma-liquid interface even when the redox couple exhibits zero net conversion.

Given this discrepancy between PDSE and conventional electrochemistry, the net zero conversion of a redox couple can be better interpreted as the outcome of competing interfacial reactions. Reducing species reduce the oxidized form, while the oxidizing species oxidize the reduced form, yielding no net change. We assumed that hydrated electrons (e_{aq}^-) and hydroxyl radicals (•OH) are the dominant and abundant species governing this balance at the interface. Accordingly, we defined the solution potentials at no net conversion as the plasma-generated electrochemical potential and interpreted it as the effective concentration ratios of these two species. These electrochemical potentials provided a framework to compare plasma conditions in the presence of inevitable consumption reactions (e.g., water electrolysis and hydrogen peroxide formation). We further highlighted that the effective concentration ratio could be fine-tuned by the plasma pulse width on the μs timescale and by the current. Increasing the pulse width or decreasing the current increased the reducing effective ratio under negative polarity and the oxidizing ratio under positive polarity. Importantly, these effective ratios should be understood not as reaction rates but as the steady-state concentrations of the redox couple resulting from the dynamic balance of opposing pathways. Under higher-current conditions, the time to reach the no-net-conversion condition decreased, even though the effective concentration ratio was lower. A graphical abstract of Chapter 3 is shown in Figure 6.1.

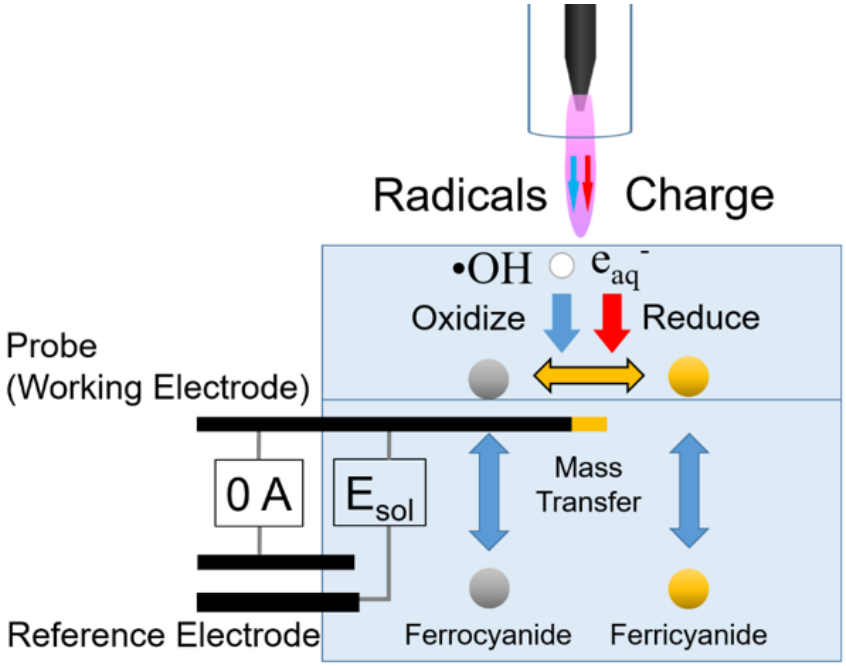


Figure 6.1 Graphical abstract of Chapter 3. We illustrated the electrochemical measurements and the characterization of the high-energy species in PDSE.

The strong reducing capability of PDSE in the plasma-cathode configuration was utilized to synthesize immiscible bimetallic alloy nanoparticles. This synthesis is challenging due to the intrinsic immiscibility of the constituent metals. They must be kinetically trapped into one single structure. Kinetic trapping requires fast reduction rates for both metal precursors in one pot and comparable reduction rates between the two precursors. We achieved the latter by switching the solvent from water to ethylene glycol, which narrowed the gap in precursor reduction rates and enabled the simultaneous generation of metal atoms, facilitating kinetic trapping. Reduction rates were quantified through their relationship to the reduction potentials, measured as onset reduction potentials. By matching the corresponding reduction potentials, the synthesis of alloy nanoparticles was achieved in ethylene glycol. We further validated the requirement for fast reduction by comparing PDSE to a thermal polyol process. Under polyol methods, precursor

reduction rates were relatively low, leading to the formation of only monometallic nanoparticles rather than kinetically trapped bimetallic alloy ones.

Beyond kinetic trapping, plasma parameters and the local chemical environment critically influence the nucleation process. In Chapter 3, we found that longer pulse widths enhance the effective reducing capability; however, in this system, a longer pulse width promoted the simultaneous formation of alloy and monometallic nanoparticles. For certain metals, cluster formation requires exceeding a threshold concentration of metal atoms. Once this threshold is exceeded, rapid cluster formation and aggregation yield monometallic nanoparticles without mixing with the second metal. PDSE uniquely enables μs timescale control to prevent this outcome by turning off the current before the nucleation threshold is reached. We showed that increasing pulse width and precursor concentrations increased the transient metal monomer concentration within a pulse, thereby favoring monometallic nanoparticle formation. Consequently, to obtain exclusively alloy nanoparticles, the pulse width and precursor concentration must be kept sufficiently low to avoid surpassing the threshold concentration. A graphical abstract of Chapter 4 is shown in Figure 6.2.

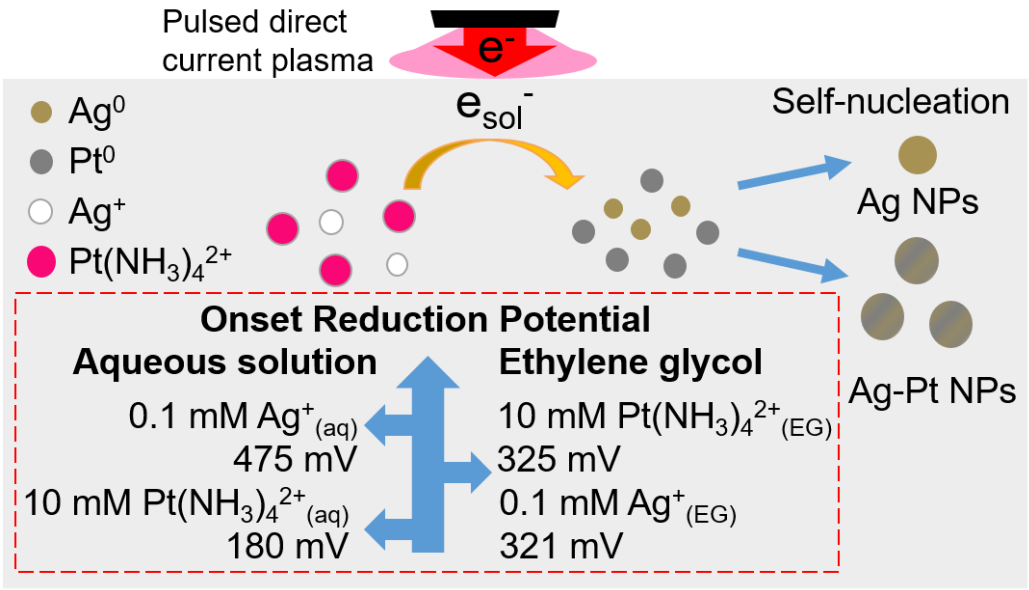


Figure 6.2 Graphical abstract of Chapter 4. We illustrated the three requirements to exclusively form immiscible bimetallic alloy nanoparticles.

Last, we investigated the reaction mechanism of the cations under a plasma-anode configuration. As the cations are established as the primary charge carriers, they drive oxidation reactions in the liquid phase. We considered two possible scenarios: (1) the cations first react with water molecules and drive ionization, dissociation, and other reactions to form reactive intermediates. These reactive intermediates include e_{aq}^- and •OH. Given that oxidation reactions are more dominant, established in Chapter 3, •OH is likely the main reactive species; and (2) the cations directly react with target molecules, with limited contribution from intermediates. Namely, the oxidation reactions might not depend on the presence of •OH. The two possible reaction pathways were tested by adding •OH scavengers, chlorine ion and ferrocyanide. It is also established in Chapter 3 that chlorine ions react with •OH and reduce the effective concentration ratios, confirming their role as a scavenger.

Here, we probed the reaction pathway using the oxidation of isopropyl alcohol (IPA) to acetone. Alcohols are commonly used as •OH scavengers due to its high intrinsic reaction rates

with •OH. Also, IPA exhibits a lower H-O bond dissociation enthalpy change than water (H-OH bond), making it more likely to react with cations than water. We demonstrated that the IPA-to-acetone reaction proceeded under PDSE and their concentrations in the liquid phase can be quantified through the gas-phase concentration measurements. The IPA consumption rate was unchanged by the addition of scavengers, chlorine ions and ferrocyanide, indicating a reaction pathway that involves direct cation-IPA reactions rather than •OH mediation. To further differentiate mechanisms, we compared two oxidation reactions with distinct pathways, IPA-to-acetone and ferrocyanide-to-ferricyanide reactions, and examined their responses to plasma parameter changes. The Faradaic efficiency (chemical conversion per charge input) exhibited different dependencies on the plasma pulse width. This highlights the importance of reaction mechanism understanding for optimizing process conditions and expanding interfacial reaction design under a plasma-anode configuration. A graphical abstract of Chapter 5 is shown in Figure 6.3.

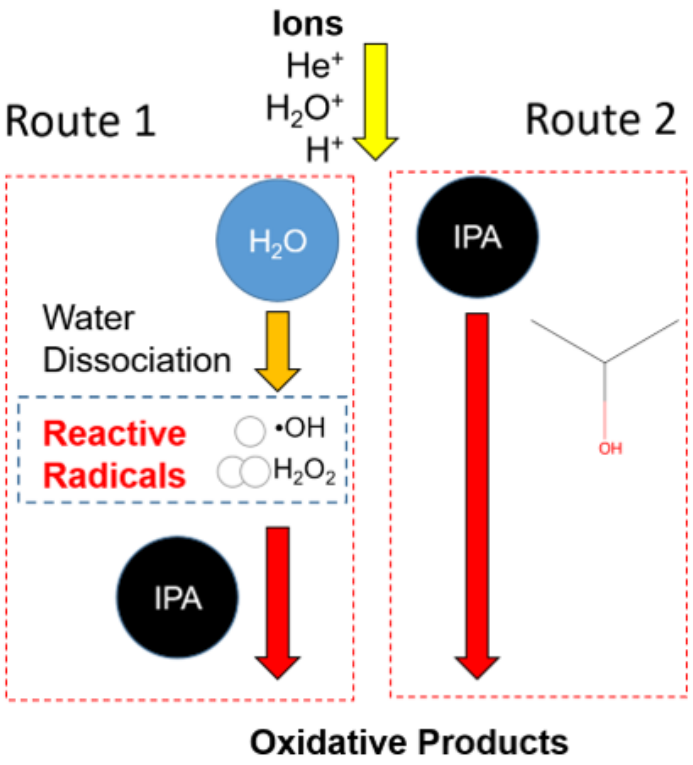


Figure 6.3 Graphical abstract of Chapter 5. We illustrated the two possible reaction pathways and demonstrated that Route 2 is more likely to be the case for the IPA-to-acetone oxidation reaction.

6.2 Critiques

In Chapter 3, we utilized an electrochemical redox couple and a gold probe to characterize the plasma-generated electrochemical potentials. Net zero conversion of the redox couple was achieved with extreme ratios. Namely, in the plasma-cathode configuration, it was likely that all •OH were captured, yet the e_{aq}^- concentration was determined by water electrolysis. Compared with the flux from the plasma phase, this is probably an underestimation to the actual flux. We also noticed a temporal discrepancy between the electron flux and •OH flux.[1] Therefore, the redox couple might be reduced first, then be oxidized back later in the timescale of ~100 μs. In this context, mass-transfer limitations might be an important factor, as ferricyanide at the interface was completely consumed. These effects will be better addressed

through combined simulations and gas-phase measurements. The reaction mechanism discussed in Chapter 5 may influence the outcomes, as it remains unclear whether ferrocyanide can directly react with ions. The complexity of the plasma-anode configuration makes it an oversimplification to account for only two reactive species. Other species might also play a role in the process.[2-4] Still, their concentrations and even their presence remain not well-understood in the absence of an overall picture.

Moreover, the results suggest that PDSE is more closely related to radiolysis than to conventional electrochemistry, since the reactions are driven by high-energy species. The plasma-generated electrochemical potentials depend strongly on the feed gas and can seldom be generalized to other redox couples. For practical utilization of PDSE, reaction rates may likely be a more critical parameter than the no net conversion solution potential.

In Chapter 4, we discussed the synthesis of bimetallic alloy nanoparticles. In this project, we did not account for the longer lifetime of solvated electrons (e_{sol}^-) in ethylene glycol relative to aqueous solution. In ethylene glycol, e_{sol}^- might be consumed less and thus reach higher interfacial concentrations to react with the precursors. Therefore, matched onset reduction potentials might not be the only reason for the formation of alloy nanoparticles. We also did not discuss the possibility of galvanic replacement reactions, which might happen in aqueous solution. Platinum (Pt) and silver (Ag) might both be reduced, but Pt was then replaced by Ag.

The connection from onset reduction potential to reduction potential, and from reduction potential to reduction rate, requires two strong assumptions that should be addressed. The first connection requires the existence of both metal atoms and precursors on the electrode surface, which should also be tested on a Ag electrode. The onset reduction potential might also not be the exact reduction potential. The second connection from reduction potentials to the reduction

rates hypothesized that the reaction with e_{sol}^- follows Marcus theory, which links the rate constants directly to the reduction potentials.[5] Marcus theory requires that precursor reduction proceed via an outer-sphere electron-transfer mechanism.

The characterization of alloy nanoparticles can also be improved. While d-spacing measurement is currently our best available method, X-ray absorption spectroscopy (XAS) will provide more direct and decisive evidence for alloy formation. The change in relative X-ray photoelectron spectroscopy (XPS) intensities in the Pt 4f peaks between Pt nanoparticles and Ag-Pt alloy nanoparticles is also not yet understood. Also, the nucleation mechanism remains unclear. It is difficult to assume a single mechanism for each metal because the literature shows discrepancies. Depending on the conditions, a metal might follow different nucleation mechanisms or a mixture of several. The assignment in Chapter 4 should be discussed further.

Chapter 5 presents an ongoing work that requires additional evidence to confirm the proposed alternative route. Given the large concentration ratio of isopropyl alcohol (IPA) to water, a selective reaction mechanism seems improbable without further proof. The IPA cross-section is likely higher than that of water, but this needs to be confirmed by cross-section measurements. Preferential adsorption of IPA at the plasma-liquid interface may also contribute, analogous to the behavior of certain ions during water splitting on metal electrodes in conventional electrochemistry. This work also requires a deeper understanding of cation-induced reactions, the charge-transfer mechanism, the average cation energy, and the type of cation species. Without these details, a complete picture of charge-transfer-induced reactions under a plasma-anode configuration remains out of reach.

The existence of multiple phases in the system further complicates the reaction mechanism. As a volatile molecule, IPA is present in the plasma phase and can react there. As

the plasma-cathode configuration formed acetone, it should be noted that IPA-to-acetone conversion likely occurs in the plasma phase as well. Even though the plasma-anode configuration produced much higher concentrations than the plasma-cathode case, it remains possible that the IPA-to-acetone conversion happens entirely in the plasma phase, with the plasma-anode configuration promoting the process. This interpretation is still consistent with our two observations: the addition of liquid-phase scavengers did not change the IPA consumption rate, and the response to plasma-parameter changes differed between the two reactions.

We attempted to purge IPA vapor with helium (He) into the plasma phase while excluding IPA from the liquid phase, but IPA rapidly dissolved into the liquid and exhibited similar behavior once IPA and acetone were detectable by GC-MS. Additional experiments and evidence are required to establish this alternative pathway. For example, the distribution of IPA molecules at the PDSE interface should be studied to address these issues. If the IPA is more preferentially adsorbed to the PDSE interface than water, it might help understand the cation-IPA reaction pathway. Another example involves the cross-sections of the IPA-cation reactions. At the plasma-liquid interface, IPA might have a higher cross-section than water, leading to a higher effective collision coefficient and therefore the dominant reaction pathway. This should help understand the tendency of cations to react with IPA instead of water.

6.3 Future Directions

In this dissertation, we focused on the utilization of e_{sol}^-, •OH, and cations. These species are challenging to form and exhibit high reactivity, yet the energy cost of PDSE is high. There needs to be a clear benefit to using these reactive species directly; otherwise, cascading reactions driven by H_2O_2 or other products from PDSE can often be achieved with conventional electrochemistry. The energy requirement is about 100 times higher for PDSE than that of

conventional electrochemical systems, limiting its applications to niche, high-value-added products. Here, we propose several possible directions to improve the utilization and the understanding of PDSE: (1) modifying the liquid environment, (2) comparing between PDSE processes by Faradaic efficiency and/or energy efficiency, (3) advancing the understanding of plasma-phase species and reactions, and (4) varying the feeding gas.

In PDSE, the lifetimes of the high-energy species are often limited due to the reaction with their surroundings. For example, e_{aq}^- are solvated from free electrons and then rapidly react with water to form hydrogen gas. In Chapter 3, we demonstrated that it is an inevitable reaction. Short lifetimes and penetration depths also lead to mass-transfer limitations, as interfacial species are quickly depleted. Utilizing solvents other than water might mitigate these issues and open new opportunities. For example, in Chapter 4, we demonstrated the utilization of ethylene glycol in PDSE, which had similar current profiles to those in aqueous solution. Instead of water splitting, solvated electrons might still react with ethylene glycol in both the gas and liquid phases, yielding different products. If the lifetime of e_{sol}^- is longer in these "inert" solvents, direct utilization of e_{sol}^- might be more prevalent instead of the cascading reactions. Ionic liquids might be promising, though their stability requires careful consideration.

Based on the dissertation, the PDSE system is driven by high-energy species, similar to radiolysis. It might make more sense to quantify PDSE systems by energy efficiency rather than Faradaic efficiency. Unless the process is driven completely by charge transfer, the use of Faradaic efficiency might involve the contributions from other processes that do not involve charge transfer. This leads to a Faradaic efficiency over 100%. The use of energy efficiency can be defined from thermodynamics or by normalization to the energy input. For example, the energy efficiency of producing •OH radicals from water can be expressed as the moles of •OH

produced multiplied by the H-OH bond dissociation enthalpy, divided by the total energy input. It also makes sense to define the metric as the moles of •OH produced per unit energy input to account for multiple processes.

We also note that the characterization of the plasma phase is crucial yet less discussed in the dissertation. For example, the characterization of •OH number densities under varying plasma conditions will strengthen the discussion in Chapter 3. In Figure 6.4, the •OH number densities were measured with different pulse widths by the utilization of laser-induced fluorescence (LIF), which estimated the •OH flux to the liquid phase with a plasma-cathode configuration.[1]. These measurements will also benefit the understanding of the plasma-anode configuration. Optical emission spectroscopy (OES) can also measure the number densities of both polarities under steady-state conditions.[6] Also, in Chapter 5, we discussed that the increase of applied voltages might increase the IPA-to-acetone rate constants. This hypothesis could be supported by measuring the electron temperature and electron number density in the plasma phase.

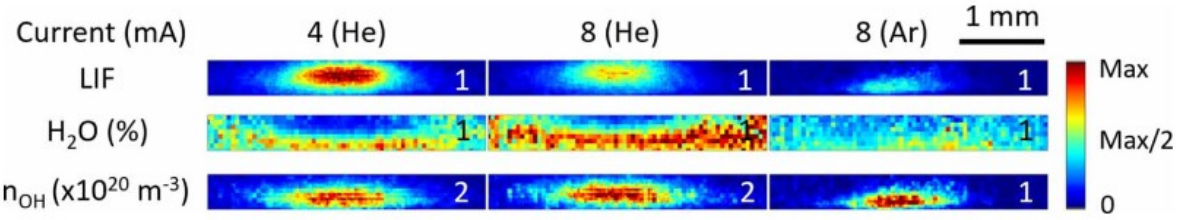


Figure 6.4 LIF intensity, water vapor, and •OH density for He and argon (Ar) DC discharges for varying discharge currents. Voltages were adjusted to achieve the specified currents. Adapted from [1].

Regarding the feeding gas, instead of the inert gas and water combination, the utilization of nitrogen (N_2) is more prevalent with plasmas. N_2 is largely inert due to its strong N≡N triple

bond, which historically limited its practical use. This changed with the Haber-Bosch (H-B) process, a groundbreaking innovation that enabled the large-scale conversion of N_2 into ammonia (NH_3) under high temperatures and pressures.[7] Instead of the high temperatures and pressures, plasma phase reactions have been utilized in ambient conditions to activate inert molecules, such as N_2 and CO_2, which is challenging for conventional electrochemistry. In this case, plasma-liquid interactions have been commonly used to first convert N_2 and O_2 into NO_x, then to urea or NH_3.[8-11] As a more reactive form of nitrogen, NH_3 is a cornerstone for synthesizing a vast array of critical nitrogen-containing compounds.[12-13] Given the high energy consumption of plasma processes, they might be best suited for small-scale and on-site production of key products, which is not achievable with the current H-B infrastructure. Besides, for nitrogen chemistry, the production of other nitrogen-containing compounds directly from N_2 or even from NH_3 might be worth exploring.

6.4 References

1. Yue, Y.; Exarhos, S.; Nam, J.; Lee, D.; Linic, S.; Bruggeman, P. J., Quantification of Plasma Produced OH and Electron Fluxes at the Liquid Anode and Their Role in Plasma Driven Solution Electrochemistry. *Plasma Sources Science and Technology* **2022,** *31* (12), 125008.

2. Clay, C. D.; Mueller, C. M.; Rich, C. C.; Schatz, G. C.; Bruggeman, P. J.; Frontiera, R. R., Evidence for Superoxide-Initiated Oxidation of Aniline in Water by Pulsed, Atmospheric Pressure Plasma. *The Journal of Physical Chemistry Letters* **2024,** *15* (27), 6918-6926.

3. Srivastava, T.; Chaudhuri, S.; Rich, C. C.; Schatz, G. C.; Frontiera, R. R.; Bruggeman, P., Probing Time-Resolved Plasma-Driven Solution Electrochemistry in a Falling Liquid Film

Plasma Reactor: Identification of HO_2^- as a Plasma-Derived Reducing Agent. *The Journal of Chemical Physics* **2024,** *160* (9),

4. Bruggeman, P. J.; Frontiera, R. R.; Kortshagen, U.; Kushner, M. J.; Linic, S.; Schatz, G. C.; Andaraarachchi, H.; Chaudhuri, S.; Chen, H.-T.; Clay, C. D.; Dias, T. C.; Doyle, S.; Jones, L. O.; Meyer, M.; Mueller, C. M.; Nam, J. H.; Raisanen, A.; Rich, C. C.; Srivastava, T.; Xu, C.; Xu, D.; Zhang, Y., Advances in Plasma-Driven Solution Electrochemistry. *The Journal of Chemical Physics* **2025,** *162* (7),

5. Marcus, R. A., On the Theory of Oxidation-Reduction Reactions Involving Electron Transfer. I. *The Journal of Chemical Physics* **1956,** *24* (5), 966-978.

6. Thai, V.-P.; Saito, N.; Nakamura, T.; Takahashi, K.; Sasaki, T.; Kikuchi, T., Effect of Voltage Polarity and Supply Frequency on the Properties of Plasma Contacting Liquid Electrodes and Gold Nanoparticle Synthesis. *Plasma Sources Science and Technology* **2022,** *31* (1), 015006.

7. Appl, M., Ammonia, 1. Introduction. In *Ullmann's Encyclopedia of Industrial Chemistry*, 2011.

8. Huang, Z.; Xiao, A.; Liu, D.; Lu, X.; Ostrikov, K., Plasma-Water-Based Nitrogen Fixation: Status, Mechanisms, and Opportunities. *Plasma Processes and Polymers* **2022,** *19* (4), 2100198.

9. Jayanarasimhan, A.; Pierrard, R.; Peyres, S. M.; Yatom, S.; Curreli, D.; Sankaran, R. M., Insights into Sustainable Nitrogen Fixation by Gas-Phase Spectroscopic Measurements and Global Modeling of Reaction Intermediates in Humid Nitrogen Plasma. *ACS Sustainable Chemistry & Engineering* **2025,** *13* (1), 140-150.

10. Tang, Y.; Dai, J.; Zhang, P.; Niu, G.; Duan, Y.; Tian, Y.-H., Selective Nitrate Synthesis by Plasma/Liquid Water Reaction: An Enhanced Oxidative Strength Mechanism in Nitrogen Discharge. *ACS Sustainable Chemistry & Engineering* **2024,** *12* (30), 11319-11326.

11. Song, X.; Ma, X.; Chen, T.; Xu, L.; Feng, J.; Wu, L.; Jia, S.; Zhang, L.; Tan, X.; Wang, R.; Chen, C.; Ma, J.; Zhu, Q.; Kang, X.; Sun, X.; Han, B., Urea Synthesis Via Coelectrolysis of CO_2 and Nitrate over Heterostructured Cu–Bi Catalysts. *Journal of the American Chemical Society* **2024,** *146* (37), 25813-25823.

12. Kim, S.; Loose, F.; Chirik, P. J., Beyond Ammonia: Nitrogen–Element Bond Forming Reactions with Coordinated Dinitrogen. *Chemical Reviews* **2020,** *120* (12), 5637-5681.

13. Rouwenhorst, K. H. R.; Engelmann, Y.; van 't Veer, K.; Postma, R. S.; Bogaerts, A.; Lefferts, L., Plasma-Driven Catalysis: Green Ammonia Synthesis with Intermittent Electricity. *Green Chemistry* **2020,** *22* (19), 6258-6287.